The
University
Of
Sheffield.

Department of
Automatic Control and
Systems Engineering

A STATISTICAL STUDY OF IONOPAUSE PERTURBATION AND ASSOCIATED BOUNDARY WAVE FORMATION AT VENUS

Ghai Siung **CHONG**

Supervisor: Dr Simon POPE,
Professor Michael BALIKHIN

Submitted in part fulfilment of the requirements for the degree of
Doctor of Philosophy in Engineering at the University of Sheffield

September 2018

Abstract

Previous missions to Venus have revealed that encounters with plasma irregularities of atmospheric origin outside the atmosphere are not uncommon. A number of mechanisms have been proposed to discuss their origins. One such mechanism involves an ionopause with a wavelike appearance. Extensive research on this characteristic of the ionopause is crucial in understanding the atmospheric evolution of Venus.

This thesis implemented an approach to identify potential boundary crossings resulting from ionospheric boundary waves. Coupled with Minimum Variance analysis, this approach was able to demonstrate whether or not the boundary crossings are 'smooth' or 'rippled'. By utilising the magnetic field and plasma data from Venus Express (VEX) over its entire mission from 2006 to 2014, this work presents the first observational statistical analysis of the ionospheric boundary waves at Venus.

The average estimated ionospheric boundary thickness is 57 ± 4 km. This value which is estimated during solar minimum is roughly 1.5 times more than those estimated during solar maximum period. Further analysis shows that the boundary is thicker for weaker pressure and at higher altitudes. On the other hand, the boundary is thinner for stronger pressure at lower altitudes.

In the northern polar region of Venus, the normal directions of the rippled ionospheric boundary crossings lie mainly in the terminator plane with the largest component predominantly along the dawn-dusk (Y_{VSO}) direction. The average estimated wavelength of the boundary wave is 212 ± 12 km and the average estimated velocity difference across the ionopause is 104 ± 6 km s^{-1}. The consistency shown between these results and the results from previous simulation studies of the Kelvin-Helmholtz Instability (KHI), suggests that the rippled boundary is a result of KHI. Furthermore, the magnetic field orientation in the barrier region is found to be quasi-perpendicular to the terminator plane, which is a favourable condition for the excitation of KHI along the dawn-dusk direction.

Analysis reveals a correlation between the normal directions and the locations of the boundary wave with respect to Venus. This indicates the draping of magnetic field lines appear to play a role in enhancing the plasma flow along the dawn-dusk direction, which could subsequently set up a velocity shear that favours the excitation of ionospheric boundary wave by the KHI along the dawn-dusk direction. Two other previously proposed boundary wave excitation mechanisms are also explored.

In addition, flux ropes are also identified using a similar approach. The average estimated flux ropes diameter is 90 ± 6 km and they have axial orientations which lie mainly along the Venus-Sun (X_{VSO}) direction. The consistency in the sizes, locations and orientations shown between the identified flux ropes and boundary wave events suggest that these flux ropes are created as a result of the boundary waves reaching a turbulent stage.

In summary, this statistical study reveals that the ionopause of Venus does not always appear to be smooth, but often exhibits a wavelike appearance. Further analysis suggests that this wavelike appearance of the Venus ionopause is likely to be excited by the KHI, which arises as a result of the velocity shear across the ionopause driven by the draping pattern from the magnetic field. This study also shows that flux ropes can form and populate inside the ionosphere as a result of turbulent boundary wave. On the other hand, atmospheric bubbles can also form in similar manners and exist outside the ionosphere. Continuous scattering and the subsequent convection of atmospheric bubbles downstream and away from Venus over a prolonged period of time plays an important role in atmospheric loss from Venus.

Acknowledgements

First and foremost, massive love and the biggest hugs to my supervisor, the one and only Dr. Simon Pope who is, and will always be there (be it for meetings or at restaurants) and provides unconditional guidance with his brutal honesty. Nothing can describe how thankful I am to have known you and how fortunate I am to be given this opportunity to work with you. I will never forget the promise you made 5 years ago to cook me foods. Miracles might happen one day who knows ;)

Special appreciation also goes to Professor Misha Balikhin, a wise, strict, protective fatherly figure who sees me as a kid and shows incredible care towards me. He always make sure that I have a full tummy to attend conferences.

Finally, massive shoutouts to my colleagues in the Space System Laboratory: Rich, Simon, Stef and Carol who make working enjoyable and not forgetting the uncountable amount of heavenly chocolates (and laughter) we share in the office:

Simon, an ageless man who also happens to be a human encyclopedia. Without him, I would have spent hours and hours looking for answers from the internet. Richard, a slightly shy genius who appreciates foods as much as I do. He is like a brother to me. I will truly miss the countless medium rares we had (not to forget the beers and Sangrias too). Best pal to attend conferences with! The cakes and chocolates Carol brought in all these years! Legend once says there is a friend of Carol who does not know the Pina Colada Carol once had in Cuba.... I guess only time will tell! Not to forget my compatriot Stef who I shared my journey with all these years! Last special appreciation goes to Lobby and Magic who ensure that I have a satisfied stomach at conferences!

The years I spent on my PhD might have be tough, but I would not swap it with anything else. My colleagues are like my family. I will miss them dearly when I leave. I am sure they will miss my singing in the office too!

“Yang bulat tidak datang menggolek, yang pipih tidak datang melayang”

...

You reap what you sow

Nomenclature

General Plasma Properties

ρ	plasma density
$\mathbf{B}$	Magnetic field
$\mathbf{E}$	Electric field
$\mathbf{v}$	Bulk plasma velocity
$\mathbf{v_e}$	Escape velocity
n	number density
T	plasma temperature

Instruments

ASPERA	Analyser of Space Plasmas and Energetic Atoms
ELS	Electron Spectrometer
IMA	Ion Mass Analyser
MAG	Magnetometer
NPD	Neutral Particle Detector
NPI	Neutral Particle Imager
PVO	Pioneer Venus Orbiter
VEX	Venus Express

Acronym

ESA	European Space Agency
EUV	Extreme Ultraviolet

FLR	Finite Larmor Radius
ICME	Interplanetary Coronal Mass Ejection
KHI	Kelvin-Helmholtz Instability
MHD	Magnetohydrodynamic
$\mathbf{M_p}$	Planetary body mass
NASA	National Aeronautics and Space Administration
RTI	Rayleigh-Taylor Instability
SLAMS	Short Large Amplitude Magnetic Structures
UTC	Universal Time Coordinated
UV	Ultraviolet

Physics Constants

μ_0	free space magnetic permeability	$4\pi \times 10^{-7}\ \mathrm{H\ m^{-1}}$
G	Universal gravitational constant	$6.67 \times 10^{-11}\ \mathrm{m^3\ kg^{-1}\ s^{-2}}$
$\mathrm{k_B}$	Boltzmann's constant	$1.38 \times 10^{-23}\mathrm{J\ K^{-1}}$
$\mathrm{R_E}$	Radius of Earth	6371 km
$\mathrm{R_V}$	Radius of Venus	6052 km

Contents

List of Tables

List of Figures

Chapter 1

Introduction

Venus, which is one of the brightest objects in the sky after the Sun and the moon, is often the first visible object when the night falls, or one of the last visible objects when dawn breaks. Hence, it is sometimes regarded as the "evening star" or the "morning star". As the closest neighbour of our Earth, Venus had been the prime targeted planet during the early era of space exploration. In fact, it is the first planet to be visited by a spacecraft (*Mariner 2* [*Sonett*, 1963]) and Venus has been visited by more spacecraft than any other planets apart from the Earth.

Based on the similarity in their interior compositions, sizes and the similar distance to the Sun [*Williams*, 2005], Venus is often regarded as the twin sister of Earth. However, past missions to Venus have revealed that the surface conditions of these two planets are a world apart. Venus's surface temperature is around 464 °C and its surface pressure is about 92 times more than Earth's [*Williams*, 2005]. A pressure so high that the longest any landers could operate was only around 110 minutes (*Venera 12* [*Johnson*, 1979]). So it is understandable why Venus is sometimes also regarded as the evil twin sister of Earth.

Compared to Earth, Venus took a contrasting path to evolve. While majority of the Earth's surface is covered with liquid water, Venus surface is virtually dry. However, it is noteworthy to mention that the conditions on Venus have not been this hostile and harsh throughout its history. A recent study [*Way et al.*, 2016] has shown that

Venus could have had a shallow liquid water ocean and a moderate surface temperature billions of years ago; a habitable environment that could allow life to flourish, or at least a chance for life to form and evolve. As the liquid water receives heat energy from the Sun, it evaporates and condenses in a continuous cycle that is similar to Earth's. However, as Venus evolved, the surface temperature increased and kept the water vapour from condensing. The liquid oceans eventually dried up and mainly became water vapour in the atmosphere.

These hot water vapours are very reactive. They can react with other gases such as sulphur dioxide to form sulphuric acid. They are then photo-dissociated and exist as charged particles floating on top of the atmosphere, a region collectively known as the ionosphere. Without a strong intrinsic magnetic field similar to those on Earth, the solar wind, which is a hot stream of ionised particles constantly blasted from the Sun [*Baumjohann et al.*, 1996], can interact directly with these ionospheric particles, separated by a boundary called the ionopause. The solar wind can then strip off and subsequently convect these ionospheric particles away from Venus as it impacts on the atmosphere [*Brace et al.*, 1982].

For example, waves can be observed when gust of wind flows past a body of water. And faster flowing wind results in bigger waves. The waves will eventually break and droplets of water will form. They can then be blown away when the waves become turbulent and the gravity could no longer hold down the water droplets. Prolonged period of such persistent process will eventually lead to total loss of water. This scenario is analogous to the atmosphere of Venus but on a much larger scale. Boundary waves can arise when the solar wind interacts directly with the atmosphere of Venus. These waves can grow, become turbulent and droplets of atmospheric contents can be formed. These droplets are called the atmospheric bubbles and they can subsequently be convected into space with the solar wind [*Wolff et al.*, 1980].

This is one of the many but perhaps the most effective atmospheric plasma removal mechanism for Venus that plays an important role in removing the water contents from the planet [*Lammer et al.*, 2006]. The aim of this thesis is to study the dynamic stability of the ionosphere in response to the solar wind and its role in the atmospheric evolution at Venus.

1.1 Outline of the Thesis

This thesis is organised as follows. Chapter 2 reviews the solar wind interaction with Earth and compares it to Venus, illustrating the dynamic response of the Venusian ionopause. This is followed by a review on the role of boundary waves in the atmospheric evolution at Venus. Chapter 3 describes the instrumentation onboard of Venus Express (VEX) and the methodologies that will be implemented in the thesis. A detailed analysis of the ionospheric boundary waves and an embedded flux rope observed on 26 Jun 2006 will be presented in Chapter 4. Chapter 5 presents a statistical survey on the ionospheric boundary stability conducted over the whole VEX mission, complemented with their global characteristics. The second half of this chapter will present a detailed analysis of the boundary wave induced-magnetic flux ropes. The potential wave excitation and generation mechanisms will be assessed and discussed in Chapter 6. Finally, this thesis will be concluded in Chapter 7 and an outlook for future investigations will also be presented.

1.2 Novel contributions

The main novel contributions of this thesis are summarised as follow.

1. This thesis presents an analysis of an ionospheric boundary wave event and an embedded flux rope observed on 26 Jun 2006 by utilising the VEX data. The results provide the first detailed evidence of the ionopause boundary existing in a wavelike state and they are presented in Chapter 4. They have also been published in *Chong et al.* [2017] as detailed in the following section.
2. Above contribution leads to the first statistical observational study on the boundary wave phenomena at Venus by implementing a similar approach over the entire

VEX mission duration. In particular, to measure the global distribution and the characteristics (e.g. locations and sizes) of the Venusian ionospheric boundary wave. Analysis reveals that the ionopause of Venus does not always appear to be smooth, but often exhibits a wavelike appearance. The results can provide an explanation to the previously observed atmospheric bubbles [*Brace et al.*, 1982] outside the ionosphere that may play a vital role in the atmospheric evolution at Venus. The results are presented in Chapter 5.5 and they have been accepted for publication in *Chong et al.* [2018] (detailed in the following section).

3. This thesis presents the first statistical study of the ionopause current sheet dynamics over the solar minimum period, in particular the relationship between the boundary altitude, thickness and the external pressure. The results are consistent to and complement the study by *Elphic et al.* [1981], which prior to this thesis, was the only statistical work on the Venusian ionopause dynamics but covers the solar maximum period by utilising the data from the Pioneer Venus Orbiter (PVO). In particular, the finite estimated boundary thickness will be utilised in later chapters to validate the estimated wavelength of previous simulation studies on Kelvin-Helmholtz waves. The results are presented in Chapter 5.4.

4. By implementing a new approach to identify magnetic flux ropes in the ionosphere, this thesis presents a statistical study that for the first time to evidence the formation of flux ropes is as a result of turbulent boundary wave. This study provides an explanation of a strong preference in the magnetic flux rope orientations with respect to their observed altitudes, which have been reported by a number of previous works [*Chen et al.*, 2017; *Russell*, 1990; *Elphic and Russell*, 1983]. The results are presented in Chapter 5.6. They will be drafted and submitted to the Journal of Geophysical Research: Space Physics.

5. This thesis explored and assessed the boundary wave generation mechanisms that were previously proposed by *Brace et al.* [1980] and *Luhmann* [1990]. Results reveals that neither mechanism could explain the characteristics of the observed ionospheric boundary waves. On the other hand, the results in this thesis suggest that the magnetic field draping pattern plays an important role in exciting and

generating the ionospheric boundary wave to propagate mainly along the Y_{VSO} axis. The results are presented in Chapter 6 and the discussions on the role of magnetic field draping have been accepted for publication in *Chong et al.* [2018] (detailed in the following section).

1.3 Relevant Publications

As a result from the work conducted during the production of this thesis, **1** journal paper has been published and **1** manuscript has been accepted for publication to the Journal of Geophysical Research (JGR) - Space Physics, 1 invited seminar has been presented and a number of conferences presentations have been given at international conferences.

Published journal paper

1. **Chong, G. S.**, S. A. Pope, T. L. Zhang, G. A. Collinson, S. N. Walker, and B. M. Balikhin (2017). A study of ionopause perturbation and associated boundary wave formation at Venus. Journal of Geophysical Research: Space Physics, 122(4), 4284-4298. doi:10.1002/2016JA023769.

Journal paper - accepted for publication

1. **Chong, G. S.**, S. A. Pope, S. N. Walker, R. A. Frahm, T. L, Zhang, and Y. Futaana (2018), A statistical study of ionospheric boundary wave formation at Venus. Journal of Geophysical Research - Space Physics. doi:10.1029/2018JA025644.

Invited seminar

1. **Chong, G. S.**, S. A. Pope, S. N. Walker, R. A. Frahm, T. L, Zhang, and Y. Futaana (2018), A statistical study of ionopause perturbation and associated boundary wave formation at Venus, The Solar Physics and Space Plasma Research Centre (SP^{2}RC) Seminar, Sheffield, May 2018.

Conference proceedings

1. **Chong, G. S.**, S. A. Pope and S. N. Walker (2018), Statistical analysis of ionospheric boundary wave phenomena on Venus, In 42nd COSPAR Scientific Assembly (Vol. 42). **Poster Presentation**

2. **Chong, G. S.**, S. A. Pope, S. N. Walker and G. A. Collinson (2018), Statistical analysis of ionospheric boundary wave phenomena on Venus, EGU meeting, Vienna, Austria, April 2018. **Poster Presentation**

3. **Chong, G. S.**, S. A. Pope, S. N. Walker, T. Zhang, and B. M. Balikhin (2017), A statistical study of ionopause perturbation and associated boundary wave formation at Venus, AGU Fall meeting, New Orleans, USA, December 2017. **Poster Presentation**

4. **Chong, G. S.**, S. A. Pope, T. Zhang, G. A. Collinson, S. N. Walker, and B. M. Balikhin (2016), A study of ionopause perturbation and associated boundary wave formation at Venus., AGU Fall meeting, San Francisco, USA, December 2016. **Oral Presentation**

5. **Chong, G. S.**, Balikhin, M. A., and Pope, S. A.(2016). A study of ionopause perturbation and associated wave formation at Venus. In 41st COSPAR Scientific Assembly, abstracts from the meeting that was to be held 30 July-7 August at the Istanbul Congress Center (ICC), Turkey, but was cancelled. See http://cospar2016.tubitak.gov.tr/en/, Abstract C3. 2-28-16. (Vol. 41). **Oral Presentation**

6. Pope, S. A., **Chong, G. S.**, Collinson, G., Zhang, T., and Balikhin, M. A. (2016). The magnetosphere of Venus under unusual Solar Wind condition., AGU Fall meeting, San Francisco, USA, December 2016. **Poster Presentation**

Chapter 2

Review of the solar wind interaction with planetary bodies

2.1 Venus: present day

Mercury, Venus, Earth and Mars, which are the first four planets away from the Sun, are called the terrestrial planets. They are characterised based on their main composition of rocks or metals. The main characteristics of Venus and other terrestrial planets ([*Williams*, 2005], and references therein) are summarised in Table 2.1.

Venus has a mass of $\sim 4.87 \times 10^{24}$ kg and a diameter of 12103 km. It has a volume of $\sim 92.843 \times 10^{10}$ km^3 and a surface gravitational acceleration of ~ 8.9 m/s^2. The rotation period of Venus is 5832.6 hours (roughly 243 Earth days) compared to only ~24 hours on Earth. This implies that the days and nights are very long at Venus, sunsets and sunrises only happen every 243 Earth days to be exact. Moreover, with an orbital eccentricity of ~ 0, Venusian orbit is the closest to circular. In addition, Venus is the only planet other than Uranus that has a retrograde rotation, which means that the rotation directions around their axes are in the different directions (anti-clockwise) to their orbital directions around the Sun (anti-clockwise) [*Correia and Laskar*, 2010]. One theory for Uranus retrograde motion is its collision with a protoplanet during the formation of the solar system. Due to its dense atmosphere and close proximity to the

Sun, Venusian retrograde rotation can be attributed to the tidal dissipation between the gravitational and atmospheric tides [*Correia and Laskar*, 2010].

Venus has long been considered a twin sister of the Earth simply based on their close resemblance in the bulk parameters, only if their distinctive atmospheric characteristics are not considered. For instance, the mean surface temperature on Venus is 464 °C compared to only 15 °C on Earth. In addition, the surface pressure on Venus is about 92 bars, that is 92 times more than Earth, which is equivalent to the pressure around 920 metres deep in the ocean. This surface pressure is so high that all the Russian *Venera* landers to Venus in the 70s and 80s crashed. The longest time any lander has ever spent on the surface to transmit data back to Earth was *Venera* 12, a total of 110 minutes to be exact before it was crushed by the extreme environment [*Johnson*, 1979]. Compared to Earth, present day Venus has an extremely harsh environment for any form of life, so it is understandable why Venus is sometimes regarded as the evil twin sister of Earth.

2.1.1 Venus was once hospitable

Perhaps the most distinctive difference between present day Venus and Earth is the presence of water, arguably the most essential necessity for life. While the extreme temperature at Venus would have boiled all the water from its surface making it a very dry planet, in comparison, 71% of Earth's surface is covered with water. However, Venus has not always been this inhospitable. The high deuterium-to-hydrogen ratio on present day Venus (which is $\geq$ 100 times more than Earth's) indicates that Venus may have had an ocean of water early in its history [*Donahue and Hartle*, 1992; *McElroy et al.*, 1982]. In addition, a recent 3-D climate simulation [*Way et al.*, 2016] has shown that Venus could have had a shallow liquid water ocean and a moderate surface temperature billions of years ago; a habitable environment that could allow life to form. The similarity in the bulk characteristics between Venus and Earth indicates that the initial stages of the formations of both planets should be similar, but if both planets were to evolve in a similar way, why are they so distinctively different now? Where did the water that

Table 2.1: Comparisons between the terrestrial planets. E.g. Mercury, Venus, Earth and Mars. After *Williams* [2005, and references therein].

Parameters	**Mercury**	**Venus**	**Earth**	**Mars**
Bulk and orbital Parameters				
Mass (10^{24} kg)	0.33	4.87	5.97	0.642
Diameter (km)	4879	12,104	12,756	6792
Density (kg/m^3)	5427	5243	5514	3933
Volume (10^{10} km^3)	6.083	92.843	108.321	16.318
Gravity (m/s^2)	3.7	8.9	9.8	3.7
Escape Velocity (km/s)	4.3	10.4	11.2	5
Rotation Period (hours)	1407.6	-5832.5	23.9	24.6
Length of Day (hours)	4222.6	2802	24	24.7
Distance from Sun (10^6km)	57.9	108.2	149.6	227.9
Perihelion (10^6 km)	46	107.5	147.1	206.6
Aphelion (10^6 km)	69.8	108.9	152.1	249.2
Orbital Period (days)	88	224.7	365.2	687
Orbital Velocity (km/s)	47.4	35	29.8	24.1
Orbital Inclination (degrees)	7	3.4	0	1.9
Orbital Eccentricity	0.205	0.007	0.017	0.094
Obliquity to Orbit (degrees)	0.034	177.4	23.4	25.2
Number of Moons	0	0	1	2
Global Magnetic Field?	Yes	No	Yes	No
Atmospheric Parameters				
Mean Temperature (C)	167	464	15	-65
Surface Pressure (bars)	$<\sim 5 \times 10^{-15}$	92	1	0.01
Surface density (kg/m^3)	Vacuum	65.0	1.217	0.02
Total mass of atmosphere (kg)	$<\sim$10000	4.8×10^{20}	5.1×10^{18}	2.5×10^{16}
Atmospheric composition				
(by volume, dry air) %	Na 12.0	CO_2 96.5	N_2 78.1	CO_2 95.3
	Mg 60.0	N_2 3.5	O_2 21.0	N_2 2.7
	O_2 24.0		CO_2 0.03	Ar 1.6
	H_2 3.0			O_2 0.13
	K 0.8			CO 0.08

once existed on Venus go?

2.1.2 Where did the water go?

The atmosphere that we enjoy much today takes a lengthy process to evolve since its formation [*Marshall*, 2009; *Chaisson and McMillan*, 1995]. Earth's atmosphere was formed mainly from the volcanic gases which were outgassed as a result of volcanic activity during the early days of its formation. These volcanic gases are mainly composed of water vapour, carbon dioxide, sulphur dioxide, methane, and nitrogen-rich compounds [*Chaisson and McMillan*, 1995]. As the Earth's surface cooled, these water vapours condensed and subsequently covered the surface with a layer of liquid ocean. The carbon dioxide and sulphur dioxide then dissolved into the ocean or deposited in the surface rocks. As life formed in the oceans more than 3.5 billion years ago [*Marshall*, 2009], oxygen was slowly produced and life started to flourish on Earth. As Sun rays penetrated through the cloud and reached the surface, majority of the energy was reflected back into the space and only minority of the energy was absorbed by the atmospheric greenhouse gases, for example the carbon dioxide and water vapour. It is this continuous process that keeps the Earth hospitable, a comfortably warm planet where we call home [*Chaisson and McMillan*, 1995].

Venus is located 30% closer to the Sun compared to Earth, implying that Venus was much hotter during the early stages of its formation as it received more energy from the Sun. An ocean was still expected to form, but it might not have been as abundant as on Earth [*Raymond et al.*, 2006]. This is because the high temperature at Venus would keep the kinetic energy of the water vapour high. The exact temperature was unknown but it was believed that the temperature was high enough to keep the vaporisation rate constantly greater than the condensation rate, which would cause more water to exist in the forms of gases rather than liquid [*Kasting and Pollack*, 1983]. The lack of liquid water subsequently implies that majority of the carbon dioxide would also exist in a gaseous form. These two biggest greenhouse effect contributors eventually lead Venus into a looped process which is known as the runaway greenhouse effect

[*Hamano et al.*, 2013; *Luger and Barnes*, 2015; *Kasting*, 1988]. The water vapours would combine with sulphur dioxide to form clouds of sulphuric acid that ranges from around 45 km to around 70 km [*Taylor*, 2006]. Even though this thick cloud layer would only allow around 20% of sunlight to penetrate and reach the surface, majority of this energy would be trapped and absorbed by the atmosphere. This subsequently raises the surface temperature further and eventually boiled the whole ocean [*Chaisson and McMillan*, 1995]. These water vapours are then subjected to photodissociation by the solar ultraviolet (UV) light when they reach high enough altitude in the atmosphere and are subsequently lost into space [*Kasting*, 1988; *Ingersoll*, 1969; *Pollack et al.*, 1987; *Kasting and Pollack*, 1983]. This same process could also explain both the high temperature and pressure at Venus. Even though the early ocean could have been habitable, the prolonged process of such runaway greenhouse effect left a very harsh and inhospitable place for life to evolve, let alone for life to form.

However, if Earth's upper atmosphere is also subjected to photodissociation and photoionisation processes, how did Venus lose the majority of its atmospheric water contents (currently only around 20 ppm (parts per million) water molecules exist in the atmosphere[*Williams*, 2005]), while 71% of Earth's surface is covered with water?

2.2 Solar wind interaction with Earth (magnetised body)

The Sun is constantly blasting a huge amount of plasma, resulting from the expansion of hot solar coronal gases at a supersonic speed [*Baumjohann et al.*, 1996]. This population of plasma, collectively known as the solar wind, is a stream of hot gas composed of ionised particles, i.e. the positively charged protons and negatively charged electrons as well as about 5% of Helium ions. The solar wind typically has an electron density of ≈ 5 cm^{-3} and temperature of $\approx 10^5$ K near Earth, though these values vary with time [*Baumjohann et al.*, 1996]. It carries an interplanetary magnetic field (IMF) with coronal origins, into the solar system [*Owens and Forsyth*, 2013]. These charged particles have a big impact on everything in their path, including all the planetary bodies.

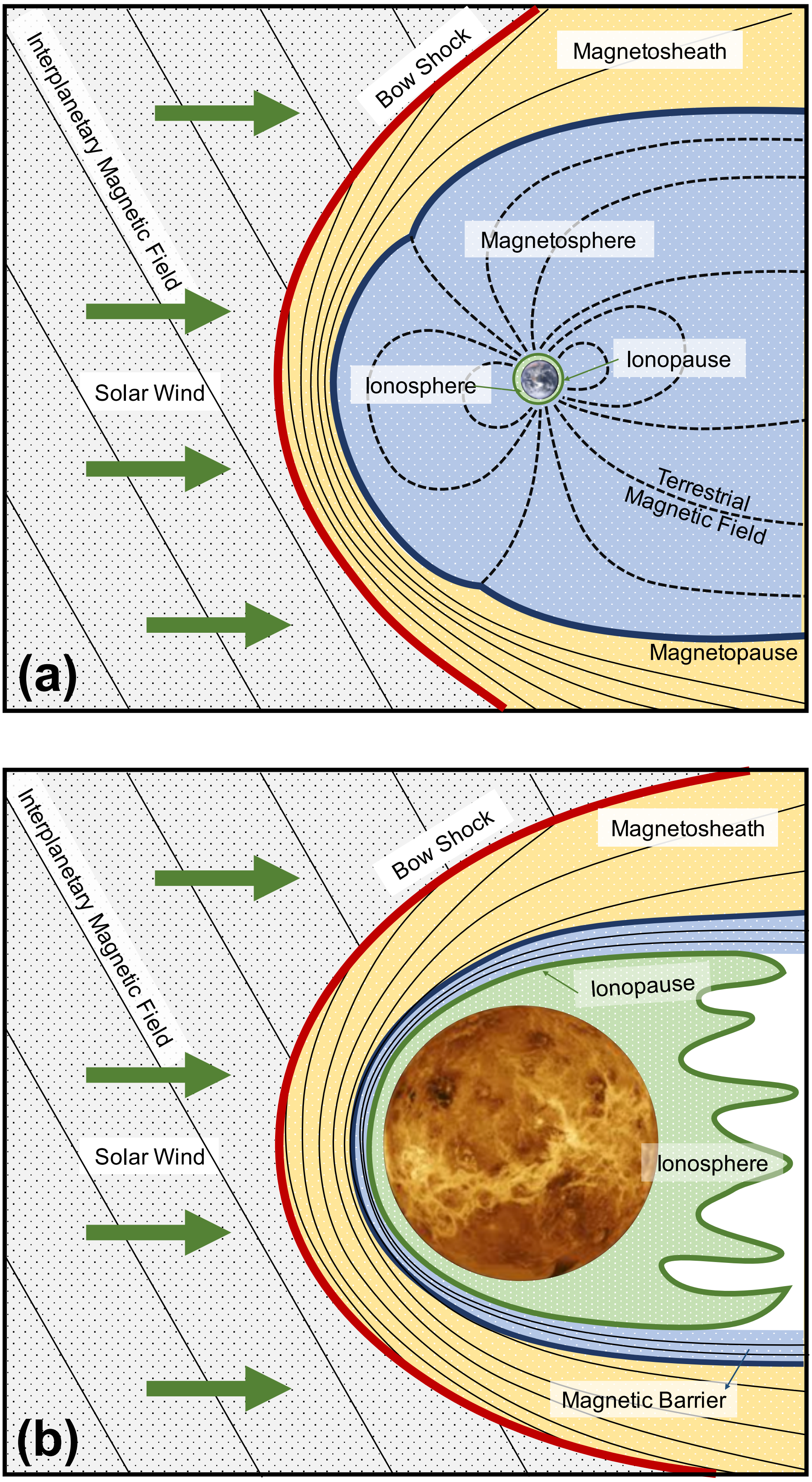

Note: Figures are not drawn to scale

Figure 2.1: Topography environments of the solar wind interaction with (a) Earth and (b) Venus. Illustrations are not drawn to scale. Source of the picture of Earth: © Copyright: EUMETSAT 2002. ID: 197557. Source of the picture of Venus: Image credit: Magellan Project/NASA/JPL.

Earth has a strong dipolar magnetic field that projects into space and acts as the prime obstacle to prevent the solar wind from directly interacting with the atmosphere. The magnetism is mostly generated by the molten iron alloy spinning in the Earth's outer core, a process generally known as the dynamo theory [*Stevenson*, 2003]. As the solar wind approaches the terrestrial magnetic field, its super-magnetosonic speed abruptly changes and a bow-shaped shock is formed. Hence, this boundary that separates the shocked from the unshocked solar wind is called the bow shock. Across the bow shock, a substantial fraction of the solar wind's dynamic energy is converted into thermal energy by dispersive and dissipative processes [*Kennel et al.*, 1984], creating a region of thermalised plasma, which is also known as the magnetosheath.

The shocked solar wind cannot simply penetrate the terrestrial magnetic field. It is mostly deflected around the obstacle and the IMF lines start to drape around Earth. This subsequently forces the terrestrial magnetic field lines into a cavity known as the magnetosphere. And the boundary that separates the magnetosphere from the shocked solar wind, is called the magnetopause. The nightside region where the magnetic field lines are stretched far in the anti-sunward direction is known as the magnetotail [*Baumjohann et al.*, 1996].

On the other hand, the dayside magnetopause and the magnetotail region can be subjected to magnetic reconnection process that involves the merging of anti-parallel magnetic field between two regions [*Baumjohann et al.*, 1996]. For example, configuration of a northward directed terrestrial magnetic field and a southward directed IMF at the dayside magnetopause, as well as the oppositely directed magnetic field between the northern and the southern magnetotail lobes. Magnetic reconnection is an important process that results in a non-zero flux transfer across the discontinuity, allowing the transfer of particles and energy between the solar and terrestrial systems, as well as within the terrestrial system [*Hones*, 1984].

The solar "extreme" ultraviolet (EUV) and UV light could dislodge a fraction of electrons by ionising the neutral atoms and molecules in the atmosphere. This in turn creates ionosphere, a region of permanent ionised population of electrically charged gas, separating the neutral atmosphere and the fully ionised magnetospheric plasma. At higher latitudes, charged particles with origins of solar wind and magnetospheric plasma can precipitate into the upper atmosphere along the magnetic field lines which intersect the North and South Poles, colliding and ionising the atmospheric neutrals. The emitted photons as a result of this ionisation process create the aurora, or commonly known as the northern and southern lights. [*Morrison and Owen*, 1996; *Baumjohann et al.*, 1996; *Kivelson and Russell*, 1995; *Chaisson and McMillan*, 1995].

This complex process of solar wind interaction with Earth which possess an intrinsic magnetic field is illustrated in Figure 2.1(a). Not that this illustration is not drawn to scale.

2.3 Solar wind interaction with Venus (unmagnetised body)

The previous section has shown that the presence of a strong intrinsic magnetic field can shield the terrestrial atmosphere from directly interacting with the highly ionised solar wind. As much as Venus is similar to Earth by only comparing their bulk properties (e.g. size, density, chemical composition), one of the biggest differences between these two planets is the absence of an intrinsic magnetic field on Venus. Nevertheless, studying the solar wind interaction with Venus would provide an opportunity to better understand the dynamics of a planet which an intrinsic magnetic field is absent.

Past studies have come to the conclusion that present day Venus does not possess an intrinsic magnetic field similar to that on Earth, though it could have had a dynamo planetary magnetic field for the first billion years of its life [*Stevenson*, 2003; *Russell et al.*, 1980; *Stevenson et al.*, 1983; *Luhmann and Russell*, 1997]. For a celestial body to generate a magnetic field, Dynamo Theory states that there must be (1) an electrically conductive fluid medium, (2) planetary rotational kinetic energy and (3) convective transferable internal energy [*de Pater and Lissauer*, 2001]. Hence Earth's magnetic field can be explained by its conductive molten iron outer core, continuous self-rotational characteristic and also a temperature flux from its core to its crust. However for Venus, the absence of magnetic field is unlikely due to its slow rotation (243 days compared to 1 day for Earth) [*Stevenson*, 2003]. *Stevenson* [2003] suggests that the absence of magnetic field could be due to the lack of heat convection as the inner core is not cooling [*Stevenson et al.*, 1983] or has already completely solidified.

A schematic diagram showing the topography of the solar-Venus environment is illustrated in Figure 2.1(b). Note that the illustration is not drawn to scale.

A bow shock will still form as the super-magnetosonic solar wind is abruptly slowed towards Venus. Similarly, a magnetosheath, a region of thermalised shocked solar wind is formed behind the shock. However, unlike Earth, Venus does not have a magnetosphere (dominated mainly by the strong terrestrial magnetic field) to deflect the solar wind. Hence, the IMF carried by the solar wind will pile up on top of the dayside ionopause, creating a region with high magnetic pressure called the 'magnetic barrier' (sometimes referred to the magnetic pile-up region) [*Zhang et al.*, 2008a]. These field lines will drape around the planet and create an induced magnetotail region in the nightside of Venus. Analogous to Earth's magnetopause, the Venusian ionopause is the boundary that separates the shocked solar wind and the planetary plasma.

As a matter of comparison, at the subsolar position (where sun is directly overhead of Venus), Earth's magnetopause has a stand off distance of around 10 R_E (Earth radii) [*Sibeck et al.*, 1991] while the nominal altitude of Venusian magnetopause stands around 1.05 R_V (Venus radius) during solar minimum [*Zhang et al.*, 2008a]. The large difference between the nominal altitudes of the Earth's and Venus's magnetopause demonstrates how contrasting the planetary boundaries can be for cases whether or not a planetary body is magnetised. An artistic comparison of the solar wind interaction between Earth and Venus is illustrated in Figure 2.2.

2.3.1 Dynamics of the ionosphere/ionopause

Without an intrinsic magnetic field, Venus' ionosphere is directly exposed to the incoming solar wind. However, the ionised particles populating the ionosphere are very good conductor. A current can be induced by the convecting magnetic field, which in turn can generate a cancelling field to prevent the shocked solar wind from penetrating. The

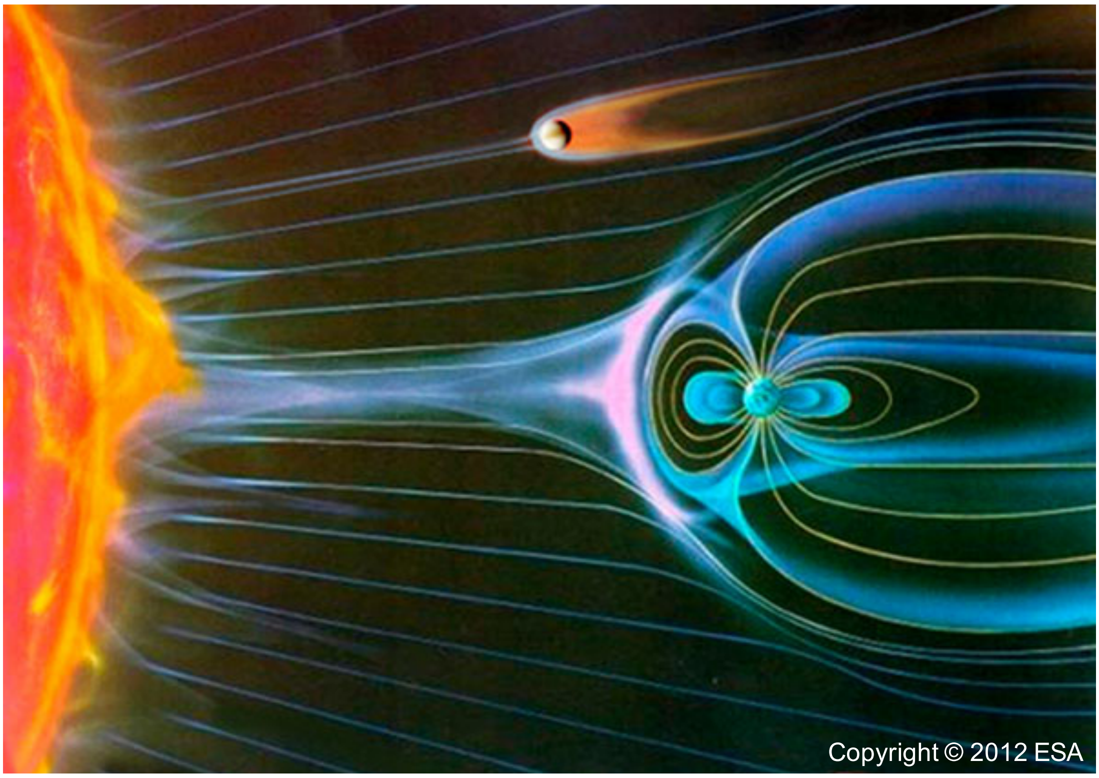

Figure 2.2: Artists impression of the solar wind interaction with Earth and Venus. Earth and Venus are depicted as the planetary bodies with and without an intrinsic magnetic field respectively. © Copyright: ESA 2012. ID: 207755

current induced field can always be generated as long as the magnetic field orientation constantly changes [*Kivelson and Russell*, 1995]. The ionopause forms at an altitude where the total pressure balance (i.e. the thermal (nk_BT), magnetic ($\mathbf{B}^2/2\mu_0$) and dynamic ($\rho\mathbf{v}^2$) pressures) between the ionosphere and magnetic barrier are in equilibrium [*Zwan and Wolf*, 1976; *Brace and Kliore*, 1991; *Brace et al.*, 1980]:

$$\sum^{MB}\left[nk_BT+\frac{\mathbf{B}_{MB}^2}{2\mu_0}+\rho\mathbf{v}^2\right]=\sum^{IO}\left[nk_BT+\frac{\mathbf{B}_{IO}^2}{2\mu_0}+\rho\mathbf{v}^2\right] \tag{2.1}$$

where $\sum$ of MB and IO denote the summations of all the pressure components in the magnetic barrier and ionosphere regions respectively. n, T, ρ and $\mathbf{v}$ are the plasma number density, temperature, density, and velocity along the normal direction of the ionopause. k_B and μ_0 are the Boltzmann's constant and free space magnetic permeability.

In the subsolar region, the total external pressure in the magnetic barrier is mainly dominated by the magnetic pressure where the thermal pressure is primarily converted into magnetic pressure [*Elphic et al.*, 1980] and the dynamic pressure becomes insignificant where the plasma velocity stagnates at the ionopause (hence $\rho\mathbf{v}^2 \rightarrow 0$) [*Luhmann*, 1986]. Hence ideally, the internal ionospheric thermal pressure itself can stand off the total external pressure in the magnetic barrier. However, this is not always the case. For example, under typical solar minimum environment where the incident solar irradiance decreases, the peak ionospheric thermal pressure is lower than the external pressure, the interplanetary flux can be easily forced into the ionosphere to supplement the total ionospheric pressure with magnetic pressure. This subsequently leads to the formation of ionopause at a lower altitude which allows the diffused magnetic field to magnetise the exposed ionised particles, creating a magnetised ionosphere. In contrast, during solar maximum when the ionospheric thermal pressure is strong enough to withstand the external pressure (85% of the time according to [*Luhmann*, 1986]), it results in a higher ionopause altitude where the ionosphere is mostly "field-free", leaving the ionosphere unmagnetised [*Luhmann et al.*, 1980; *Luhmann and Cravens*, 1991].

When the ionosphere is magnetised, the magnetic field in the magnetic barrier and the ionosphere regions are less distinguishable. On the other hand, when the ionosphere is unmagnetised, the ionospheric boundary can be clearly defined, where the ionosphere is often populated with small scale magnetic structure (e.g. flux ropes which will be discussed further in the following section) [*Elphic et al.*, 1980]. Moreover, the altitude where the ionopause forms is an important factor in plasma escape mechanisms, of which will be discussed in detail later. This is because the altitude of the ionopause can dictate the proportions of the atmospheric neutrals being eroded by the solar wind. Nonetheless, the ionopause can generally be characterised as a tangential discontinuity [*Knudsen et al.*, 1982; *Elphic and Ershkovich*, 1984] separating the dense ionospheric plasma from the tenuous solar wind plasma, where the total pressure is constant with no mass and magnetic flux across the boundary [*Baumjohann et al.*, 1996].

The total magnetic pressure in the magnetic barrier is primarily manifested from the incident solar wind dynamic pressure through the depletion of solar wind plasma [*Zwan and Wolf*, 1976; *Brace and Kliore*, 1991; *Brace et al.*, 1980]. However, as the plasma velocity is primarily in the direction along the Venus-Sun line, this implies that the exerted dynamic pressure will also vary depending on locations. For instance, the dynamic pressure is higher at lower Solar Zenith Angle [1] (SZA) where the radial components (relative to Venus) of the plasma velocity are maximal. In contrast, the dynamic pressure is lower at higher SZA where the radial components of the plasma velocity are minimal [*Phillips et al.*, 1986; *Brace et al.*, 1980; *Brace and Kliore*, 1991; *Luhmann*, 1986]. In another word, the altitude where the ionopause forms varies depending on locations. For instance, the nominal ionopause altitude at subsolar and terminator regions during solar maximum are ∼300 km and ∼900 km respectively [*Zhang et al.*, 2008a].

Unlike Mars [*Vogt et al.*, 2015] which is also an unmagnetised planet, Venusian ionopause is a well defined boundary and has a characteristic finite thickness that mostly ranges from 20 to 40 km [*Elphic et al.*, 1981]. Similar to the altitude, the thickness of ionospheric current sheet also varies with solar activities. For example, when the solar activity is higher, the ionopause forms at a higher altitude as a result of stronger ionospheric thermal pressure. At the same time, the plasma collisional effects decrease with increasing altitude and this results in a thinner current sheet. On the other hand, during quiet solar activity where the ionopause forms at lower altitude, collisional diffusion is responsible in broadening the current sheet [*Elphic et al.*, 1981]. Such properties of the ionospheric current sheet have so far only been explored with Pioneer Venus Orbiter (PVO) data over the solar maximum period. Similar variability is also expected during solar minimum and it will be one of the objectives in this thesis to be explored further.

2.4 Ionopause: wavelike appearance

The solar wind interaction with large planetary bodies like Venus can be described using magnetohydrodynamics (MHD) theory where the plasma is treated as a conducting fluid and its behaviours vary with the presence of a magnetic field. An in-depth intro-

---

[1] SZA is the angle between the zenith and the Sun. For example, SZA = 0° at subsolar point and SZA = 90° at the terminator region. Terminator is the the imaginary line separating the dayside and night side of Venus

duction to solar system magnetohydrodynamics can be found in *Siscoe* [1983]. For this reason, the Venusian ionopause is subjected to a number of macro, “fluid-like” instabilities [*Luhmann and Cravens*, 1991]. The two main instabilities are the Interchange (flute) Instability [*Arshukova et al.*, 2004] and the Kelvin-Helmholtz Instability (KHI) [*Chandrasekhar*, 1961].

The KHI is a macroinstability that is principally generated by the strong shear flows across a boundary [*Chandrasekhar*, 1961] and is an important mode of energy transfer at Venus [*Futaana et al.*, 2017]. Other contributing factors to the generation of KHI waves include the magnetic field orientation [*Lu et al.*, 2015], density gradient [*Amerstorfer et al.*, 2007; *Amerstorfer et al.*, 2010], temperature gradients [*Huba*, 1981], gyroviscosity or Finite Larmor Radius (FLR) [*Wolff et al.*, 1980], solar activities [*Biernat et al.*, 2007] and gravity [*Terada et al.*, 2002; *Elphic and Ershkovich*, 1984]. Detailed solutions to the KHI using MHD equations can be found in *Nagano* [1978, 1979]; *Wolff et al.* [1980]; *Elphic and Ershkovich* [1984]; *Terada et al.* [2002].

Generally, the following qualities possess destabilising effects: quasi-perpendicular orientation between the magnetic field and the wave vector as well as the flow velocity, lower density and higher temperature gradients across the ionopause, and lower planetary gravitational acceleration. The opposites are also true for the stabilising effects. Note that the FLR effects can be either stabilising or destabilising depending on the solar wind condition [*Wolff et al.*, 1980].

Even though the KHI is considered the more dominant instability for wave excitation, there are occasions when terms such as the magnetic field stress and boundary curvature are more significant, and can give rise to other instabilities, for example the Rayleigh-Taylor Instability (RTI) or Interchange (flute) Instability [*Elphic and Ershkovich*, 1984]. On the other hand, the Interchange (flute) Instability only grows when there is a non-monotonic plasma pressure gradient at the subsolar region [*Arshukova et al.*, 2004].

A schematic illustration of the ionospheric boundary wave phenomena is shown in Figure 2.3 (denoted in blue). A number of model simulations have demonstrated that the ionospheric boundary wave can arise when the ionopause is excited by these instabili-

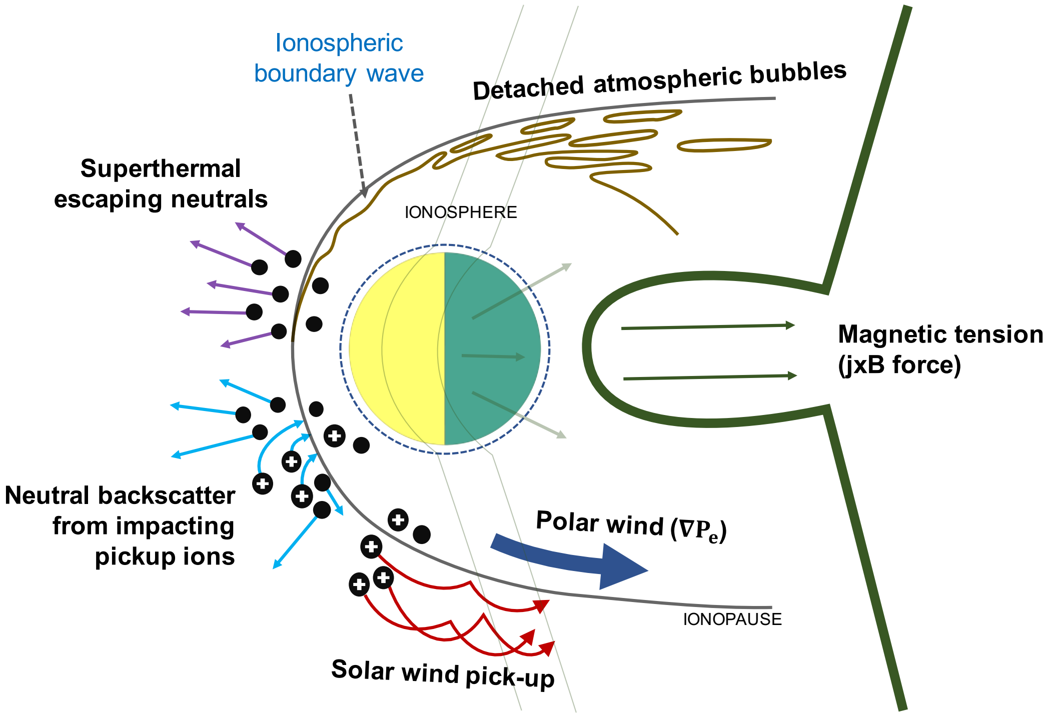

Figure 2.3: A schematic summary of all the dominant loss mechanisms of both ions and neutrals on Venus. After [*Futaana et al.*, 2017].

ties. *Wolff et al.* [1980] showed that the ionospheric boundary is unstable to KHI and illustrated the formation of flux ropes and atmospheric bubbles as a result of the ionospheric surface wave. The 2D model utilised in *Thomas and Winske* [1991] shows that the ionopause can be unstable as long as the magnetic field is perpendicular to the flow direction, even for very low velocity shears. *Terada et al.* [2002] used a two-dimensional global hybrid model to investigate the KHI at Venus and showed that the ionopause in the subsolar region is unstable to KHI. *Biernat et al.* [2007] studied the growth of the KHI at the Venusian ionopause and found that KHI can evolve regardless of the solar wind conditions. *Amerstorfer et al.* [2007] and *Amerstorfer et al.* [2010] showed that a density increase across the ionopause can influence the growth rate of KHI and characterised the evolution of the KHI into three main phases, i.e. linear, non-linear and turbulent phases.

However, *Möstl et al.* [2011] showed that the ionopause is not able to reach the non-linear vortex phase during either low or high solar activity due to the stabilizing density jump across the ionopause as well as the low ionopause altitudes. Though *Lu et al.* [2015] pointed out that *Möstl et al.* [2011] utilised the density ratio of solar wind condition to the ionosphere which is higher (more stabilising), rather than the density ratio of magnetic barrier to the ionosphere which is lower (less stabilising). In addition, using a 2.5D MHD simulations, *Zellinger et al.* [2012] shows that the gravity possesses an insignificant effect to the evolution of KHI and concluded that density increase has a more stabilising effect on the boundary layer than the gravity term. *Lu et al.* [2015] shows that boundary wave can still arise even for parallel magnetic field orientation which has a stabilising effect. The results also indicates that there is a critical value of the density ratio for which non-linear phase would not be reached if exceeded.

In addition to Venus, the development of the KHI has been studied at other planets. For example, *Penz et al.* [2004] suggests that KHI may lead to the detachments of ionospheric plasma clouds on Mars; *Sundberg et al.* [2010] observed dusk-side magnetospheric boundary wave at Mercury which could possible be excited by KHI; *Nykyri and Otto* [2001] shows that KHI at the magnetospheric boundary is responsible for the plasma transfer into the Earth's magnetotail; *Masters et al.* [2009] suggests that KHI is responsible for the magnetospheric boundary wave phenomena at Saturn; and *Goetz et al.* [2016] shows that the ionopause can be excited by the KHI as a result of high velocity shear at comet 67P/ChuryumovGerasimenko.

2.4.1 Flux ropes and atmospheric bubbles

When it is excited, model simulations have demonstrated that Venusian ionopause can exhibit a wavelike appearance. This wavelike appearance of the ionopause is an important characteristic of Venus and plays a significant role in its atmospheric evolution as well as the plasma energy exchange between the Sun and Venus. For instance, when the Venusian ionospheric boundary is excited by the KHI, the boundary wave can grow, become non-linear and subsequently reach a turbulent phase with non-regular structures [*Amerstorfer et al.*, 2010]. Results in *Lu et al.* [2015] shows that magnetic reconnection can be initiated when the KHI vortices are highly rolled up and islands of plasma irregularities can be formed. The vortices formed in the turbulent phase can eventually break up to create magnetic "flux ropes" and "atmospheric bubbles".

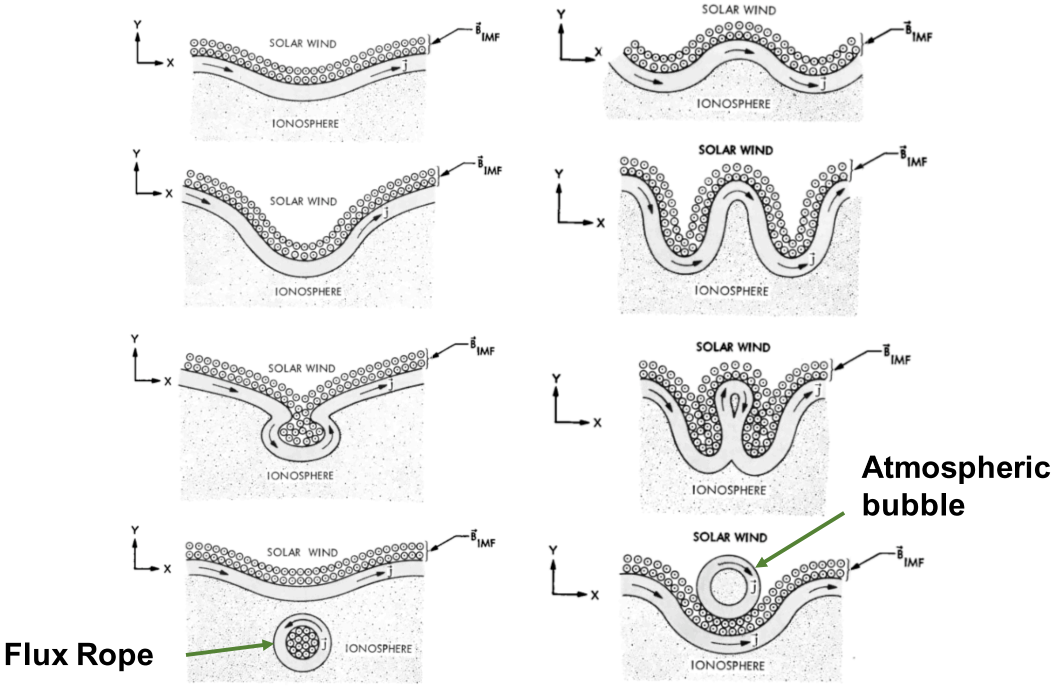

Figure 2.4: Illustrations of possible formations of (a) flux rope and (b) atmospheric bubble when the ionospheric boundary wave reach a turbulent state. After [*Wolff et al.*, 1980].

Their possible formation mechanisms are illustrated in Figure 2.4 (after [*Wolff et al.*, 1980]). The ionopause can be distorted as the boundary reaches turbulent state. As a result, compressed IMF and solar wind plasma which are trapped in a "current tube" can be formed in the ionosphere when the ionospheric current sheets reconnect. This current tube with plasma originated from the shocked solar wind is called a flux rope. Similarly, a current tube but with ionospheric plasma can also be formed outside the ionosphere, and it can be regarded as an atmospheric bubble.

Venusian flux ropes were first reported in *Russell and Elphic* [1979], since then they have been extensively researched [*Elphic and Russell*, 1983; *Elphic and Russell*, 1983; *Russell*, 1990; *Chen et al.*, 2017]. In addition to boundary wave reaching turbulent stage, flux ropes can also be generated by the mass loading mechanism. The mechanism presented in [*Russell*, 1990; *Wei et al.*, 2010] remarks the sinking of flux tubes into the ionosphere based on the balance between the downward curvature force and upward buoyancy force (due to the different densities between the flux tubes and the ionosphere). When the buoyancy force is stronger than the curvature force, the flux

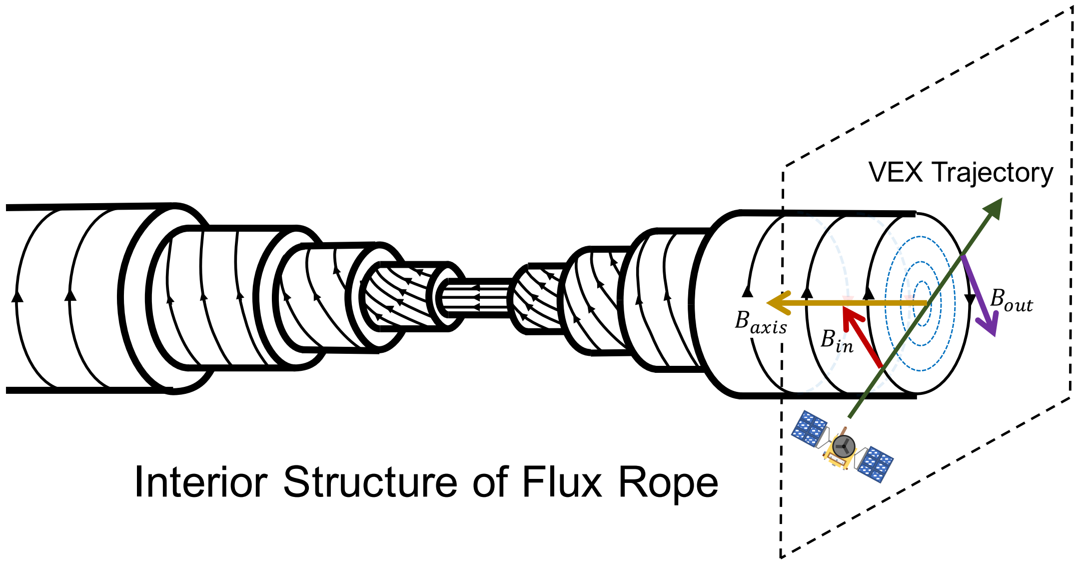

Figure 2.5: Illustration of the interior magnetic structure of a flux rope. (adapted from [*Russell and Elphic*, 1979]). The red, yellow and purple-coloured arrows represent the magnetic field lines of the inbound boundary, central axis and outbound boundary. The grey arrows represent the magnetic field lines between the boundaries and the axis. The green straight arrow representing the trajectory of VEX.

tubes will float on the ionospheric current sheet. These flux tube can become heavier as a result of photoionisation of the neutrals, eventually overcoming the buoyancy force and subsequently sink into the ionosphere.

Regardless of the generation mechanisms, as the flux ropes sink deeper into the ionosphere, the velocity shear relative to the quasi-stationary ionospheric plasma could provide the flux ropes with a helical structure [*Russell and Elphic*, 1979]. These flux ropes will twist and compress as they travel deeper into the ionosphere, resulting in a decrease in their diameters, which can be attributed to the Helical Kink Instability [*Russell*, 1990]. Its interior structure is illustrated in Figure 2.5. Flux ropes can be viewed as a magnetic structure with twisted solar wind field lines. The twisting and compressions of the magnetic field lines give flux rope a strong axial field, and the field becomes more azimuthal with increasing distance from the centre. Hence, spacecraft crossing through the flux rope will experience a three dimensional change in magnetic field direction, a unique signature of a flux rope.

A thorough review of the global characteristics of these magnetic flux ropes can be found in [*Elphic and Russell*, 1983; *Elphic and Russell*, 1983; *Chen et al.*, 2017]. According to the authors, flux ropes can be observed on more than 70% of the PVO orbits. They have higher spatial occurrences at lower altitudes and can occupy more than 50% of the ionospheric volume near 165 km. The radius of the flux ropes range from 6 km at an altitude of 160 km to 15 km at altitude of 500 km. They tend to have quasi-horizontal orientations at higher altitudes and more randomly orientated at lower altitudes. These flux ropes may enter into, slow down, 'pile up' in the denser ionosphere and are subsequently transported to the nightside region [*Russell and Elphic*, 1979]. As they twist and develop into three dimensional structures, they can interact with other flux ropes which have also become kink unstable to form more complex structures. These flux ropes may dissipate their respective magnetic flux through charge exchange and recombination with the surrounding ionosphere, which is becoming more resistive as the altitude decreases [*Russell*, 1990].

The atmospheric bubbles, sometimes referred to as "plasma clouds", possess plasma contents which are similar to those of ionospheric origins [*Brace et al.*, 1982]. They are primarily observed above the ionopause around the terminator and further downstream, a region which is regarded as the "cloud zone". The shapes of these clouds are not known as the authors suggested that they can appear in spherical or elongated shapes along the solar wind flow. In addition, only a small number of clouds (12 according to *Brace et al.* [1982]) are predicted to be present in the cloud zone at any given time. The fate of these atmospheric bubbles are not certain. They are likely to be convected downstream along with the solar wind bulk flow. The authors also discussed the roles of ionospheric surface wave in leading to the detachment of atmospheric bubbles. The estimated ion loss rate due to the convection of atmospheric bubbles ranges from 5×10^{24} to 7×10^{26} s^{-1} [*Lammer et al.*, 2006; *Brace et al.*, 1982; *Terada et al.*, 2002; *Amerstorfer et al.*, 2010]. If such process has been taking place on Venus since its formation, its role in the plasma removal mechanism will have been significant.

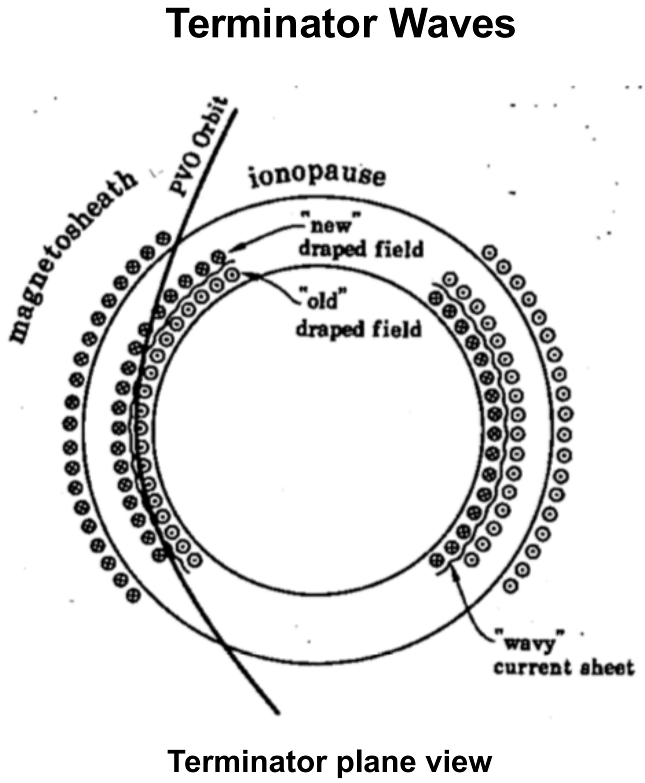

Figure 2.6: Illustrations of possible formations of "terminator wave" [after *Luhmann* [1990]]. Note the reversed orientations of the magnetic field lines.

2.4.2 Previous observational works

The ionospheric boundary has been demonstrated to be unstable to a number of instabilities. When it reaches turbulent phase, flux ropes and atmospheric bubbles can be created as illustrated in Figure 2.4. These plasma irregularities play an important role in Venusian atmospheric evolution and have been observed and researched extensively in the past. However, observational studies on ionospheric boundary wave events are rather limited and only short periods of PVO data (one to two orbits of data) have been utilised.

Using PVO data, *Luhmann* [1990] suggested the existence of "terminator wave" based on the significant field behaviour change of the observed flux ropes within 15° of the terminator. The authors suggested a possible mechanism by the reverse orientation of the IMF in the ionosphere and suggested its association with the formation of flux ropes as illustrated in Figure 2.6 (after *Luhmann* [1990]). *Brace et al.* [1980] observed large amplitude wavelike features in the vicinity of ionopause which the authors suggested propagating longitudinal waves or ionospheric surface waves. Such observations are always accompanied with ionopause altitude changes. The authors suggested that these wavelike features could be induced by the impulsive solar wind interactions with the ionosphere.

Brace et al. [1983] reported quasi-coherent wave trains that exist below 200 km which can represent vertical plasma motions. The authors regarded these waves as propagating trans-terminator ionospheric waves into the nightside and suggested a potential energy source from the plasma pressure gradient driven interchange instabilities or the ion-neutral drag driven shear instabilities. *Pope et al.* [2009] and *Walker et al.* [2011] suggested that nonlinear vortex-like structures observed in the magnetosheath region using Venus Express (VEX) magnetic field data were associated with the strong shear flow across the ionopause. However, the altitudes of these observations are not consistent with the nominal ionopause altitude.

2.4.3 Atmospheric evolution of Venus

There are a number of particle escape mechanisms from the upper atmosphere of Venus and they are summarised in a schematic diagram in Figure 2.3. One of the processes is the detachment of plasma clouds as a result of turbulent boundary as discussed previously. All of these processes are well summarised in *Lammer et al.* [2008], *Lammer et al.* [2006], *Brain et al.* [2016] and references therein. A synopsis discussion of these mechanisms will be described briefly in this section. Generally, neutral atmospheric particles can escape from a planetary body as long as they have sufficient energy to reach the escape velocity to overcome its gravitational inward pull. The escape velocity of a planetary body at a particular distance can be determined by

$$v_e = \sqrt{\frac{2GM_p}{r}} \tag{2.2}$$

where G is the universal gravitational constant, M_p is the mass of the planetary body, and r is the altitude where the particles escape. Hence for Venus, a G of 6.67 ×

10^{-11} m^3 kg^{-1} s^{-2}, M_p of 4.87×10^{24} kg and r of 6052 km give an escape velocity of $\approx$ 10.34 km s^{-1}. Note that the value of escape velocity varies with the distance of the particles from the planet. Hence, if the nominal ionopause altitude of 250 km is considered instead, v_e would decrease to $\approx$ 10.15 km s^{-1}, indicating less energy is needed for the particles to escape from the ionosphere compared to those from the surface. This would then correspond to an escape energy of $\approx$ 8.54 eV for O* and $\approx$ 0.54 eV for H*. * indicates hot and energetic photochemically produced atoms.

The atmospheric escape mechanisms can primarily be characterised into two categories, depending if the particles are in neutral or charged states.

Neutral particles

1. Thermal escape (or Jeans escape) [*Chamberlain*, 1961; *Öpik and Singer*, 1961]: Atoms with velocity that exceeds the escape velocity in the exosphere can escape into the space. However, the low temperature in the collisionless exosphere of Venus is not able to provide the hydrogen atoms enough energy to overcome the escape energy [*Lammer et al.*, 2008]. Hence, the loss of hydrogen through this process is negligible Venus, let alone the heavier atoms which higher energy is needed to escape.

2. Photochemical escape: The dissociative recombinations of molecular atmospheric ions would form neutral atoms with large velocity. The productions of hot H* atoms of all possible photochemical reactions have sufficient energy to escape from the planet. However, the energy of the productions of O* atoms are not sufficient to escape [*Dubinin et al.*, 2012]. The highest energy of all the possible formations of hot O* atoms is 6.96 eV [*Kella et al.*, 1997] which is much lower than the escape energy (8.54 eV) of O* atoms.

3. Sputtering [*Luhmann and Kozyra*, 1991]: The atmospheric neutral particles can be accelerated and subsequently ejected into the space when incident charged particles interact with the neutrals in the collisional region of the atmosphere. It is important to mention that these accelerated particles are also subjected to

photodissociation and photoionisation processes, which are then picked up by the solar wind as charged particles instead.

In addition to thermal energy, charged particles can be influenced by the external magnetic and electric field. Hence, there is a difference in the escape mechanism between the neutral and charged particles.

Charged particles

1. Solar wind pick up: A convection electric field ($\mathbf{E} = -\mathbf{v} \times \mathbf{B}$) can be generated by the solar wind flowing past the ionosphere. This electric field can accelerate the planetary ions (mainly the H^+ and O^+) from the exosphere up to twice the solar wind velocity [*Futaana et al.*, 2017].
2. Hall electric field: Curved magnetic field lines can induce an electric field ($\mathbf{E} = \mathbf{j} \times \mathbf{B}$) which can accelerate and remove “blobs” of atmospheric particles from Venus. This process is only effective in regions where the field lines are curved, such as the polar regions and the magnetotail region mainly due to solar wind field lines draping around Venus [*Dubinin et al.*, 2013; *Futaana et al.*, 2017].
3. Polar wind [*Collinson et al.*, 2016]: An electric field ($\mathbf{E} = \nabla \cdot \mathbf{P_e}$) can also be generated by electron pressure gradients which can direct the atmospheric charged particles away. These ambipolar fields result in ion outflow from the magnetic cusps on Earth hence it is referred to as the polar wind.
4. Detached plasma clouds/atmospheric bubbles [*Brace et al.*, 1982]: As discussed earlier, ionospheric plasma clouds can be formed as a result of ionospheric boundary wave reaching nonlinear stage. These clouds of plasma are sometimes referred to atmospheric bubbles.

A summary of the estimated loss rates for different mechanisms are tabulated in Table 2.2. Note that these values are estimated using simulation studies summarised in *Lammer et al.* [2006], *Lammer et al.* [2008], and references therein. In addition, it can

Table 2.2: Average Venusian upper atmosphere escape rates. After [*Lammer et al.*, 2006; *Lammer et al.*, 2008].

Escape Process	Loss rate (s^{-1})
Neutrals particles	
Jeans: H	2.5×10^{19}
Photo-chemical reactions: H*	3.8×10^{25}
Sputtering: O	6×10^{24}
Charged particles	
Electric field force: H^+	$\leq 7 \times 10^{25}$
Ion pick up: H^+	1×10^{25}
Ion pick up: H_2^+	$< 10^{23}$
Ion pick up: O^+	1.6×10^{25}
Detached plasma clouds[a] : O^+	$5 \times 10^{24} - 7 \times 10^{26}$

[a] The range of limits is obtained from *Lammer et al.* [2006]; *Brace et al.* [1982]; *Terada et al.* [2002]; *Amerstorfer et al.* [2010].

be observed from Table 2.2 that the detachments of atmospheric bubbles yields the highest plasma loss rate (if the higher end of the estimated range is considered) among all the suggested mechanisms.

Similar atmospheric escape mechanisms also take place in other unmagnetised bodies [*Brain et al.*, 2016]. The importance of each role on different planets is dependent on a combination of the planetary properties as well as the external conditions. For instance, compared to Venus which is larger, the thermal and photochemical escapes play more important roles in the atmospheric removal process for Mars. This is because lower energy is needed to reach the escape velocity of ≈ 5 km s^{-1}, even though the Venusian atmosphere receives more energy from the solar radiation (simply because of its close proximity to the Sun). Figure 2.7 summarises the relationship between the escape velocity and the distance from the Sun (measured in surface temperature) of some solar system bodies.

Venus Express plasma measurements show that the estimated escape rate for hydrogen is approximately twice (≈ 1.9) that of oxygen [*Barabash et al.*, 2007]. This ratio corresponds approximately to the stoichiometric ratio of the number of hydrogen to oxygen

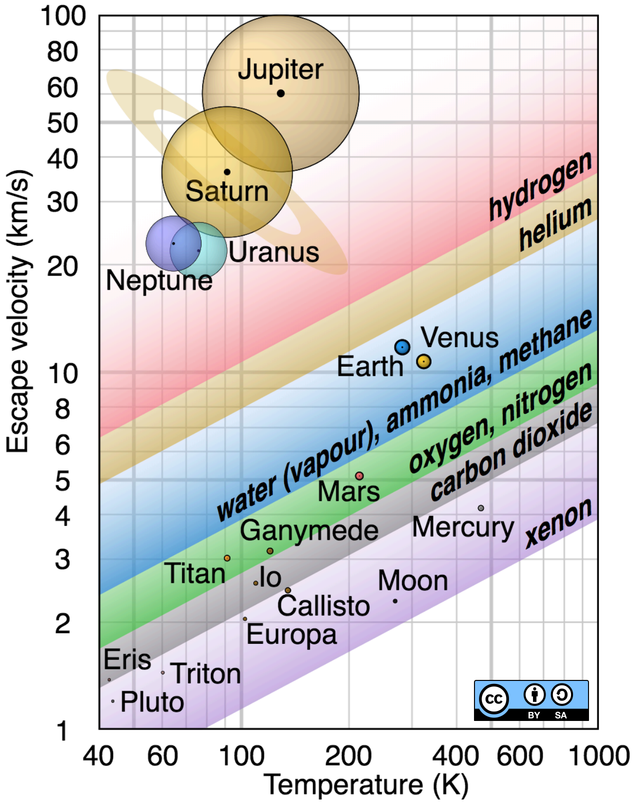

Figure 2.7: Graphs of escape velocity against the distance from the Sun (measured in surface temperature) of some planetary bodies. The retained gases are also shown. The objects are drawn to scale. This figure is utilised under the Creative Commons Attribution-Share Alike 3.0 Unported license.

atoms of a water molecule (2:1). In another word, present day Venus could still be losing water molecules from the already low water content atmosphere (20 ppm (parts per million)) to space. Even with a small plasma loss rate, a prolonged period of all the discussed plasma removal mechanisms play a fundamental role in removing the ocean of liquid water that once existed on Venus surface [*Way et al.*, 2016].

2.5 Motivations and outstanding questions

From the early observations and radar mapping from Earth surface, to spacecraft flybys, orbiters and landings, past and current missions have allowed us to better understand Venus. However, there are still a lot of outstanding questions that are yet to be answered. By using the data from Venus Express, this thesis will focus particularly on the stability and the dynamics of the ionopause in relation to the incoming solar wind in order to contribute to the following:

1. Model simulations demonstrated that the ionopause can exhibit a wavelike appearance, but the observational studies on this subject are very limited. Does the ionopause always exhibit a wavelike appearance or does its occurrence depend on certain parameters?
2. What are the dynamics of the ionospheric current sheet? Do its parameters (e.g. thickness and altitude) vary with internal and external conditions?
3. What is the global distribution of the ionospheric boundary waves? What are their general characteristics (e.g. sizes, altitudes, propagation direction, etc.)?
4. Model simulations demonstrate that atmospheric bubbles and flux ropes can be the end products of a boundary wave. Can this relationship be directly evidenced from observational studies?
5. Based on their characteristics, can the ionospheric flux ropes be categorised depending on their production mechanisms (e.g. mass loading or turbulent boundary wave)?
6. Is the boundary wave excited and generated only by KHI as demonstrated from the simulation studies? Can boundary waves arise as a result of ionopause altitude fluctuations [*Brace et al.*, 1980] or the reverse in magnetic field orientations [*Luhmann*, 1990]?
7. How important is the role boundary wave events play in the atmospheric evolution at Venus? Could water be removed as a result of ionospheric boundary wave?

All of these questions are addressed and discussed directly in this thesis. The findings contribute to our understanding of the dynamics of the solar wind interaction with Venus, and unmagnetised bodies in general. Moreover, the results establish a better perspective on the planetary atmospheric evolutions. The novel contributions of this thesis are summarised in Chapter 1.2. They will be discussed more in details in the "Contribution" sections in each of the following chapters: Chapter 4, 5 and 6 respectively.

Chapter 3

Instrumentations and methodology

3.1 Introduction

This chapter will present an overview of the instruments onboard VEX which the data will be utilised for analysis in this thesis. In addition, Minimum Variance Analysis, a data analysis technique that will be employed in this thesis will also be introduced in this chapter.

3.2 Venus Express

Venus Express (VEX) is the European Space Agency (ESA)s first European Mission to Venus. It was launched in November 2005 during solar minimum from the Baikonour Cosmodrone in Kazakhstan, took a journey of about 5 months and arrived at Venus in April 2006 [*Svedhem et al.*, 2007; *Titov et al.*, 2006]. VEX was fairly similar to Mars Express apart from few modifications to account for the independent differences between Venus and Mars [*Svedhem et al.*, 2009]. VEX spacecraft was in an elliptical polar orbit with apoapsis distance of 66,000 km for a 24 hour period and latitude of about 78 °N. Due to the solar gravity perturbations, the periapsis changed around 1 to

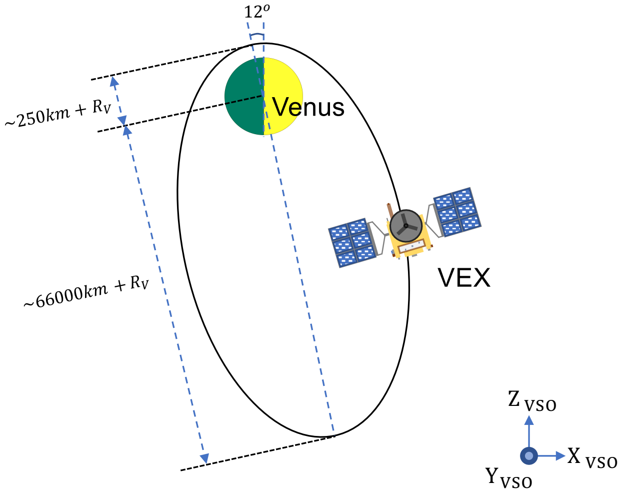

Figure 3.1: An illustrative diagram showing the orbital details of the Venus Express.

2 kilometres per day but it was maintained in a range of 130 to 463 kilometres [*Titov et al.*, 2006; *Svedhem et al.*, 2007]. An illustrative diagram is shown in Figure 3.1.

The objectives of the VEX mission are mainly focussed on understanding the Venus planetary dynamics:

1. Solar wind interaction with the Venusian plasma environment
2. Greenhouse effect on Venus
3. Characteristic cloud system
4. Atmospheric escape mechanisms
5. Venus surface infra-red topography
6. Volcanic and seismic activity on Venus

3.2.1 Magnetometer

The magnetic field was measured by the VEX Fluxgate Magnetometer (MAG) which consisted of two triaxial fluxgate sensors [*Zhang et al.*, 2006]. When the spacecraft was nearer to the planet, the magnetometer would be switched on at a rate of 32 Hz to enable more data to be recorded but was maintained at standard mode of 1 Hz otherwise. VEX also operated in 128 Hz "Burst" mode for two minutes at periapsis. The data used in this research has been cleaned for dynamic stray fields [*Pope et al.*,

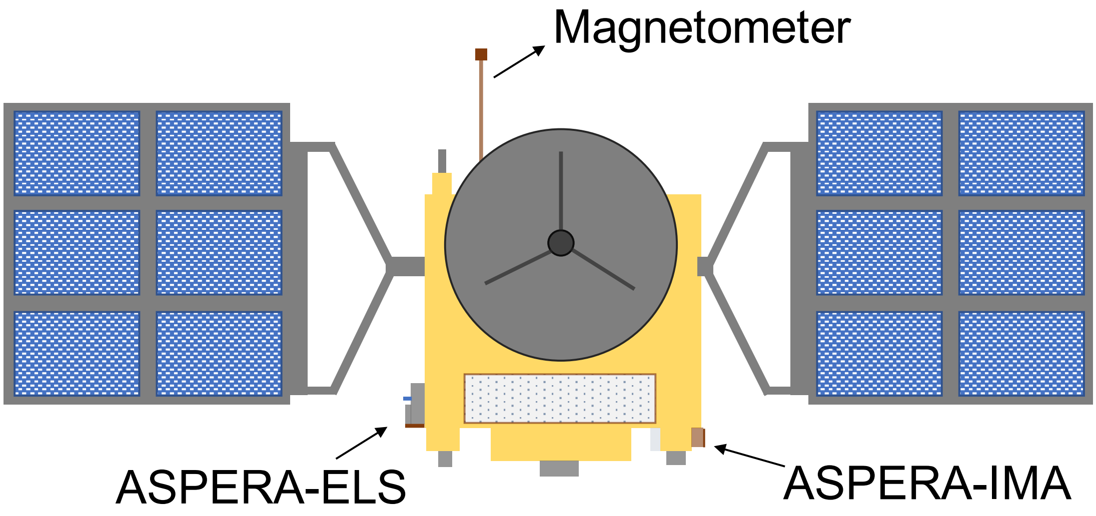

Figure 3.2: An illustrative diagram of Venus Express showing the positions of the magnetometer, ASPERA-IMA and ASPERA-ELS.

2011] and corrected for offset [*Leinweber et al.*, 2008]. 1 Hz data is used in this thesis and 32 Hz data will be used where available.

3.2.2 ASPERA-4

The Analyser of Space Plasmas and Energetic Atoms (ASPERA-4) onboard VEX included four sensors; electron spectrometer (ELS), ion mass analyser (IMA), neutral particle imager (NPI) and neutral particle detector (NPD) [*Barabash et al.*, 2007]. Only ELS and IMA data are used in this paper.

The ELS had 16 sectors of 22.5° covering the full 360° cycle. ELS provides electron energy spectra in several modes, two of which is used in this thesis: an electron spectrum between 0.9 eV to 15 keV is generated every 4s with an approximate energy resolution ($\Delta E/E$) of 7% (the energy resolution is energy and sector dependent) and an electron spectrum between 9 eV to 250 eV is generated every 1s with an approximate energy of 7%. Both ranges of electron energy cover the electron populations used to characterise the planetary regions and will be utilised in this thesis. Only data from anodes 5 to 12 of ELS will be used in this work as they provide unobstructed view.

The ion measurements provided by the IMA are in the energy range 0.01-36 keV/q

Table 3.1: The performance of the ELS and IMA. Extracted from *Barabash et al.* [2007].

Parameter	ELS	IMA
Particles to be measure	Electrons	Ions
Energy, keV per change	0.01-15	0.01-36
Energy resolution, $\triangle E/E$	0.07	0.07
Mass Resolution	-	m/q=1,2,4,8,16,32, >40
Intrinsic field of view	$10° \times 360°$	$90° \times 360°$
Angular resolution, FWHM	$10° \times 22.5°$	$4.5° \times 22.5°$
G-factor/pixel, cm^2 sr	7×10^{-5}	3.5×10^{-4}
Efficiency, %	Incl. in G-factor	Incl. in G-factor
Time resolution (full 3D), s	32	196
Mass, Kg	0.3	2.4

with sampling time of 192 seconds and an energy resolution of $\Delta E/E$ of 0.07. Its mass resolution covers the H^+, H_2^+, H^{2+}, O^+ and the groups of heavy ion with molecular mass to charge ratio, $20 < M/q < 80$ amu/q. Ion moment data (density, velocity and temperature) can be derived from the particle counters [*Fränz et al.*, 2007]. Only the data from magnetometer, ELS and IMA will be used in this work. A diagram showing the locations of these three instruments on VEX is displayed in Figure 3.2. A comparison between ELS and IMA is summarised in Table 3.1.

3.2.3 Remarks

The data have been rotated into the Venus Solar Orbital (VSO) coordinate frame; with $+X_{VSO}$ in the Venus-Sun direction, $+Y_{VSO}$ perpendicular to $+X_{VSO}$ and in the direction of the orbital motion of Venus, and $+Z_{VSO}$ is orthogonal to complete the right hand set of axes. Illustration is provided in the lower right corner in Figure 3.1.

Particle and low resolution magnetic field data are available from the data centre at Centre de Donnes de la Physique des Plasmas (http://amda.cdpp.eu/) and from the ESA Planetary System Archive (PSA) at https://www.cosmos.esa.int/web/psa/. High resolution MAG data is available on request from the VEX - MAG PI, TieLong Zhang.

After conducting a statistical survey of the available data for the entire mission duration, it is found that there is a time drift up to 10 seconds on the ASPERA-4 instruments. After raising this issue with the ELS team, they mentioned that the offsets could be due to the uniform time drift on the ASPERA-4 clock and more information will be provided as soon as the issue is identified. All the ELS data used in this work have been manually time-shifted in conjunction to the magnetometer.

In addition, the survey also found that a small number of the IMA ion moment data are inaccurately calibrated. After discussing with the IMA team, it is due to electronics noise resulting from low temperatures which was not cleaned by standard processing. Hence, the noise has been misidentified by the processing procedure as the pickup ions populations which causes an abnormality in the calibrated data. The data has not been reprocessed at the time of writing. As a result, all the inaccurate ion data are not considered in this work.

3.2.4 Comparison to PVO

Figure 3.3 shows a comparison between the VEX and PVO operating periods based on the sunspots number. In contrast to PVO which was able to sample the Venusian ionosphere around the subsolar region during the solar maximum period, the high latitude elliptical polar orbit of VEX provides an opportunity to study the dynamics of the Venusian ionosphere in the northern polar region of Venus during solar minimum. This allows the work conducted in this thesis to complement those conducted using PVO data that covers mainly the solar maximum period.

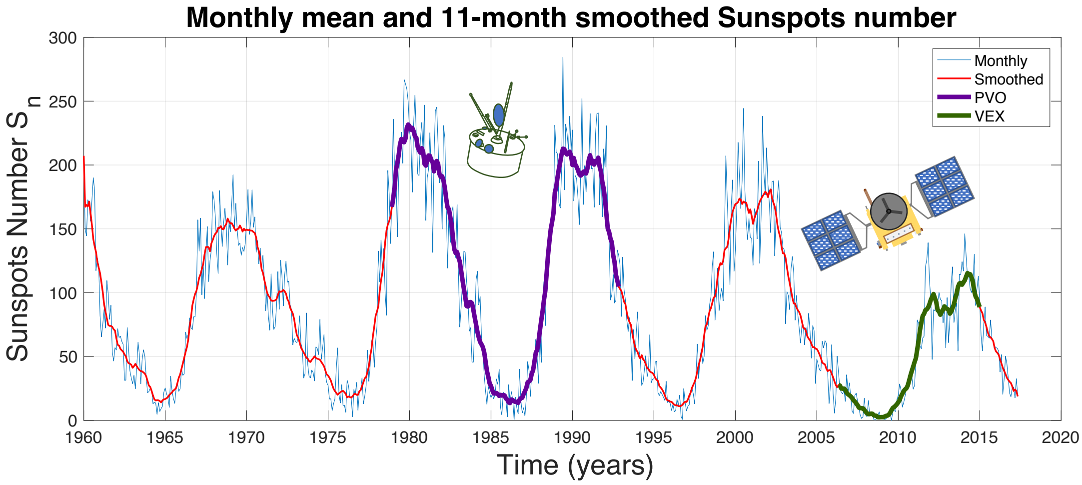

Figure 3.3: Operating periods of VEX and PVO based on the sunspots number. The sunspots number was obtained from the GSFC/SPDF OMNIWeb interface at https://omniweb.gsfc.nasa.gov.

3.3 Minimum Variance Analysis

The two primary aims of using MV analysis in this work are to find (1) the discontinuity conditions of boundary crossings (e.g. tangential or rotational) and (2) to estimate the normal directions of the boundary crossings using MAG data.

The principal objective of the MV analysis technique is “to find, from single-spacecraft data, an estimator for the direction normal to a one-dimensional or approximately one-dimensional current layer, wave front, or other transition layer in a plasma.” [*Sonnerup and Scheible*, 1998]. It was first employed in *Sonnerup and Cahill* [1967] to determine the vector normal to the magnetopause. More specifically, MV analysis will be utilised to transform the magnetic field measurements from the VSO coordinates into the boundary normal coordinates. For instance, the minimum variance direction resulted from MV analysis of a boundary crossing is directed along the minimum change in magnetic field magnitude, which can be used as an estimator for the normal direction of a boundary crossing of tangential discontinuity (i.e. Venus ionopause). The intermediate and maximum variance directions will complete a right angle plane tangential to the normal direction.

The three pairs of eigenvectors V_i and eigenvalues λ_i from the magnetic variance matrix M (Equation 3.1) are orthogonal and correspond to each other. For example, eigenvector V_{min} corresponds to the smallest eigenvalue λ_{min}. In addition, the eigenvectors represent the minimum, intermediate and maximum variance directions respectively. In this work, the smallest value of eigenvalue λ_{min} correspond to the minimum variance direction V_{min}, the largest value of eigenvalue λ_{max} correspond to the maximum variance direction V_{max} and eigenvalue λ_{int} correspond to the intermediate variance direction V_{int}.

The working procedures to obtain the magnetic variance matrix M over an interval of MAG data with 1:N vector measurements are summarised as below:

$$M = \begin{bmatrix} m_{xx} & m_{xy} & m_{xz} \\ m_{yx} & m_{yy} & m_{yz} \\ m_{zx} & m_{zy} & m_{zz} \end{bmatrix} \tag{3.1}$$

$$m_{ij} = \langle B_i B_j \rangle - \langle B_i \rangle \langle B_j \rangle \tag{3.2}$$

$$\langle B_i B_j \rangle = \sum_{m=1}^{N} \frac{(B_i B_j)}{N} \tag{3.3}$$

$$\langle B_i \rangle = \sum_{m=1}^{N} \frac{B_i}{N} \tag{3.4}$$

where i and j represent the directions X, Y and Z. N is the total number of vector measurements.

Each of the three pair of eigenvectors V_i and eigenvalues λ_i can then be determined from the magnetic variance matrix M by solving Equation 3.5.

$$MV_i = \lambda_i V_i \tag{3.5}$$

V_{min} the minimum variance direction is used as an estimator for the normal direction of a boundary crossing of tangential discontinuity. The magnetic field components in the minimum variance direction, $B_n = B_{min} = B \times V_{min}$. Similarly, The magnetic field components in the intermediate and maximum variance directions are $B_{int} = B \times V_{int}$ and $B_{max} = B \times V_{max}$ respectively. B_{min}, B_{int} and B_{max} are orthogonal to each other.

3.3.1 Useful Parameters

There are a few primary parameters which are used to define the nature of the results. They are described as below:

1. Note that V_{min}, the normal directions estimated using the MV analysis method are not always well-defined. *Lepping and Behannon* [1980] shows that $\lambda_{int}/\lambda_{min}$ is an important statistical indicator of how well defined the normal directions are. Lower values of $\lambda_{int}/\lambda_{min}$ imply poorly determined variance qualities. In particular, the authors showed that variance qualities cannot be accurately determined for $\lambda_{int}/\lambda_{min} < \sim 1.8$. Earlier works [*Sonnerup and Cahill*, 1967; *Behannon et al.*, 1981; *Smith*, 1973; *Lepping and Behannon*, 1980] required $\lambda_{int}/\lambda_{min}$ of at least 1.5-2.5. In this thesis, $\lambda_{int}/\lambda_{min} \geq 3$ is adopted to ensure well-defined estimated normal directions of boundary crossings.
2. The discontinuity jump conditions are important to classify whether a current layer is a tangential or rotational discontinuity. For example, the Venusian ionopause can be characterised by a tangential discontinuity [*Wolff et al.*, 1979] where the $|B_n|$ across the current sheet is zero [*Sonnerup and Scheible*, 1998]. In this thesis, we follow the criteria that was first introduced by *Smith* [1973] and was later adopted by *Neugebauer et al.* [1984]; *Horbury et al.* [2001]; *Söding et al.* [2001]; *Knetter et al.* [2004] to differentiate these two discontinuities based on the values of $|B_n|/|B|$ and $|\triangle B|/|B|$, where $|B_n|$ is the magnetic field component normal to the discontinuity surface, $|B|$ is the larger field magnitudes on either side of the discontinuity and $|\triangle B|$ is the change of the field magnitude across the boundary. The criteria are summarised in Table 3.2.

3.3.2 Statistical Error Estimates

The estimations of the eigenvectors (e.g. V_{min}, V_{int} and V_{max}) can result in statistical uncertainties [*Sonnerup and Scheible*, 1998]. These statistical errors can be estimated by the use of standard analytical approach. Such approach has been shown to be com-

Table 3.2: A table of the criteria to differentiate tangential and rotational discontinuities. Adopted from *Knetter et al.* [2004].

Discontinuities	$\lvert B_n \rvert / \lvert B \rvert$	$\lvert \triangle B \rvert / \lvert B \rvert$
Rotational	≥ 0.4	< 0.2
Tangential	< 0.4	≥ 0.2
Either	< 0.4	< 0.2
Neither	≥ 0.4	≥ 0.2

parable to the use of computational techniques such as the bootstrap method [*Khrabrov and Sonnerup*, 1998].

$\lvert \triangle\varphi_{i,j} \rvert$, the angular uncertainty of V_i for rotation toward or away from V_j can be estimated as below:

$$\lvert \triangle\varphi_{i,j} \rvert = \lvert \triangle\varphi_{j,i} \rvert = \sqrt{\frac{\lambda_{min}}{N-1}\frac{(\lambda_i + \lambda_j - \lambda_{min})}{(\lambda_i - \lambda_j)^2}} \tag{3.6}$$

where i and j can be min, int, and max, but $i \neq j$. For instance, $\lvert \triangle\varphi_{min,int} \rvert$ would represent the angular uncertainty between V_{min} and V_{int}. If $\lambda_{int}/\lambda_{min}$ of 3 and N = 6 are considered, then the resulting $\lvert \triangle\varphi_{min,int} \rvert = \pm\ 0.387$ rad $= \pm\ 22.2°$. Note that this value of uncertainty is obtained by utilising the lower limits of $\lambda_{int}/\lambda_{min}$ and N considered in this thesis. Where in fact, the values of $\lambda_{int}/\lambda_{min}$ and N resulted from the MV analysis implemented in this thesis (which will be discussed further in Chapter 4 and Chapter 5) are shown to be higher. This would result in much smaller hence insignificant uncertainties. Therefore, statistical uncertainties resulted from the MV analysis approach will not be considered in this thesis.

Chapter 4

Ionospheric boundary wave: Detailed single observational study

4.1 Introduction

Past simulation works summarised in Chapter 2.4 have shown that the Venusian ionopause can be unstable to macroinstabilities (e.g. KHI *Terada et al.* [2002]; *Biernat et al.* [2007]) and can exist with a wavelike appearance. This wavelike property of the ionopause has also been frequently depicted in a number of illustrations [*Brace et al.*, 1987; *Luhmann and Kozyra*, 1991], and is closely linked to the observations of flux ropes [*Russell and Elphic*, 1979] and atmospheric bubbles [*Brace et al.*, 1982]. These plasma irregularities play important roles in the energy transfer between the solar wind and the Venusian atmosphere.

VEX's high latitude and highly elliptical polar orbits provide an ideal opportunity to study the fluctuations of the ionopause boundary, as the tangential velocity shear flow, which is the primary seed for the development of the KHI [*Chandrasekhar*, 1961], is large in the terminator region [*Knudsen et al.*, 1980]. Despite the significances of the ionospheric boundary wave, the observational studies of such events are rather limited and are mostly conducted with PVO data [*Luhmann*, 1990; *Brace et al.*, 1980; *Brace et al.*, 1983].

In this chapter, a detailed analysis of evidence of boundary waves in the vicinity of the terminator observed on 26 June 2006 is presented. High resolution data of IMA and ELS of ASPERA-4, as well as the MAG on board of VEX will be utilised to characterise this event. An approach is implemented to identify potential ionospheric boundary crossings. Coupled with MV analysis, this approach is able to demonstrate whether or not these boundary crossings are 'smooth'. We investigate the evolution of these boundary waves in the terminator region of the ionopause by examining a sequence of magnetic oscillations. On 26 June 2006, within the boundary wave, evidence is shown for the existence of a magnetic flux rope. The observation of boundary waves in this study is fundamental in explaining the observations of atmospheric bubbles outside the ionosphere [*Brace et al.*, 1980, 1982]. Finally, their dynamics are discussed and their properties are shown to be consistent with a previously proposed generation mechanism which may contribute to Venusian atmospheric evolution.

4.2 VEX pass on 26 June 2006: Pulse-like Photoelectron Dropout

Figure 4.1 shows the (a) VEX trajectory, (b) the electron energy-time spectrogram of count rate, (c) ion energy-time spectrogram of count rate and (d) 1Hz magnetic field magnitude plot. The yellow, red, purple and green coloured parts of the trajectory plot reflect the different regions VEX was in, i.e. the unshocked solar wind, magnetosheath, magnetic barrier and ionosphere regions respectively. They are also reflected in the coloured bar above (b). The nominal altitudes of bow shock (BS), induced magnetopause (MP) and ionopause (IP) are represented in blue, red and green dashed lines respectively [*Zhang et al.*, 2008b,a]. The actual crossings of the bow shock and ionopause are marked with golden circle and their respective time crossings. Note that since the location of the bow shock is highly variable, which can be due to the variation

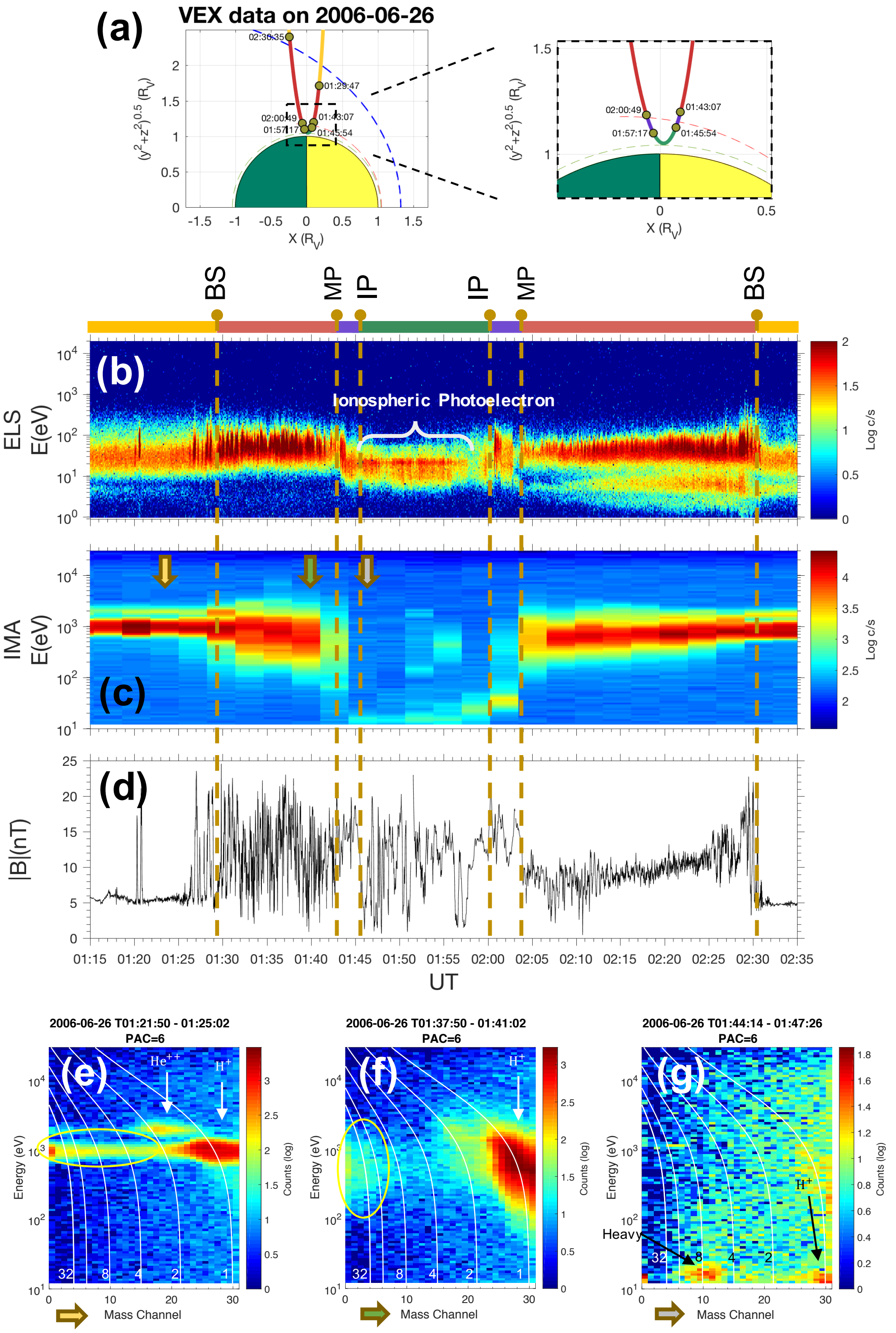

Figure 4.1: VEX pass from 01:15 UT to 02:35 UT on 26 June 2006. (a) The VEX trajectory plot in R_V (Venus radii), (b) electron energy-time spectrogram of count rate obtained from ELS, (c) ion energy-time spectrogram of count rate obtained from IMA and (d) 1-Hz magnetic field magnitude plots otained from MAG. (e), (f) and (g) are the energy-mass channel plots of the ion populations in different regions indicated with the yellow, green and grey coloured arrows in (c). Full figure description can be found the the body of the main text.

of the solar EUV, solar wind Mach number and IMF orientation [*Zhang et al.*, 2008b], the observed altitudes of the bow shock are comparably different than the nominal locations.

On 26 June 2006, the spacecraft was orbiting Venus quasi-along the terminator plane ($X_{VSO} = 0$, Y-Z $_{VSO}$ plane). The angle between the orbital and the terminator plane is about 6°. The unshocked solar wind (yellow bar) was rather quiet. This is reflected from the low and broad solar wind electron energy around 20-40 eV in Figure 4.1(b) and the minimal magnetic field fluctuation around 5 nT in Figure 4.1(d). The inbound bow shock was crossed at around 01:30 UT (at an altitude of about 4477 km) with a sudden appearance of high energetic electron populations in the magnetosheath region. This bow shock crossing is a typical example of a quasi-parallel shock. The shock angle θ_{Bn} is $\approx 30°$, based on a mean average value obtained using MV analysis (32°) [*Sonnerup and Scheible*, 1998; *Sonnerup and Cahill*, 1968], Coplanarity (34°) [*Schwartz*, 1998, and references therein] and model Bow shock (24°) [*Zhang et al.*, 2008b]. There are some notable oscillations prior to crossing the bow shock at around 01:30 UT on 26 June 2006. These structures could be attributed to either foreshock magnetic structures (e.g. Short Large Amplitude Magnetic Structures (SLAMS) [*Collinson et al.*, 2012]) or multiple shocks crossings. Such magnetic oscillations are quite common for quasi-parallel shocks like this inbound bow shock crossing on 26 June 2006.

As the spacecraft crossed the bow shock into the magnetosheath (red bar), the incoming solar wind electrons are heated by the shock, broadening the electron energy distribution. The broad energy intensity (ranging from ∼11 eV to ∼70 eV) in this region can be seen to become narrower towards the lower boundary of the magnetosheath. At around 01:43 UT, VEX crosses the magnetopause (at an altitude of about 1226 km) and enters the magnetic barrier (purple bar), which may be described as the 'transition layer' [*Coates et al.*, 2008]. In the magnetic barrier, the electron distribution broadens, spanning 3 eV to 70 eV which shows a mixture of higher energy sheath-like (∼11 eV to 70 eV) and lower energy ionospheric (3 eV to ∼11 eV) plasma. The lower boundary of the magnetic barrier is not particularly obvious here; the electron distribution remains broad without an obvious peak until 01:46 UT (altitude of 768 km).

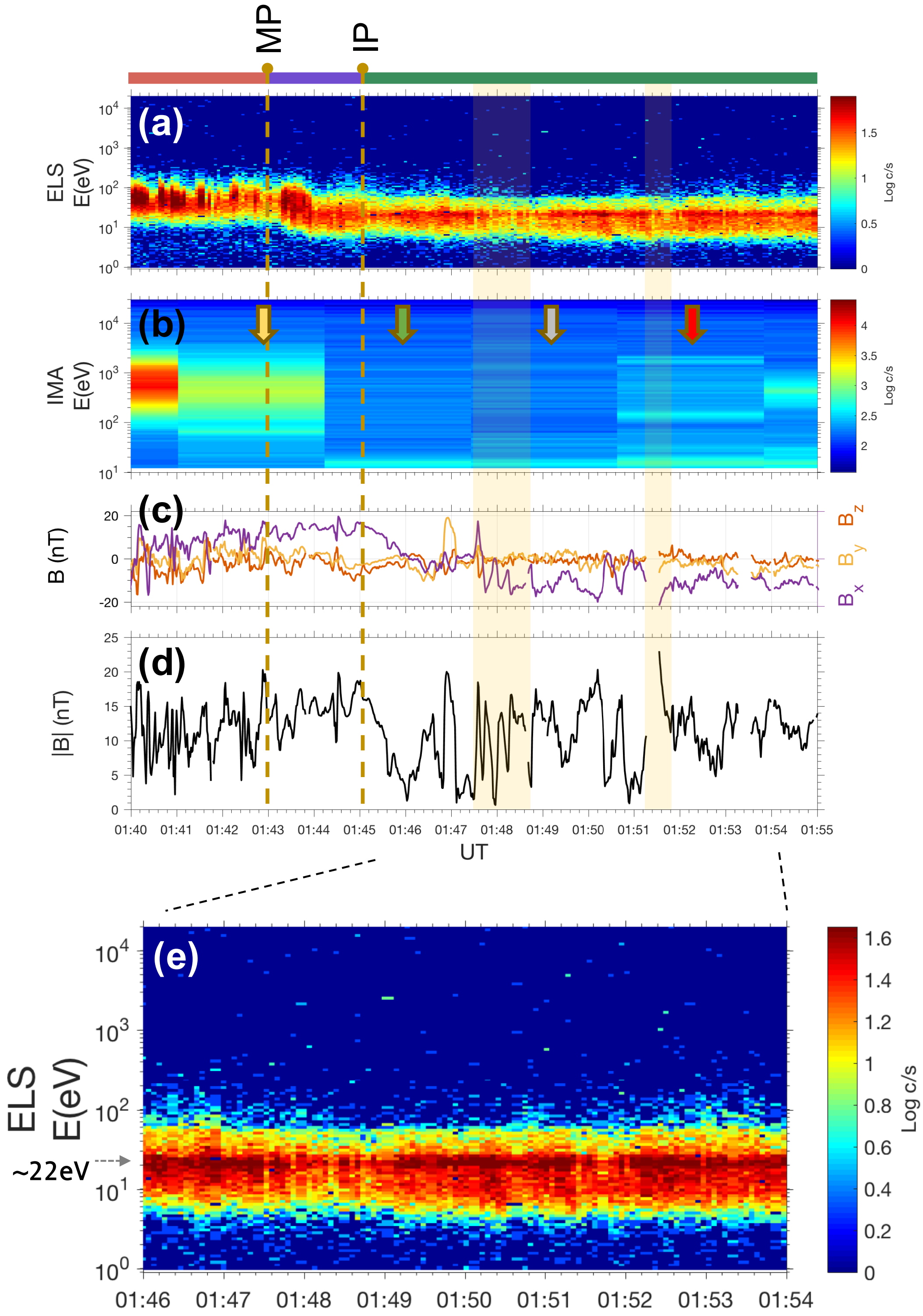

Figure 4.2: (a) The electron energy-time spectrogram of count rate, (b) the ion energy-time spectrogram of count rate, (c) magnetic field components in X_{VSO}, Y_{VSO} and Z_{VSO} directions, and (d) magnitude of the magnetic field from 01:40 to 01:55 UT. The multiple pulse-like photoelectron dropouts intervals are shaded in yellow. (d) A section of the electron energy-time spectrogram from 01:46 to 01:54 UT which clearly shows multiple pulse-like dropouts in the electron count rate.

Figure 4.2 shows the (a) the electron energy-time spectrogram of count rate, (b) ion energy-time spectrogram of count rate, (c) components of the magnetic field in VSO coordinates and (d) magnitude of the 1Hz magnetic field from 01:40 to 01:55 UT that focuses the inbound magnetic barrier and ionosphere in greater details. Figure 4.2(e) shows a section of the electron energy-time spectrogram of count rate from 01:46 to 01:54 UT which shows multiple pulse-like dropouts in the electron count rate.

The inbound ionopause was crossed at around 01:46 UT at an altitude of about 768 km. The ionosphere region (green bar) is identified by the observation of ionospheric photoelectron population which has electron flux intensity peaking ∼21-22 eV. This is also clearly denoted by the grey arrow on the Y_{VSO} axis in Figure 4.2(e) which shows the ionosphere region in greater detail. These photoelectron population are mainly due to the photo-ionization of oxygen by solar HeII 30.4 nm photons [*Coates et al.*, 2008]. They typically have a unique signature of flux intensity peaking at 21-24 eV and at 27 eV [*Coates et al.*, 2008; *Cui et al.*, 2011]. In addition, the mean average magnetic field magnitude in the ionosphere is ∼9.16 nT, making this a good example of a VEX pass through an unmagnetised ionosphere (upper limit of unmagnetised ionosphere is ∼15 nT [*Angsmann et al.*, 2011]). There are intervals of pulse-like missing photoelectron population in the ionosphere region which are shaded in yellow in Figure 4.2. These will be termed as "photoelectron dropout" events throughout this work. VEX was in the ionosphere region through the periapsis of 303 km and then crossed the outbound ionopause at around 01:59 UT (at an altitude of about 845 km). The outbound planetary pass can be characterised similarly to the inbound pass but in a reversed order. A mixture of sheath-like and ionospheric plasma populations were detected in the outbound magnetic barrier. The spacecraft then crossed the magnetopause at 02:04 UT into the outbound magnetosheath and eventually crossed the bow shock again at 02:30 UT.

Figure 4.1(e), (f) and (g) show the energy-mass channel plots of the ion populations in the unshocked solar wind, magnetosheath and ionosphere regions, which are also indicated with the yellow, green and grey coloured arrows in Figure 4.1(c). The yellow circled populations are due to noise/H^+ contamination. The six white coloured lines are the mass-position lines which correspond to mass-to-charge ratio m/q of (starting from the left) 32, 16, 8, 4, 2 and 1 (amu/C). Ions observed around these lines indicate the presence of O_2^+, O^+, O^{++}, He^+, He^{++} and H^+ respectively. In this work, the ion populations with $m/q \geq 8$ are considered the heavy ions. Moreover, the IMA ion data is also used to characterise the different planetary regions. For instance, the typical high and narrow He^{++} and H^+ energy with solar wind origins can be reflected in Figure 4.1(e) which is sampled when VEX was in the unshocked solar wind region indicated by the yellow arrow in Figure 4.1(c). Similarly, the heated and broaden ion (H^+) energy distribution in the magnetosheath region can be reflected in Figure 4.1(f). Finally, the cold and low energy heavy O ions and protons (H^+) originating from the Venusian atmosphere can be seen in the ionosphere region in Figure 4.1(g).

Throughout this work, the first observation of photoelectrons during an orbit is identified as the inbound ionopause and the last observation of photoelectron population is identified as the outbound ionopause. The ionosphere is the region within the inbound and outbound ionopause.

4.3 Analysis of the boundary wave

From Figure 4.2(d), it is clearly seen that the magnetic field drops almost to 0 nT in the ionosphere region on a number of occasions, e.g. 01:46, 01:47, 01:48 and 01:51 UT. The high peaks of these magnetic field fluctuations around 15 to 20 nT are comparable to the field magnitude in the magnetic barrier region. Furthermore, these magnetic field fluctuations also correspond directly to the intervals of pulse-like photoelectron dropouts. These intervals are clearly shaded in yellow in Figure 4.2.

On the other hand, Figure 4.3 shows the four energy-mass channel plots of the ion populations in different regions indicated with the yellow, green, grey and red coloured arrows in Figure 4.2(b). The heavy ions (with m/q similar to and greater than 8) and the low energy protons originate from the upper atmosphere as well as the ionosphere. They are identified by black circles. The high energy protons which are from the shocked solar wind are identified with red circles.

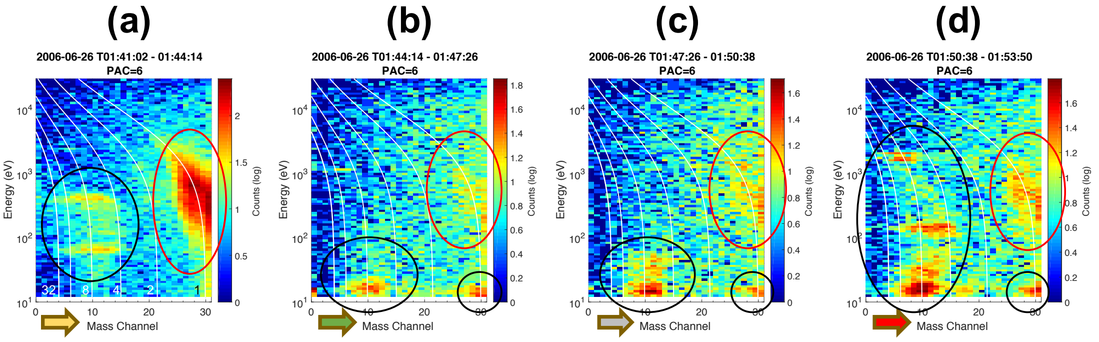

Figure 4.3: (a)-(d): the energy-mass channel plots of the ion populations in different regions indicated with the yellow, green, grey and red coloured arrows in Figure 4.2(b). The ion populations circled by black lines are ionospheric and those circled by red lines are from the solar wind.

These high energy proton populations (circled in red) are observable during all four intervals presented. They are expected in Figure 4.3(a) and (b) as VEX-IMA was sampling the magnetic barrier region. However, these high energy proton populations are also clearly observed in Figure 4.3(c) and (d) which is not expected in the ionosphere. Note that the heavy ion populations observed in Figure 4.3(a) are normally not expected as well. However, these atmospheric ions could be attributed to the "atmospheric bubbles" which will be discussed further in later sections.

In the ionosphere, it would be expected that the ionospheric plasma population to be constantly observed and the solar wind plasma should be absent. So, the occurrence of the photoelectron dropouts and the observations of proton populations with shocked solar wind origins in the ionosphere imply that: while VEX was in the ionosphere, there were periods when VEX detected ion and electron populations as well as magnetic field magnitude similar to those in the magnetic barrier region. This can be due to a few possible scenario: 1. VEX travelled into and out of the ionosphere numerous times in a single VEX pass, 2. VEX crossed into magnetic flux ropes with magnetic barrier origins and 3. VEX travelled into patches of magnetised and unmagnetised plasma. However, the decay of the magnetic field in the ionosphere is on a time scale of minutes to several hours [*Luhmann et al.*, 1984]. As a comparison, the magnetic field fluctuations that correspond to the photoelectron dropouts are rather instantaneous, on the time scale of seconds. Hence, the last scenario of VEX travelled through patches of magnetised

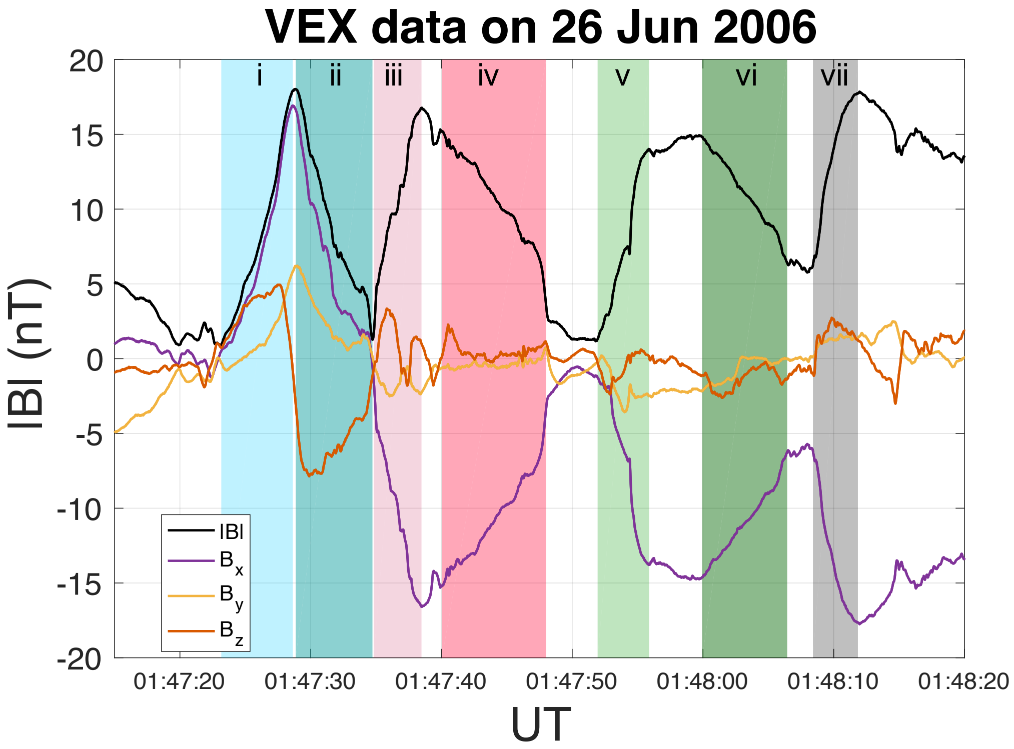

Figure 4.4: A section of the Venus Express data on the 26 June 2006 which shows seven consecutive oscillations (dip-to-peak and peak-to-dip) of the magnetic field. The black plot represents the field magnitude, the purple, yellow and orange represent the field components in X_{VSO}, Y_{VSO} and Z_{VSO} directions respectively. Each dip-to-peak-to-dip is also shaded in lighter and darker shade of colours for ease of identification.

and unmagnetised regions of the ionosphere consecutively can be ruled out.

Crossings of both the flux ropes and ionopause can be characterised by tangential discontinuity. Hence, the first two scenarios indicate that if VEX was to travel from the magnetic barrier to the ionosphere region or vice versa, or to travel into and out of a magnetic flux rope with magnetic barrier origins, boundary of tangential discontinuity would have been crossed. Multiple crossings of the ionopause/flux rope in a single VEX pass indicate a boundary wave. Therefore, MV analysis is implemented to find out if the ionopause was crossed over the intervals when photoelectron dropouts are observed. In the case that they are ionopause crossings, MV analysis will be utilised to find their respective normal directions.

Figure 4.4 shows the magnetic field data (in X_{VSO}, Y_{VSO} and Z_{VSO} direction) over a section of these consecutive oscillations region (01:47:15 to 01:48:20 UT) which correspond to the first yellow-shaded region in Figure 4.2. The second yellow-shaded is associated with a gap in magnetic field and which will be omitted from the following analysis. The field magnitude shows three distinct oscillations between sheath and ionospheric levels, with the magnetic field data oscillating from around 2 nT to 18 nT. These dip-to-peak and peak-to-dip magnetic field correspond to the pulse-like dropouts in the electron energy-time spectrogram, visible from Figure 4.2(e). Each of the dip-to-peak and peak-to-dip are shaded in different colours and are labelled in lower case Roman numerals for ease of identification in Figure 4.4.

Table 4.1 shows the components of the minimum variance directions in the X_{VSO}, Y_{VSO} and Z_{VSO} directions, intermediate-to-minimum eigenvalues ratio ($\lambda_{int}/\lambda_{min}$), the ratio of average magnetic field component along the minimum variance direction (B_n) to the larger field magnitudes on either side of the discontinuity ($|B_n|/|B|$), the ratio of the change of the field magnitude to the field magnitude ($|\triangle B|/|B|$), the angle between $|B_n|$ and $|B|$, $\theta_{\ B_n\text{-}B}$, the number of data points during the intervals analysed as well as the angle between the spacecraft trajectory and the minimum variance directions, $\theta_{\ VEX,MV}$.

The minimum variance directions of all seven intervals for the periods corresponding to successive dip-to-peak and peak-to-dip magnetic oscillations are generally well-defined. In particular, the intermediate-to-minimum eigenvalues (λ_2/λ_1) of all the minimum variance directions are > 4, apart from Region v (01:47:51 to 01:47:55 UT) which the minimum variance direction is slightly less well-defined with λ_2/λ_1 of 3.57. This may be affected by the magnetic field intermediary at 01:47:54 UT (centre of Region v in Figure 4.4).

It is noticeable from Figure 4.4 that the main changes of the field measurement in this period are mostly in the X_{VSO} direction. Apart from Regions i and ii, the components along Y_{VSO} and Z_{VSO} are relatively close to zero ($\sim \pm 3$ nT). The mean average total magnetic field dips in this duration are also close to zero nT ($\sim$ 2 nT) which may indicate VEX was travelling in the ionosphere region where the plasma is almost unmagnetised. Additionally, all the $|B_n|/|B| < 0.25$ (mean value of 0.09) and $|\triangle B|/|B| > 0.56$ (mean value of 0.7). These are well within the criteria for tangential

Table 4.1: A summary of the results of the Minimum Variance Analysis on Venus Express data on 26 June 2006 for all the photoelectron dropout intervals shown in Figure 4.4.

Time (UT)		MV Direction								
From	To	X	Y	Z	$\lambda_{int}/\lambda_{min}$	$\lvert B_n\rvert/\lvert B\rvert$	$\lvert\triangle B\rvert/\lvert B\rvert$	$\theta_{B_n,B}$ (deg)	Data Point	$\theta_{\;VEX,MV}$
‘01:47:23’	‘01:47:28’	0.331	-0.920	-0.209	68.97	0.06	0.89	86.7	176	163.9
‘01:47:28’	‘01:47:34’	0.365	-0.923	0.122	20.29	0.07	0.64	86.1	189	160.2
‘01:47:34’	‘01:47:38’	-0.061	0.919	0.390	144.86	0.04	0.67	87.5	118	19.0
‘01:47:40’	‘01:47:48’	0.076	-0.996	0.039	7.82	0.04	0.65	87.7	255	173.9
‘01:47:51’	‘01:47:55’	0.191	-0.047	0.981	3.57	0.25	0.92	76.1	126	90.5
‘01:47:59’	‘01:48:06’	0.173	-0.862	0.476	4.01	0.17	0.56	80.1	208	148.2
‘01:48:08’	‘01:48:11’	0.049	0.976	-0.212	31.70	0.01	0.60	89.3	111	17.0

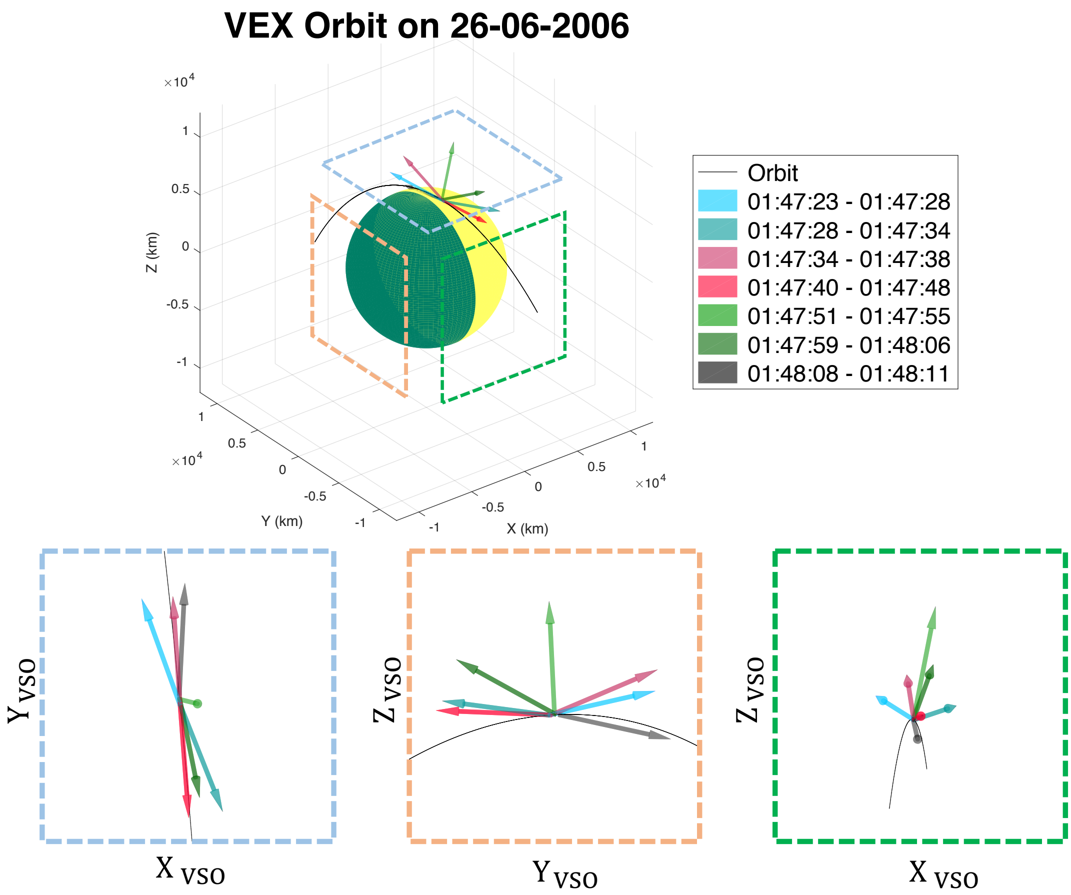

Figure 4.5: Three-dimensional views of minimum variance directions of all the seven “peak-to-dip” and “dip-to-peak” intervals on 26 June 2006 . The intervals ‘01:47:22 - 01:47:28’,‘01:47:34 - 01:47:38’, ‘01:47:51 - 01:47:55’, ‘01:48:08 - 01:48:11’, ‘01:47:28 - 01:47:34’, ‘01:47:40 - 01:47:48’ and ‘01:47:59 - 01:48:06’ are colour-labelled with respect to their minimum variance directions. The colour-dotted frames are 2D views of the trajectory where blue is X-Y $_{VSO}$ plane, pink is Y-Z $_{VSO}$ plane and green is X-Z $_{VSO}$ plane.

discontinuity mentioned earlier in Chapter 3; $|B_n|/|B| < 4$ and $|\triangle B|/|B| \geq 0.2$. The tendency of the angle between $|B_n|$ and $|B|$ to be 90° (all $\theta_{B_n,B} >$ 76.1°, mean value of 84.8°) further indicates that this is a tangential discontinuity; a typical characteristic of the Venusian ionopause [*Wolff et al.*, 1980].

All the seven minimum variance directions are plotted against the orbit in Figure 4.5; both the figure and the table are colour-coded. If the dayside ionopause is assumed to exist as a smooth quasi-spherical boundary separating the atmospheric plasma from the shocked solar wind, then the boundary normal directions at the locations of the

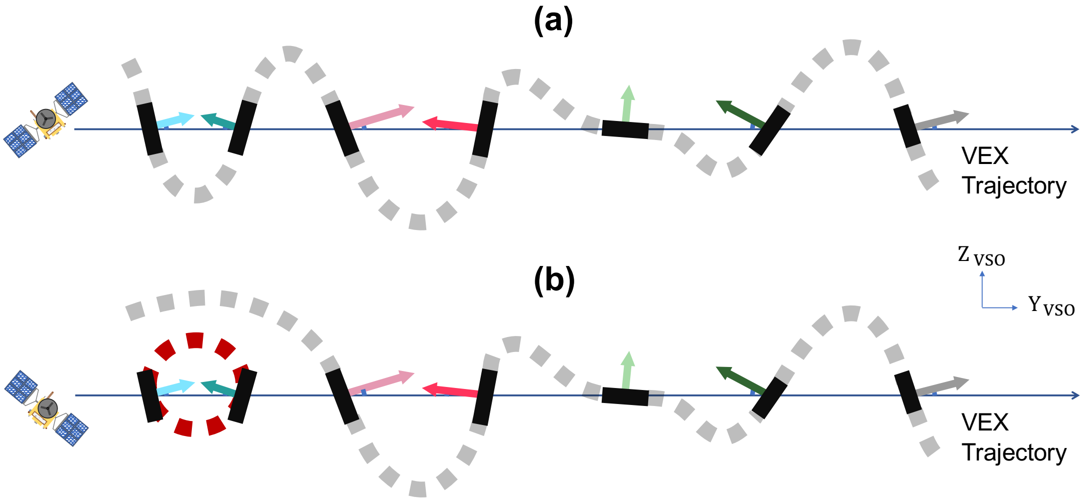

Figure 4.6: (a) A possible illustration of the boundary wave observed from 01:47:22 to 01:48:12 UT. The normal directions of the boundaries are represented by the coloured arrows. The arrows are colour-coded according to Table 4.1. The black lines represent the instantaneous boundaries which VEX crosses. The grey dotted line completed the illustrative shapes of the boundaries. The blue straight arrow represents the trajectory of VEX. (b) A similar illustration of the boundary wave, but also including an isolated flux rope represented as a red dotted line.

crossings should lie radially outward from the centre of Venus. However, this scenario is not reflected from the results shown in Figure 4.5.

As the ionopause is crossed mainly around the northern polar region of Venus on this VEX pass, the minimum variance directions of smooth quasi-spherical boundary crossings should have dominant components along the Z_{VSO} axis. Instead, Figure 4.5 shows that the minimum variance directions of the boundary crossings lie mainly along the Y_{VSO} axis.

4.3.1 Possible appearance of the ionopause

In this section, the data analysis of 26 June 2006 so far has shown that, when VEX was in the ionosphere, (1) there are intervals of photoelectron dropouts even though they are expected to be observed continuously throughout the ionosphere, (2) a mixture of ionospheric and solar wind ion populations are observed, (3) consecutive field oscillations from high field (sheath-like) to low field (ionospheric) are experienced, (4) ionospheric boundary is crossed multiple times throughout these intervals of photoelectron dropouts, and (5) the normal directions of the boundary crossings mainly lie along the Y_{VSO} axis. These results suggest that on 26 June 2006, the ionopause where VEX crossed repeatedly from the ionosphere into the magnetic barrier (and vice versa), is not smooth but exists in a wavelike appearance propagating along the Y_{VSO} axis. This scenario is interpreted in an illustrative diagram in Figure 4.6(a).

θ_{VEX_MV}, the angle between the trajectory of VEX and the minimum variance directions from each of the dip-to-peak and peak-to-dip transition are calculated and shown in Table 4.1. All seven angles with respect to the VEX trajectory (plotted as a blue straight horizontal arrow) are shown in Figure 4.6(a). The seven arrows, which are colour-coded with their respective intervals in Table 4.1, represent the minimum variance direction of each of the seven boundary crossings. The bold grey dashed lines, which form a perpendicular plane to the minimum variance directions, represent the instantaneous boundaries crossed by VEX. An illustrative shape of the potential boundary is traced with the grey dotted line. The observed changes in angles between the VEX trajectory and the boundary normals indicates the existence of a boundary wave, e.g. Figure 4.6(a). Even though the angles θ_{VEX_MV} were taken into consideration when plotting this figure, the shape and structure should only serve as an illustrative example.

4.4 Analysis of a flux rope

While most of the magnetic wave trains from the previous section (01:47:22 to 01:48:12 UT in Figure 4.4) show properties of a two-dimensional planar magnetic structure, the first dip-to-peak-to-dip from 01:47:23 to 01:47:34 UT (Region i and ii) shows a three-dimensional magnetic structure that has a close resemblance to those of a flux rope, i.e. Figure 2.5. Figure 4.7(a) illustrates the passing of VEX through the centre of a flux rope and Figure 4.7(b) shows how the corresponding magnetic field may change crossing the flux rope in the minimum, intermediate and maximum variance directional frames. Regardless of how a flux rope is crossed, the changes of the magnetic field in the variance frames should be consistent as long as the flux rope is crossed through its

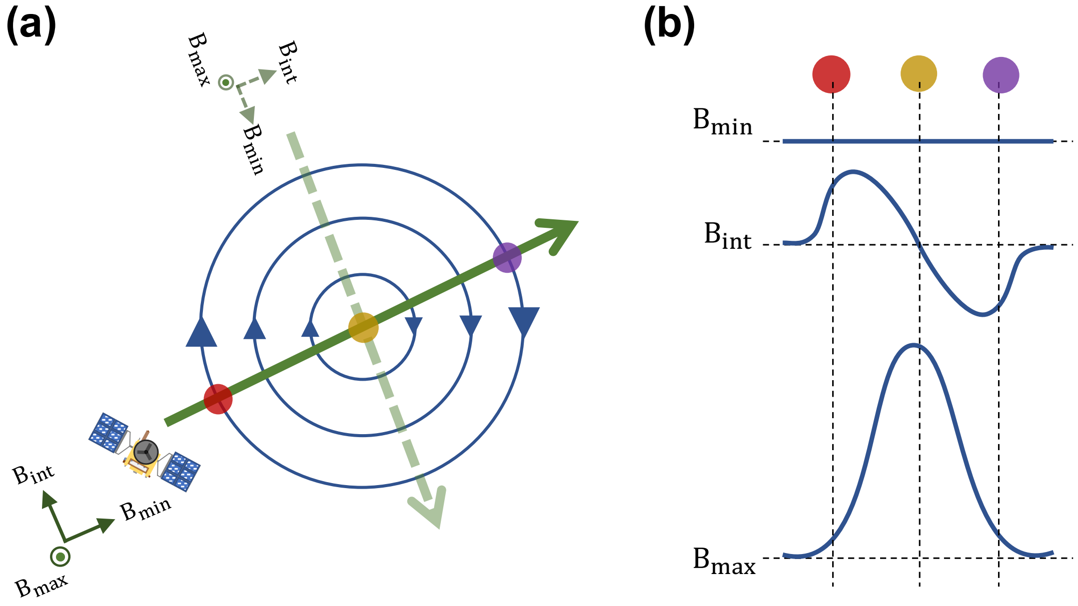

Figure 4.7: (a) An illustration of a VEX passing through the centre of a flux rope. (b) Expected changes of the magnetic field components in the minimum, intermediate and maximum variance coordinates. Green arrow represents the trajectory of VEX. The red, yellow and purple-coloured dots correspond to different spacecraft locations in a flux rope.

centre as illustrated in Figure 4.7.

The flux rope on this VEX pass was observed at an altitude of 574 km and SZA of 87°. The minimum B_{min}, intermediate B_{int} and maximum B_{max} variance components of its magnetic field are shown in Figure 4.8. From Figure 4.8, the magnetic field strength is observed to be the lowest ($\sim$ 1nT) at the boundaries of the magnetic structure (corresponds to the begin and the end of the field magnitude plot). The magnetic field strength increases as the structure is crossed gradually, peaking in the maximum variance direction ($\sim$ 18nT) before it decreases towards the exiting boundary. In addition, it can be observed in Figure 4.8 that when the magnetic field in the maximum variance direction B_{max}, is at its peak strength, the intermediate and minimum variance components B_{int} and B_{min} reach minimum (≈ 0 nT). This suggests that VEX crosses a magnetic structure with weak field strength at the boundaries and strong axial field in its centre; e.g. a flux rope. Note that unless the spacecraft passes through the exact centre of the flux rope, there will be a finite azimuthal field component (or B_{min}) perpendicular to its axis. The MV analysis of the flux rope presented here suggests that

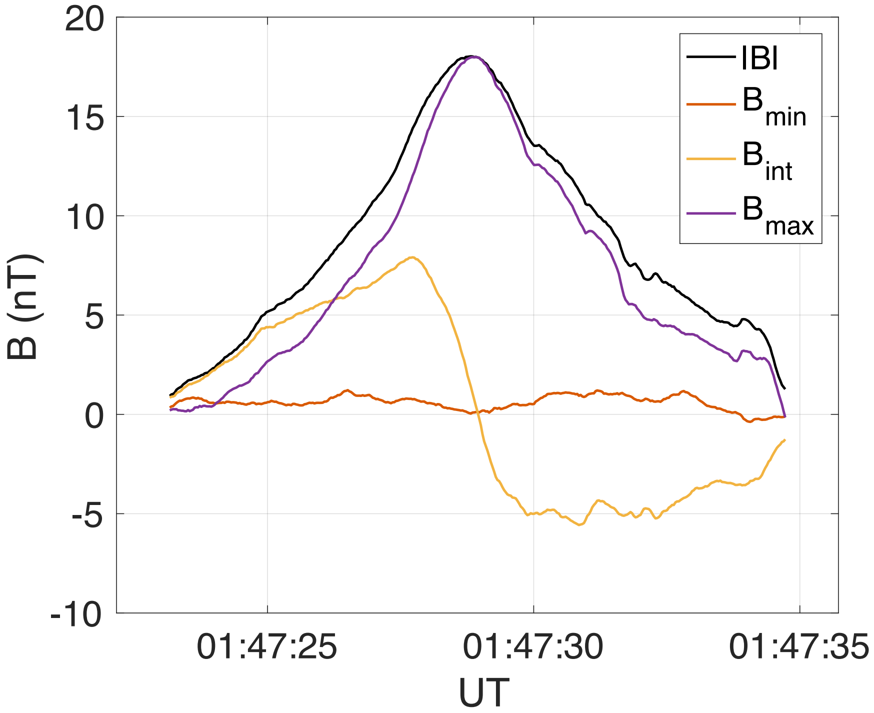

Figure 4.8: The magnetic field (in the minimum, intermediate, and maximum variance coordinates) of the flux rope observed from 01:47:23 UT to 01:47:34 UT.

VEX crossed very close to the centre of the flux rope. This is reflected from the very low but non-zero magnitude of B_{min}. The results presented in Figure 4.8 are consistent to the illustration shown in Figure 4.7.

To find out if these changes of direction are three-dimensional, further analysis is conducted. Figure 2.5 shows the magnetic structure of a flux rope (adapted from [*Russell and Elphic*, 1979]). The red, yellow and purple-coloured arrows (labelled B_{in}, B_{axis} and B_{out}) that represent the instantaneous magnetic field directions which VEX crosses at the inbound boundary, central axis and outbound boundary. If the VEX trajectory is assumed to cross the flux rope as illustrated in Figure 2.5, and if the direction of the peak magnetic field is assumed in the direction of the axis (B_{axis}) of the flux rope, the angle between the field direction at the inbound crossing of the boundary (B_{in}) and the axis (B_{axis}) from the analysis is found to be 77°. Similarly, the angle between the field direction at the outbound crossing of the boundary (B_{out}) and axis (B_{axis}) is 54°. The existence of these rotations between B_{in}, B_{axis} and B_{out} shows the field rotation is three dimensional as illustrated in Figure 2.5, implying that the structure

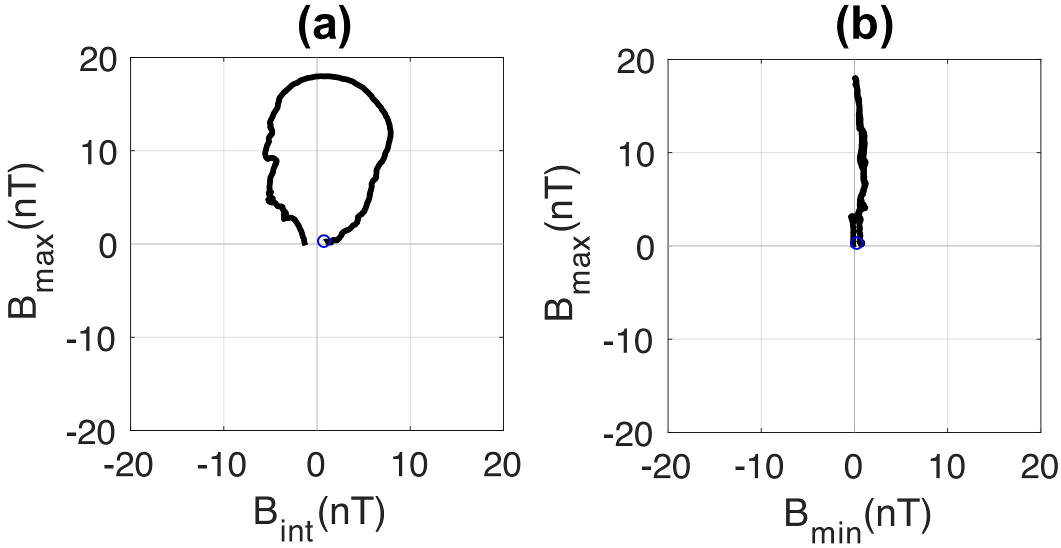

Figure 4.9: Hodogram of the field variation in (a) B_{max} to B_{int} and (b) B_{max} to B_{min} plane from 01:47:23 to 01:47:34 UT.

which VEX traversed through is not just a two-dimensional planar magnetic structure. All the above observations are consistent with the signature characteristics of a flux rope.

Furthermore, while the minimum variance component B_{min} (orange) is close to 0 nT throughout the interval, it is visible from Figure 4.8 that the direction of the intermediate variance component B_{int} (yellow) flips 180° quickly (in just under 2 seconds) as the maximum variance component B_{max} (purple) reaches its maxima. This observation is consistent with the typical characteristic of the structure of a flux rope. If B_{int} represents B_{in} in Figure 2.5, B_{int} decreases as VEX passes through the flux rope and it will reach minima (zero in our case) when VEX passes through/close to the centre of the flux rope (as the main magnetic field component will be along the axis). Similarly, as VEX leaves the centre of the flux rope, B_{int} increases but in the opposite direction and eventually reaches B_{out} when VEX traversed through the outbound boundary; i.e. the B_{in} and B_{out} are 180° opposite in direction.

The hodogram of the variance components is shown in Figure 4.9(a) and 4.9(b). The start of the hodogram plot is marked with a blue circle. The minimum variance direction of this magnetic structure is very well-defined with eigenvalues ratio of $\lambda_2/\lambda_1 > 169$. It can be seen that the magnetic field direction rotates by 180° as VEX traverses through the magnetic structure which is consistent with our observation from Figure 4.8. Another key identifier that this magnetic structure is in fact a flux rope and not some planar magnetic structures, is the "potato chip" shape hodogram [*Russell*, 1990] as shown in Figure 4.9(b) that indicates the magnetic structure is axially 'twisted'. In contrast to this "potato chip" shape, a vertical line of B_{max}/B_{min} would have indicated that the magnetic structure is "untwisted"; i.e. not a flux rope.

In comparison to Figure 4.6(a), the observation of a flux rope and how it may exist within the boundary wave is illustrated in Figure 4.6(b). Both of the plots only serve as an illustration. Due to the limitations of Venus Express instrumentation and without further analysis, the exact physical structure of the flux rope and the boundary wave cannot be determined with certainty.

4.5 Discussion

This chapter has presented the results of the observation of boundary waves and a flux rope on the 26 June 2006 using the VEX magnetic field and plasma measurement data.

4.5.1 Altitude of the ionopause

Even though the plasma data measured from VEX as well as the MV parameters from the data analysis are consistent with the signatures of the Venusian ionopause, the altitude at which the boundary wave and flux rope are observed on 26 June 2006, is much higher than the nominal altitude of the ionopause during solar minimum (572 km compared to the nominal 250 km [*Zhang et al.*, 2008a]). Furthermore, during solar minimum, the ionosphere is expected to be magnetised most of the time [*Zhang et al.*, 2007], a state which often contains large-scale magnetic field structures. Since such field structures may suppress the formation and the observation of flux ropes, flux ropes are infrequently observed even though they are observed in more than 70% of the orbits of PVO (during solar maximum) [*Elphic and Russell*, 1983].

Although it may not be a common, the terminator ionopause has previously been observed at much higher altitudes (> 700 km) during solar minimum [*Zhang et al.*, 2008a; *Coates et al.*, 2008; *Futaana et al.*, 2008; *Angsmann et al.*, 2011] and has been observed as high as 900 km during solar maximum [*Zhang et al.*, 2008a]. The Venus ionosphere can also sometimes be observed field-free at solar minimum (an unmagnetised ionosphere was observed in 39 out of 225 VEX orbits from 24 April to 30 December in 2006 according to [*Wei et al.*, 2010]) and resemble the environment at solar maximum; e.g. on 26 June 2006 when the magnetic field strength $|B|$ of the ionosphere is ≈ 0 nT. The preliminary survey of VEX in 2006 by [*Zhang et al.*, 2008a] shows that about 5% of the orbits are unmagnetised, of which are all under extreme solar conditions, e.g. Interplanetary Coronal Mass Ejection (ICME) events [*Futaana et al.*, 2008] and IMF alignment with solar wind flow [*Zhang et al.*, 2009]. Note that the VEX pass on 26 June 2006 presented in this chapter does not fall into either mentioned cases. Further analysis of the VEX magnetic field data in a period of ± 15 days of this date shows a mixture of magnetised and unmagnetised ionosphere, with a higher occurrence of the former.

Although the periapsis of VEX is consistently around 250-350 km and because the nominal altitude of the Venusian ionopause is 250 km [*Zhang et al.*, 2008a] during solar minimum, VEX normally only crosses the ionopause for a very short time (or not at all) during solar minimum. This could also explain why physical boundary waves are rarely observed during solar minimum. In addition, significant disturbance of the ionopause boundary due to the boundary waves may also result in crossings being observed at higher than expected altitudes.

4.5.2 Kelvin-Helmholtz instability and the scarcity of the observations

The flux rope and boundary waves are observed close to the terminator (SZA of 86.8°). The strong velocity shear in the terminator region, is a principal seed excitation for the development of the KHI [*Terada et al.*, 2002; *Amerstorfer et al.*, 2007; *Wolff et al.*, 1980; *Elphic and Ershkovich*, 1984; *Pope et al.*, 2009; *Pérez-de Tejada et al.*, 1977]. As the boundary wave grows and develops from the linear to non-linear regime, vortices can form. These vortices can roll up and eventually break up forming bubbles of ionospheric plasma. These detached ionospheric bubbles are eventually convected downstream by the magnetosheath flow. This process is subsequently responsible for atmospheric plasma loss of Venus [*Lammer et al.*, 2006; *Elphic and Ershkovich*, 1984; *Wolff et al.*, 1980; *Brace et al.*, 1982; *Russell et al.*, 1979; *Russell and Elphic*, 1979; *Terada et al.*, 2002]. Coincidently on 26 June 2006, ionospheric heavy ion populations are observed out of the ionosphere in the magnetic barrier region as shown in Figure 4.3(a). These are likely due to the detached atmospheric bubbles from the boundary wave phenomenon observed on the same day.

In addition, over the period where the rippling ionopause boundary is observed (01:47:22 to 01:48:12 UT), the approximately perpendicular orientation between the magnetic field direction in the magnetic barrier region (mainly along X_{VSO} direction) and the wave normal of the ionopause boundary (which are represented by the minimum variance directions mainly along Y_{VSO} direction) favours the excitation of KHI [*Wolff et al.*, 1980].

Flux ropes can be produced in the subsolar region by the mass loading process and may be transported into the nightside through the terminator region. Although the periapsis of VEX was maintained at around 250 km (nominal ionopause altitude), the population of flux ropes has been shown to be greatest at lower altitudes (highest population is around 165 km according to [*Russell and Elphic*, 1979; *Elphic and Russell*, 1983]), therefore VEX observations of flux ropes tend to be infrequent. On the other hand, atmospheric bubbles and flux ropes are both produced in the terminator region [*Brace et al.*, 1982] and can co-exist in theory. However, by the time the atmospheric bubbles are fully developed, they have already been transported downstream into the nightside. This can explain the scarcity of the observations of the atmospheric bubbles in the dayside. In addition, there are only an estimated 12 plasma clouds in the cloud zone at any time [*Brace et al.*, 1982]. More in-depth analysis on the production of flux ropes will be discussed in Chapter 5.

4.5.3 Shape and sizes

The normal directions of the inbound and outbound boundary crossings of the flux rope are quasi-parallel which is observable from Table 4.1. Based on this quasi-parallel orientation, as well as the very low B_{min} (observable from Figure 4.8), the flux rope can be presumed to be crossed by the spacecraft through its centre. Apart from the interval '01:47:51' to'01:47:55' where its minimum variance direction is predominantly along the Z_{VSO} axis (which could be due to the magnetic intermediary as mentioned previously), the $\theta\ _{VEX,MV}$ of the rest of the intervals $\approx 0°/180°$ indicates that VEX was travelling quasi-perpendicular into the boundary wave and flux rope, i.e. as illustrated in Figure 4.6.

Based on the above assumptions, as well as a stationary boundary wave and flux rope, the mean average width of each oscillation and the flux rope are $\sim$ 133 km and $\sim$ 113 km respectively. This is estimated from the mean average speed of VEX ($\sim$9.5 km s^{-1}) and time spent during the crossing. If the flux rope is assumed to be moving at the local Alfven speed, $\pm$1 km s^{-1} [*Elphic and Russell*, 1983] or less (relative to VEX trajectory), then the width of the flux rope would be $\sim$101 or $\sim$125 km.

The observations discussed in this paper suggest the structure has the characteristics of a flux rope. However, the estimated width is significantly greater than the upper boundary of their estimated diameter (16 km in the terminator region) suggested by *Russell* [1990]. One explanation for this is that the flux rope is newly created as a result of turbulent boundary and it is then observed just underneath the ionopause after VEX crosses the centre line of the draping (this is discussed further in Section 4.5.4). Flux ropes become more twisted as they travel deeper into the ionosphere, resulting in a decrease in their width. This can be attributed to the Helical Kink Instability [*Russell*, 1990]. Furthermore, based on the plasma parameters obtained from PVO, *Wolff et al.* [1980] shows that the wavelengths of the KHI can range from around 50 km to 150 km. Since the flux rope is observed very close to the ionopause boundary and the estimated width of the flux rope of around 113 km is in the range of the KHI wavelength in [*Wolff et al.*, 1980], the estimated width is within the possible limit.

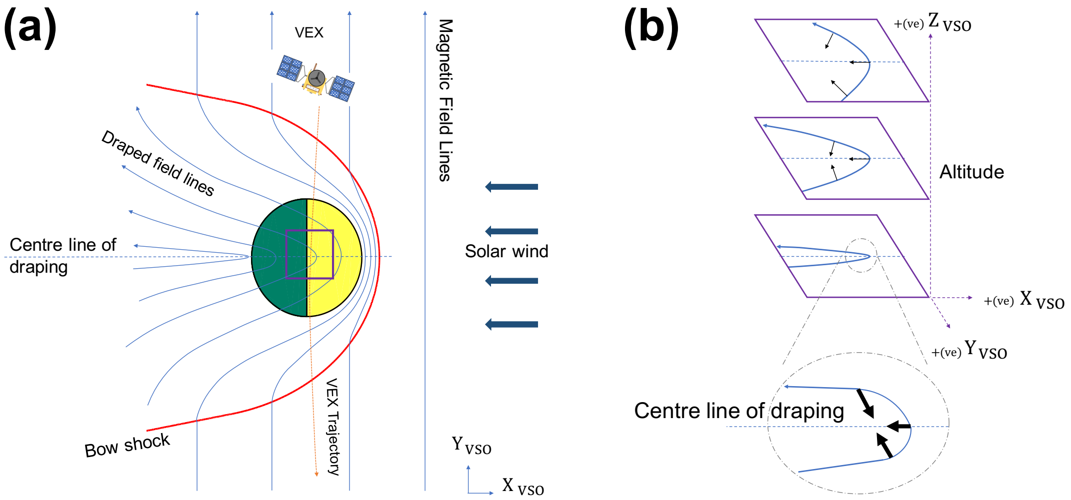

Figure 4.10: (a) Illustration of field draping around Venus in the X-Y $_{VSO}$ plane. The magnetic field lines are represented by the blue arrows. As they are swept towards the planet, they start to drape around the planet with the field lines extending in the -X_{VSO} direction. (b) Illustrates the change in field line draping as a function of altitude for the area in the purple-coloured square box. The black arrows represent the normals to the field line directions as they drape around the planet. As the altitude decreases the directions of the field lines become more anti-parallel along the flanks of the draping.

Since only one flux rope is observed in this particular study, in comparison to [*Elphic and Russell*, 1983] which includes statistical variations, our estimation of the width depends on how the spacecraft encounters the flux rope. For example, different width calculations will result if VEX traverses through the exact centre of the axis or just off centre. In addition, flux ropes can diffuse within the ionosphere and exist in an elongated shape [*Wolff et al.*, 1980]. This could create marginal variations in the calculation.

Furthermore, the magnetic field lines are draped as illustrated in Figure 4.10. If the centre line of draping is taken to be the origin of the Y_{VSO} axis, the field lines on the $+Y_{VSO}$ and -Y_{VSO} will tend to travel in the direction towards the origin as a result of field draping as seen in Figure 4.10(b). Since the boundary wave phenomenon is observed in the $+Y_{VSO}$ location, the observed wave is expected to be propagating in the -Y_{VSO} direction towards the origin. Based on this, the estimated width of each of the oscillations is ~147 km (considering a relative Alfven speed of ±1 km s^{-1} [*Elphic and Russell*, 1983]). Due to the practical limitations of VEX, configuration of the complete physical structure of the surface wave is not possible.

As discussed in the previous section, to check the consistency of MV analysis results, each of the magnetic field dip-to-peak and peak-to-dip over the interval (01:47:22 to 01:48:12 UT) was divided into several segments and further analysed using MV analysis. This has revealed that there are distinct differences between the minimum variance parameters of some of the segments and the main transition. The results indicated that while the individual segments of the main transition showed consistent variance directions, the results from segments around the peaks or dips which correspond to magnetic barrier and ionosphere respectively (i.e. the start and end of the individual boundary transitions) are quite different. As seen from Figure 4.4, if the thickness of the ionopause boundary is represented by the width of the colour-shaded regions, then the observed different widths suggests that there is a variation in the ionopause boundary thickness.

The variations of the thickness of ionopause boundary is not illustrated in Figure 4.6. Furthermore, there is negligible non colour-shaded transition between Region i and ii, which may imply that VEX was in neither the magnetic barrier nor the ionosphere, further agreeing with our findings that the first magnetic field oscillation dip-to-peak-to-dip is an isolated flux rope.

4.5.4 Embedded flux rope in the boundary wave

The results from the data analysis suggest that the flux rope is observed just inside the ionopause. This leads to a couple of outstanding questions. Firstly, how do the analysis results of the flux rope differ to the crossings of boundary wave? The hodograms (Figure 4.9) of the flux rope show a smooth 180° field rotation with finite pitch angles with respect to the axis; e.g. the angle between B_{axis} and B_{in} (77°) as well as B_{out} (54°), a characteristic that is unique to flux ropes and commonly not expected from a boundary wave. In contrast, further analysis conducted on the rest of the wave train (attached in Appendix A) shows only planar field rotations (i.e. changes in a plane with negligible pitch angles). However, there is a scenario where the characteristics of a boundary wave could resemble a flux rope. Non-draped field lines can be represented locally as an ellipse with eccentricity of infinity, e.g. Figure 4.10(a). As they progress towards the planet, the field lines start to drape around the planet. For the case of field lines around the northern polar region near the centre line of the draping, the eccentricity tends towards zero with the field lines extending in -X_{VSO} direction. If VEX crosses this point, the eccentricity will be small and result in tightly curved field lines, e.g. Figure 4.10(b). In this case, VEX may observe a non-planar (three-dimensional) field rotation associated with a boundary wave that can be misinterpreted as a flux rope at the first glance. Furthermore, only the first dip-to-peak-to-dip (the flux rope) shows a "potato chip"-shaped hodogram while the rest shows a mixture of randomly and linearly-shaped hodograms, i.e. not a flux rope. Based on the observations of (i) smooth 3-dimensional 180° field rotation as shown in hodogram in Figure 4.9(a), (ii) finite pitch angles between B_{axis} and B_{in} as well as B_{out}, and (iii) a "potato chip"-shaped hodogram as shown in Figure 4.9(b), all of which are expected characteristics of a flux rope. These results then suggest that the first dip-to-peak-to-dip corresponds to a flux rope that is observed in the vicinity of the ionospheric boundary wave.

Secondly, if flux ropes are normally more frequently observed deeper in the ionosphere, why is the flux rope observed so close to the boundary wave? To begin with, the IMF is observed to drape around Venus which is evident from an abrupt change of magnetic field in the B_X direction at around 01:45:30 UT (evident from Figure 4.2(c)). Through the draping of field, B_X changes from $+X_{VSO}$ to -X_{VSO} direction. As VEX was travelling almost along the terminator on this date, if the hemisphere in which before VEX crossed the field draping is regarded as the dawn-hemisphere and the hemisphere in which after VEX crossed the field draping is regarded as the dusk-hemisphere, then the observations of the flux rope as well as the boundary wave were just in the dusk-hemisphere, which is only about two minutes after the centre of the draping was crossed. However, the characteristics of the magnetic field in the flux rope are found to be similar to the magnetic field in the dawn-hemisphere, where in particular the magnetic field in the X_{VSO} direction is positive while the Y_{VSO} and Z_{VSO} directions are close to zero. In contrast, the characteristics of the magnetic field for the rest of the wave train are similar to the magnetic field in the dusk-hemisphere after crossing the draping (i.e. the field in X_{VSO} direction is consistently in the negative direction). Since the signatures of the flux rope are different from the boundary wave in the dusk-hemisphere, the results suggest that the flux rope may have been produced in the dawn-hemisphere and transported to the dusk-hemisphere, hence the flux rope is observed to be relatively close to or embedded in the boundary wave. Based on the similarity in diameter of both the flux rope and the boundary wave widths, the generation of the flux rope in the subsolar region by mass loading process is unlikely in this case.

In comparison to the conventional field draping pattern, *Masunaga et al.* [2011] presented a complicated interplanetary magnetic field configuration around Venus. This was for the case of parallel alignment between the incoming magnetic field lines and the Venus-Sun line and it was associated with the loss of oxygen ions from the atmosphere. This configuration consisted of multiple reversals of the B_X component. One generation mechanism they proposed was the KHI. However, they noted a lack of previous studies showing Kelvin-Helmholtz waves directly at the polar ionopause. In our paper, even though the interplanetary magnetic field lines arrive at an angle of $\sim 30°$ (at the limit of the parallel alignment studied in *Masunaga et al.* [2011]), only one reversal of the B_X component is observed. This suggests a conventional draping pattern for this encounter.

4.6 Summary

High resolution data from IMA, ELS and MAG onboard the Venus Express spacecraft are utilised to observe a rippling Venusian ionopause boundary on 26 June 2006 . Results of MV analysis shows VEX repeatedly crossed the ionopause boundary, which suggests the ionopause is in a wave-like state. Further analysis over the duration where the boundary wave, identified a magnetic flux rope embedded just inside the ionosphere. The different magnetic field component signature of the flux rope and ionopause shows that the flux rope was produced in the dawn-hemisphere and transported into the dusk-hemisphere. Results also suggest that the boundary wave phenomenon is induced by the KHI due to the large velocity shear in the terminator plane, where the rippling ionopause boundary is observed, as well as the perpendicular orientation between the magnetic field in the magnetic barrier and the wave normal of the boundary. The production of the flux rope in the subsolar region and subsequent transportation to the nightside, is ruled out based on the similar diameters and close proximity between the flux rope and the ionopause boundary waves.

A brief inspection over ± 15 days of 26 June 2006 for photoelectron dropout events results in only a single date on 29 June 2006 that shows intervals of photoelectron dropout, which may suggest a similar boundary wave perturbation. Based on a single event reported in this chapter, it is not possible to conclude whether this wavelike appearance of the ionopause is an inherent characteristic or otherwise. In the next chapter, a statistical analysis is conducted to measure the global distributions and properties of the ionospheric boundary wave phenomena.

4.7 Contribution

The majority of the results presented in this chapter are, to date, the only detailed analysis of an ionospheric boundary wave event using VEX data. They are published in Journal of Geophysical Research: Space Physics:

Chong, G.S., Pope, S.A., Zhang, T., Collinson, G.A., Walker, S.N. and Balikhin, M.A., 2017. A study of ionopause perturbation and associated boundary wave formation at Venus. *Journal of Geophysical Research: Space Physics, 122*(4), pp.4284-4298.

Chapter 5

Ionospheric boundary stability: Statistical analysis

5.1 Introduction

Based on a single VEX orbit on 26 June 2006, Chapter 4 presented a detailed analysis of the observation of the ionospheric boundary existing in a wavelike appearance. The boundary wave appears to propagate mainly in the Y_{VSO} direction in the northern polar region of Venus where the ionosphere was perturbed. In addition, a magnetic flux rope has also been identified in the vicinity of the boundary wave. Their close proximity and similarity in sizes suggest that the observed flux rope is a result of turbulent boundary wave. Moreover, the strong shear flow in the terminator region where the boundary wave is observed indicates that the KHI may play a role in the excitation of the boundary wave. However, unlike the expected shear direction which should be along the conventional solar wind bulk flow in the -X_{VSO} direction in the terminator region, the estimated boundary wave propagation direction is mainly along the Y_{VSO} direction.

These observations and indications are only based on a single VEX pass through the ionosphere. In addition, as summarised in Chapter 2, the observational studies of the ionospheric boundary wave are rather limited and only short periods of data (one to two orbits of data) have been utilised. Hence, based on these small sets of data, it is not possible to deduce if this particular observation of boundary wave on the 26 June 2006 is an isolated event or a common characteristic of the ionopause. More data is needed to measure the overall distributions of the boundary wave events and understand the global characteristics of the ionopause.

Hence, it is the aim of this chapter to survey all the available VEX data to assess the overall stability, as well as the dynamics of the Venusian ionopause. To achieve this, the ionopause is classified into 'smooth' and 'rippled' cases using a similar approach implemented in Chapter 4, that was based on the presence of the ionospheric photoelectron population and results from the MV analysis. The boundary normal directions at the locations of the crossings of respective cases are compared and their global characteristics will be measured. In addition, all the flux ropes are identified using a similar approach to Chapter 4 that was based on their "potato chip" shape hodogram. Their global characteristics are also presented in this chapter. Finally, the implications of this wavelike appearance of the ionopause and its role in the Venusian atmospheric evolution are discussed.

5.2 Data selection

Based on the previous observation study on boundary waves on 26 June 2006, ionospheric boundary waves can generally be characterised as the following. Firstly, oscillations of magnetic field which correspond to the intervals of photoelectron dropouts indicate the spacecraft was repeatedly travelling between the ionosphere and magnetic barrier regions. Secondly, MV analysis is implemented over these intervals of photoelectron dropouts to assess if the ionopause is crossed, i.e. tangential discontinuity. And finally, boundary normal directions at the locations of the crossings can indicate if the boundary crossing is smooth or rippled.

The following section presents another case study on 02 Oct 2011 where boundary waves are also observed. This particular case study exhibits a strong negative correlation between the fluctuations of the photoelectron counts and the magnetic field oscillations.

This negative correlation is one of the bases for the identification of boundary wave events. Another case study on 08 Nov 2011 will also be presented as an example of continuous observation of photoelectron population in the ionosphere without any dropout, suggesting a smooth ionospheric boundary. These case studies will highlight the distinct differences between a smooth and a rippled boundary. The methodology on the data selection for the statistical survey will be discussed at the end of this section.

Figure 5.1 and 5.2 show the (a) VEX trajectory, (b) electron energy-time spectrogram of count rate obtained from ELS, (c) the average electron count rate at 22 eV and (d) the 1 Hz magnetic field magnitude plot of the ionosphere perturbation on 02 Oct 2011 and 08 Nov 2011 respectively. Data in (c) is smoothed using a moving average filter of 7 data points. Descriptions of the figure are similar to those in Figure 4.1. Note that on 02 Oct 2011, VEX-ELS operated in 1 sec mode (described in Chapter 3.2.2). Since the electron energy-time spectrogram plots are needed only to identify the ionospheric photoelectron population (which has unique flux intensity peaks of 21-24 eV and 27 eV), this mode of smaller energy range is sufficient for this case study.

VEX observations of the bow shock through to the magnetic barrier region on 02 Oct 2011 and 08 Nov 2011 are similar to those on 26 June 2006 presented in Chapter 4.

5.2.1 Rippled Boundary: VEX pass on 02 Oct 2011

Similar to the ionosphere perturbation on 26 June 2006, there are intervals of photoelectron dropout on 02 Oct 2011. These ten intervals of photoelectron dropouts are shaded in blue and are clearly reflected from the intervals of sudden decreased electron counts at 22 eV (signature energy peak of photoelectron population) in Figure 5.1(c). Furthermore, the magnetic field oscillations also correspond directly to the intervals of photoelectron dropouts. These dip-to-peak and peak-to-dip magnetic field fluctuations immediately adjacent to the 9 photoelectron dropout events are shaded in yellow (apart from one interval labelled “n/a” which is associated with a gap in magnetic field and which will be omitted from the following analysis). MV analysis is implemented over these 18 field magnitudes fluctuations to find if they are ionopause crossings. In the

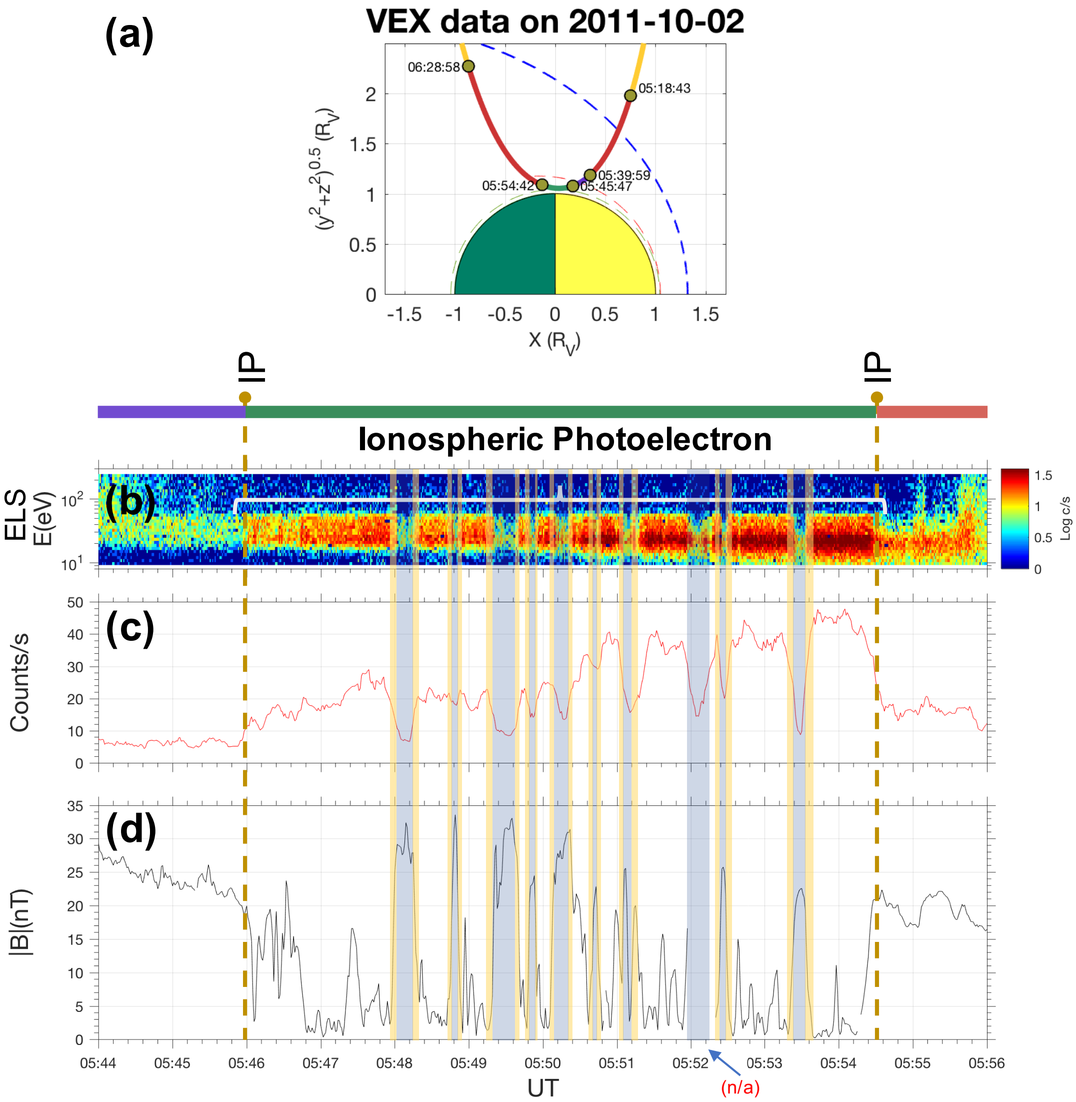

Figure 5.1: An example of an unmagnetised ionosphere perturbation with intervals of clear "photoelectron dropouts" on 02 Oct 2011. (a) The VEX trajectory plot in R_V, (b) electron energy-time spectrogram of count rate obtained from ELS, (c) the average electron count rate at 22 eV (7-point smoothed) and (d) the 1Hz magnetic field magnitude plot of the ionosphere perturbation from 05:44 UT to 05:56 UT. All the ten photoelectron dropouts are shaded in blue. There is missing magnetic field data in the photoelectron dropout interval labelled "n/a". The yellow shaded regions correspond to the dip-to-peak and peak-to-dip magnetic field fluctuations immediately adjacent to the photoelectron dropouts regions.

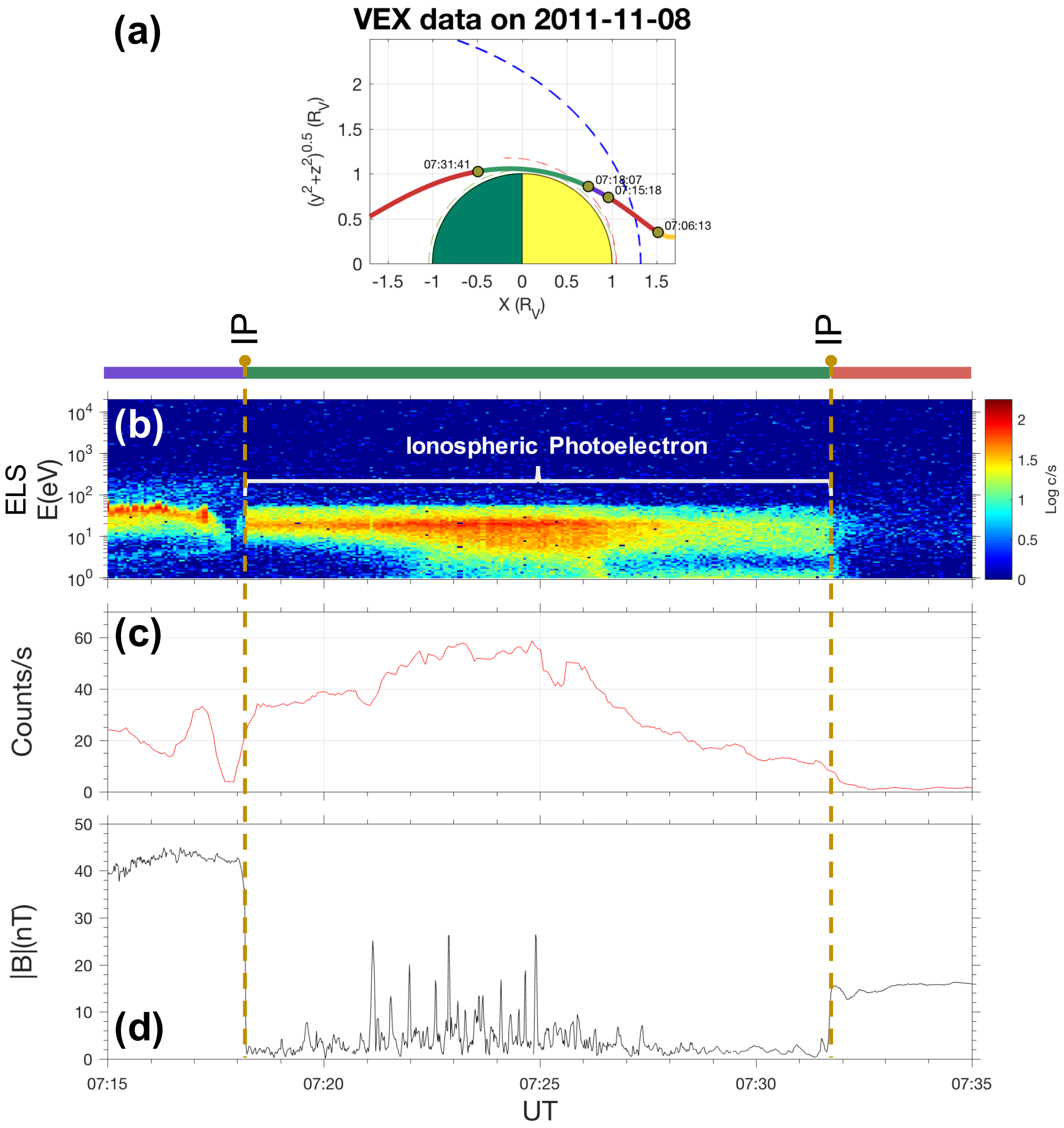

Figure 5.2: An example of the crossing of an unmagnetised ionosphere with no photoelectron dropout events from 07:15 UT to 07:35 UT on 08 Nov 2011. (a) The VEX trajectory plot in R_V (b) The electron energy-time spectrogram of count rate obtained from ELS, (c) the average electron count rate at 22 eV (7-point smoothed) and (d) the 1 Hz magnetic field magnitude plot of the ionosphere perturbation from 07:18 UT to 07:32 UT.

case that they are boundary crossings, MV analysis is used to find the normal directions to all the boundaries. The results are tabulated in Table 5.1.

The intermediate-to-minimum eigenvalues ($\lambda_{int}/\lambda_{min}$) of all 18 intervals are > 3.5 which shows that the minimum variance directions are well defined. All the $|B_n|/|B| < 0.14$ (mean value of 0.06) and $|\triangle B|/|B| > 0.63$ (mean value of 0.86). These values are well within the criteria for tangential discontinuity; $|B_n|/|B| < 4$ and $|\triangle B|/|B| \geq 0.2$, indicating that this boundary represents a tangential discontinuity. In addition, all the angles between $|B_n|$ and $|B|$, $(\theta_{B_n,B}) > 81.8^\circ$ (mean value of 86.5°) which is $\approx 90^\circ$ further indicating all the nine intervals of photoelectron dropouts are tangential discontinuities, a typical characteristic of the Venusian ionopause [*Wolff et al.*, 1980].

As discussed in Chapter 4, if the dayside ionopause is assumed to exist as a smooth quasi-spherical boundary separating the atmospheric plasma from the shocked solar wind, then the boundary normal directions at the locations of the crossings should lie radially outward from the centre of Venus. The results presented here reflect otherwise. The average angle between the boundary normal directions and the radial vectors from the centre of Venus is $\sim 63^\circ$. This quasi-perpendicular orientation indicates the ionospheric boundary which VEX crossed is not smooth but possess a wavelike appearance.

Potential Correlation

The results presented here are consistent to those obtained from the case study on 26 June 2006. However, the intervals of photoelectron dropouts on 02 Oct 2011 are “visually” clearer; in the sense that the presence of photoelectron population can be observed to correspond directly to the low-field unmagnetised ionosphere, and the intervals of photoelectron dropouts can be observed to correspond directly to the high-field magnetic barrier. In fact, the gradual change of the electron counts corresponds negatively to the magnetic field fluctuations. For instance, the gradual decrease (increase) of the electron count rate corresponds directly to the gradual increase (decrease) of the magnetic field magnitude. The mean average value of the correlation coefficient be-

Table 5.1: A summary of the results of the Minimum Variance Analysis on all the photoelectron dropout intervals on 02 Oct 2011 (shown in Figure 5.1) and the single ionopause crossing on 08 Nov 2011 (shown in Figure 5.2).

Time (UT)		MV Direction							
From	To	X	Y	Z	$\lambda_{int}/\lambda_{min}$	$\lvert B_n\rvert/\lvert B\rvert$	$\lvert\triangle B\rvert/\lvert B\rvert$	$\theta_{B_n,B}$ (deg)	Data Point
					02 Oct 2011				
‘05:47:56’	‘05:48:03’	0.187	0.979	0.081	23.04	0.00	0.92	89.8	8
‘05:48:15’	‘05:48:21’	0.070	0.574	-0.816	5.07	0.01	0.74	89.3	7
‘05:48:42’	‘05:48:49’	0.096	0.956	-0.276	42.67	0.07	0.93	86.0	8
‘05:48:49’	‘05:48:55’	0.066	0.986	-0.156	1305.10	0.06	0.89	86.7	7
‘05:49:15’	‘05:49:22’	0.207	0.882	0.423	18.97	0.01	0.95	89.4	8
‘05:49:35’	‘05:49:42’	0.012	-0.607	0.795	10.54	0.01	0.68	89.6	8
‘05:49:47’	‘05:49:50’	0.369	0.868	-0.333	8.66	0.05	0.92	87.3	4
‘05:49:53’	‘05:50:50’	0.109	0.868	-0.485	92.38	0.14	0.89	82.2	8
‘05:50:04’	‘05:50:11’	0.142	0.942	0.303	34.09	0.00	0.93	89.8	8
‘05:50:22’	‘05:50:36’	0.177	0.866	-0.469	4.26	0.09	0.79	85.1	15
‘05:50:37’	‘05:50:42’	0.047	0.738	-0.674	50.77	0.14	0.89	81.8	6
‘05:50:43’	‘05:50:48’	0.070	0.989	0.129	10.01	0.10	0.63	84.2	6
‘05:50:55’	‘05:50:59’	0.324	0.839	0.438	32.14	0.12	0.86	83.3	5
‘05:51:07’	‘05:51:11’	0.111	0.960	0.258	31.27	0.10	0.76	84.2	5
‘05:52:20’	‘05:52:25’	0.083	0.778	-0.622	46.53	0.07	0.87	85.8	6
‘05:52:27’	‘05:52:34’	0.096	0.551	-0.829	3.50	0.02	0.91	89.0	8
‘05:53:19’	‘05:53:25’	0.260	0.472	-0.842	6.07	0.09	0.97	84.9	7
‘05:53:33’	‘05:53:39’	0.246	0.623	-0.743	10.46	0.03	0.89	88.1	7
					08 Nov 2011				
‘07:18:10’	‘07:18:13’	-0.677	-0.119	-0.726	223.13	0.03	0.93	88.4	4

tween all the nine individual average electron count rate and their respective magnetic field is -0.72. The correlation coefficients of each of the nine photoelectron dropout intervals are -0.95 -0.27 -0.92 -0.80 -0.78 -0.56 -0.52 -0.90 and -0.80 respectively. The strength of this correlation of -0.72 is statistically "strong" ([*Evans*, 1996]). However, the correlation coefficient drops to -0.50 if the calculation is done over the entire period of ionosphere region.

Compared to this 'clear' photoelectron dropout events on 02 Oct 2011, the observed dropouts on 26 June 2006 are rather subtle, hence it is referred to as 'pulse-like'. Unlike the 'strong' correlation between the average electron counts at photoelectron energy level and the magnetic field fluctuations on 02 Oct 2011, the calculated correlation coefficient for the whole period of notable photoelectron dropouts (shaded in yellow in Figure 4.2) is only -0.23, which statistically implying a "weak" correlation ([*Evans*, 1996]). This is the main difference between these case studies. One of the reasons was that ELS on 26 June 2006 was operating in 4 sec mode. Even though the ELS was covering the full energy scan, the time resolution is four times less than the 1 sec mode which the ELS operated in on 02 Oct 2011. Had the ELS operated in 1 sec mode, it would have been clearer to identify the intervals of photoelectron dropouts. In addition to the lower time resolution of ELS, this weak correlation can also be due to the fact that the MAG and ELS signals are often noisy. This makes it unreliable to measure the statistical relationship between the photoelectron counts and the magnetic field magnitude. Furthermore, strong correlations are only shown if they are measured by the intervals of photoelectron dropouts, rather than the entire ionosphere region. In summary, it is not feasible to identify the photoelectron dropout events solely based on the correlation between the electron counts (at photoelectron energy level) and the fluctuations in magnetic field magnitude.

5.2.2 Smooth Boundary: VEX pass on 08 Nov 2011

Unlike the previous two case studies, the photoelectron population on 08 Nov 2011 is observed continuously in the ionosphere without any dropout. The inbound ionopause (dayside) is analysed using MV analysis and the results are summarised in Table 5.1. The ionopause outbound crossing on 08 Nov 2011 was in the nightside hence the boundary crossing is not as well defined. Therefore, the outbound ionopause crossing is not analysed. The $\lambda_{int}/\lambda_{min}$ is 223.1 indicate a very well defined minimum variance direction. $|B_n|/|B| = 0.03$, $|\triangle B|/|B| = 0.93$ and $\theta_{B_n,B} = 88.4°$ reveals that the interval is indeed a tangential discontinuity, suggesting that the crossing is the Venusian ionopause. Furthermore, the average angle between the boundary normal directions and the radial vectors from the centre of Venus is only $\sim 2°$. This quasi-parallel orientation indicates the inbound ionospheric boundary at which VEX crossed is a smooth quasi-spherical boundary.

5.2.3 Statistical survey

To measure the distributions of these photoelectron dropout events regardless if they are 'clear' or 'pulse-like' dropouts, an approach has been taken in this work to visually survey all the available ELS data from 2006 to 2014. Comparing to the case on 08 Nov 2011 (Figure 5.2) where the photoelectron population is observed continuously, it is rather straightforward to observe the photoelectron dropout cases as shown previously in Figure 5.1 and 4.2 respectively. Since identifications based on the correlation coefficient between the electron counts and magnetic field magnitude is not feasible, surveying by eye is a preferred approach. However, it will be an interest for future work to develop a numerical framework to identify these events in a more systematic fashion.

Results of the conducted statistical survey show that the photoelectron dropout events on 02 Oct 2011 and 26 June 2006 are not uncommon. After excluding the orbits where the ELS and/or MAG data are unavailable when VEX was in the ionosphere, as well as orbits when ionospheric photoelectron populations are not observed at all, around 23% (495 orbits) show at least one or more intervals of photoelectron dropouts out of the remaining 2141 orbits from Apr 2006 to Nov 2014.

The MV analysis approach is applied to all the dip-to-peak and peak-to-dip field fluctuations immediately adjacent to the intervals of photoelectron dropout identified across the full data set. Note that unlike the unmagnetised ionosphere, the field magnitude in a magnetised ionosphere is similar to that observed in the magnetic barrier region. Hence, for the orbits when photoelectron dropouts are observed, the dip-to-peak and peak-to-dip field fluctuations in a magnetised ionosphere cannot be clearly identified. This results in only 371 unique orbits (from a total of 495 events) selected for further analysis. In these 371 orbits, 1043 intervals of photoelectron dropouts are observed, hence 2086 field fluctuations. Since MV analysis is only valid with 3 or more data points, only 1633 field fluctuations (from a total of 2086) which have 6 or more data points are selected. Analysis conducted using more data points would result in smaller data sets, and less data points would result in a higher statistical uncertainty [*Sonnerup and Scheible*, 1998]. The resulting distributions of the boundary normal directions are similar using between 3 and 9 data points. The use of a minimum of 6 data points is chosen as a compromise between the number of data sets and the statistical uncertainty.

Around 98% (1603 out of 1633 intervals) of all the minimum variance directions have $|B_n|/|B| < 0.4$ and $|\triangle B|/|B| \geq 0.2$, indicating a tangential discontinuity. Similarly, around 95% (1562 out of 1633 intervals) have $\theta_{B_n,B} > 75°$ further indicating that the analysed intervals are tangential discontinuities. This is again consistent with the characteristics of the Venusian ionopause [*Wolff et al.*, 1980]. Furthermore, more than 88% (1446 out of 1633 intervals) have $\lambda_{int}/\lambda_{min} > 3$, which shows that the minimum variance directions are well defined. In total, around 84% (1374 out of 1633 intervals) of all the minimum variance directions have $|B_n|/|B| < 0.4$, $|\triangle B|/|B| \geq 0.2$ and $\theta_{B_n,B} > 75°$ (tangential discontinuity), and have $\lambda_{int}/\lambda_{min} > 3$ (well defined directions). These results imply that the multiple photoelectron dropout events observed during each of these orbits, are due to VEX traversing the ionospheric boundary multiple times. For example on 02 Oct 2011, VEX traversed through the ionospheric boundary 9 times on a single trajectory.

In addition to the previous analysis, a total of 251 VEX passes with ionospheric boundary crossings that are similar to the case presented on 08 Nov 2011 (no photoelectron dropout) are collected. The criteria used to select this data was (1) no observations of photoelectron dropout events, (2) only gradual ionospheric crossings without magnetic intermediary and (3) clear passes from high field magnetic barrier to low field unmagnetised ionosphere. Results of MV analysis show that the minimum variance directions are very well defined with more than 96% (242 out of 251) of the directions having $\lambda_{int}/\lambda_{min} > 3$. The results also suggest that the crossings are ionospheric boundary with more than 98% (247 out of 251) having $\theta_{B_n,B} > 75°$ and around 100% (250 out of 251) having $|B_n|/|B| < 0.4$ and $|\triangle B|/|B| \geq 0.2$.

5.3 Normal directions of boundary crossings

For the cases where no photoelectron dropout event is observed, all of the normal directions for the 238 (out of 251) ionopause crossings with $\lambda_{int}/\lambda_{min} \geq 3$ and number of data points ≥ 6 are binned in a three dimensional polar statistical histogram with an azimuthal ϕ bin size of 7.5° and elevation α bin size of 3.75° in Figure 5.3(a). The colourbar at the bottom of the histogram is the number of boundary crossings in each bin. For ease of comparison, all minimum variance directions with negative Z_{VSO} components are rotated into the positive Z_{VSO} direction and the local positions of the boundary crossings are shifted to the northern polar point ($\alpha = 90°$) so that all directions can be visualised and compared in a single directional hemisphere.

For an ideally smooth quasi-spherical ionospheric boundary, the boundary normal directions at the locations of the crossings should lie radially outward from the centre of Venus, i.e. quasi-parallel orientation between the red and blue dashed arrows, as illustrated in Figure 5.3(c). Note that the illustration of the symmetric ionospheric boundary is visualized on the basis that the nominal altitude of ionopause is not SZA dependant [*Zhang et al.*, 2008a].

This smooth quasi-spherical property of ionospheric boundary can be reflected from the results shown in Figure 5.3(a). Observable from Figure 5.3(a), around 91% (217 out of 238) of the boundary normal directions fall in the elevation range of $\alpha > 67.5°$. As the locations of boundary crossings are shifted to the northern polar region, this highly populated region in the elevation range of $\alpha > 67.5°$ implies quasi-radial boundary nor-

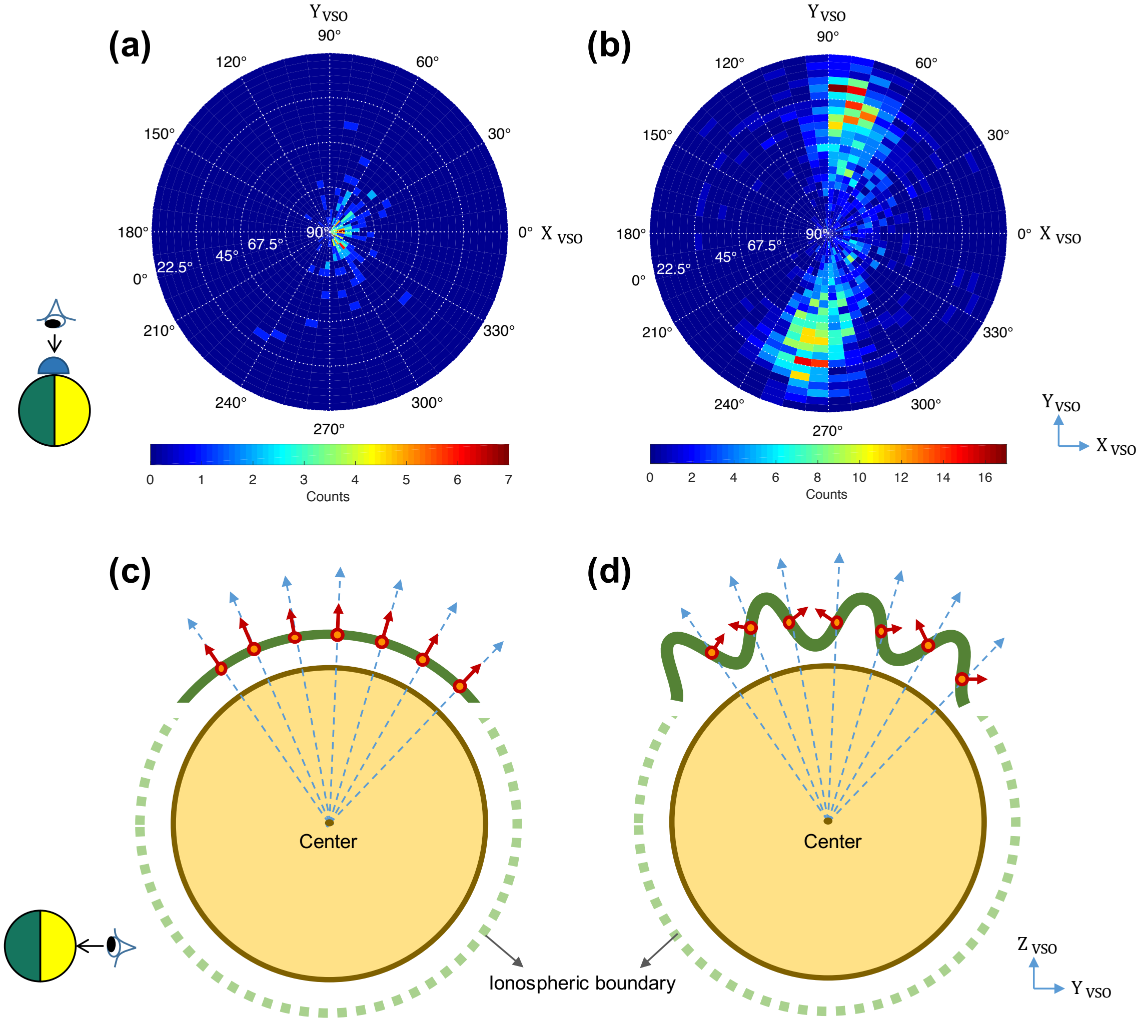

Figure 5.3: All the normal directions of the ionospheric boundary crossings are binned in a three dimensional polar statistical histogram for ionospheric boundary crossings cases with (a) no observation of photoelectron dropout events as well as (b) observations of photoelectron dropout events with an azimuthal ϕ bin size of 7.5° and elevation α bin size of 3.75°. (a) and (b) are computed from a total of 238 and 1446 events respectively with criteria of $\lambda_{int}/\lambda_{min} \geq 3$ and number of data points ≥ 6. The colourbars at the bottom of the histograms are the number of counts in each bin. Illustrative diagrams that show the projections of normal directions of ionospheric boundary crossings especially in the northern polar regions where all of the boundary crossings are observed for (c) a smooth ionospheric boundary and (d) a rippled ionospheric boundary. The green line represents the ionospheric boundary. The blue dashed arrows represent vectors projected radially from the centre of Venus through its local locations. The red arrows represent normal directions of boundary crossings projected from its local locations which are denoted by the orange coloured dots.

mal directions from the centre of Venus. This suggests that the ionospheric boundary where VEX crossed is smooth and quasi-spherical (i.e. Figure 5.3(c)).

On the other hand, this scenario of smooth Venusian ionospheric boundary is not reflected for the cases where photoelectron dropout events are observed. All of the 1446 well defined boundary normal directions from the photoelectron dropout intervals are binned in a similar three dimensional polar statistical histogram as shown in Figure 5.3(b). Observable from Figure 5.3(b), the surface bins are more populated in the azimuthal range of $60^\circ < \phi < 120^\circ$ and $240^\circ < \phi < 300^\circ$ as well as in the elevation range of $\alpha < 45^\circ$. In comparison to the smooth boundary case presented in Figure 5.3(a), only around 23% (333 out of 1446) of the boundary normal directions fall in the elevation range of $\alpha > 67.5^\circ$. This shows that instead of propagating radially outward from the centre of Venus, the majority of the normal directions of the boundary crossings lie in the Y-Z $_{VSO}$ plane with more dominant components along the Y_{VSO} axis.

In contrast to Figure 5.3(a), the results from Figure 5.3(b) imply that, where the ionospheric boundary is crossed multiple times, the ionopause crossings from the photoelectron dropout cases do not result from a smooth ionospheric boundary locally, but an ionospheric boundary that can exist in a wave along the Y-Z $_{VSO}$ plane and in a direction dominantly along the Y_{VSO} axis. This is illustrated in Figure 5.3(d).

Note that, due to the highly elliptical polar orbit of VEX, the ionopause is sampled only around the northern polar region of Venus. Therefore, the illustrative diagram in Figure 5.3 is only limited to the northern polar region of Venus.

To analyse if the observations of boundary wave events might be biased on the spacecraft trajectory, Figure 5.4 presents a polar histogram of the VEX trajectories when rippled ionospheric boundary events are observed. With $+Y_{VSO}$ axis as the reference vector, the VEX trajectory is expressed by the angle between the spacecraft orbital and the terminator plane (Y-Z $_{VSO}$), which the angle ranges from 0° to 180°. The results show that all the minimum variance directions are obtained from a variety of VEX trajectories, i.e. the consistent minimum variance directions shown above are not

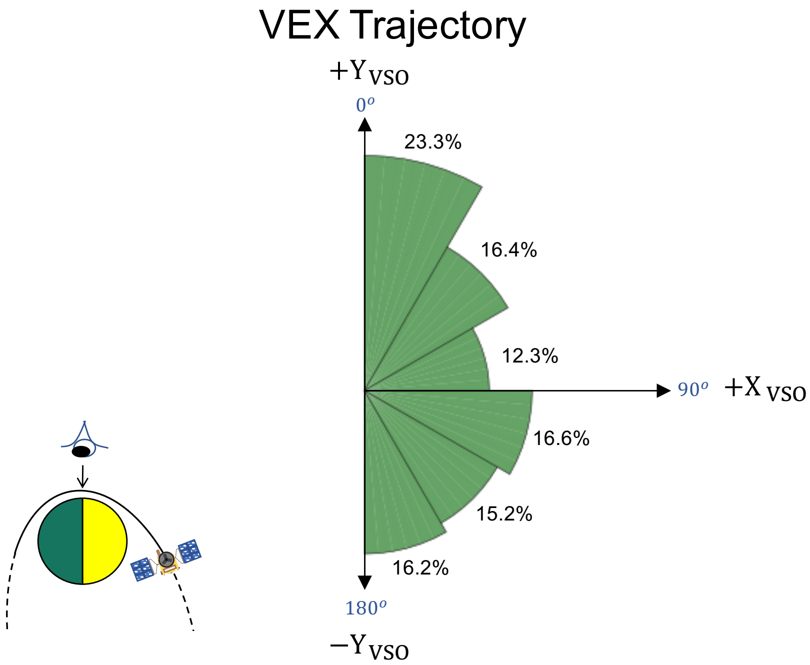

Figure 5.4: A polar histogram of a total of 195 VEX trajectories when rippled ionospheric boundary events are observed. The VEX trajectory is expressed by the angle between the orbital and the terminator plane (Y-Z $_{VSO}$) with $+Y_{VSO}$ axis as the reference vector.

biased towards any particular VEX orbit.

Crossings of the magnetic flux ropes [*Russell and Elphic*, 1979; *Russell*, 1990; *Wolff et al.*, 1980] should be, in theory in an idealised hydromagnetic state, similar to crossings of the Venusian ionospheric boundary. Both are tangential discontinuity boundaries [*Spreiter et al.*, 1970; *Wolff et al.*, 1979]. Regardless if the flux ropes are considered in this polar statistical histogram, the results which show the ionospheric boundary existing in a wave along the Y-Z $_{VSO}$ plane still hold. Further discussions on flux rope will be covered in detail later in Section 5.6.

In summary, the analysis of all the ionospheric boundary crossings from 2006 to 2014 reveals that the Venusian ionospheric boundary is not always smooth, but a boundary that often exhibits a wavelike appearance in the northern polar region, where all of the boundary crossings are observed. Figure 5.5 presents an illustrative diagram to show how the wavelike characteristic of Venusian ionospheric boundary with the perturbation of a flux rope can be visualised from the simultaneous observations of

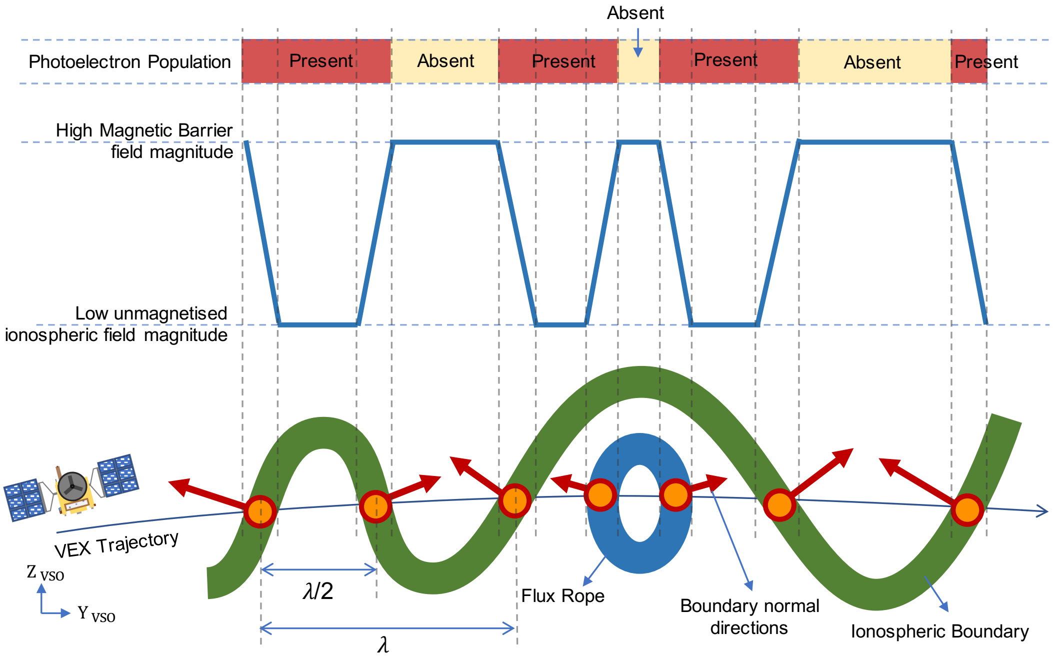

Figure 5.5: An example of illustrative diagram showing how the ionospheric photoelectron dropout events (top panel) and the changes in magnetic field magnitude (middle panel) can be related to the possible VEX trajectory through multiple ionospheric crossings and flux ropes (bottom panel). The red arrows represent normal directions of boundary crossings projected from its local locations which are denoted by the orange coloured dots. λ and $\lambda/2$ denote estimated half-width and full width of the ionospheric boundary wave.

photoelectron dropout events (top panel) and the changes in magnetic field magnitude (middle panel). This illustration is consistent to the photoelectron dropout case studies presented earlier.

5.4 ‘Smooth’ ionospheric boundary

The analysis in the previous section has identified a total of 238 ‘smooth’ ionospheric boundary crossing cases. In this section, this data set is utilised to estimate the ionospheric boundary thickness and assess its dynamics in relation to the external pressure as well as the altitude where it is observed.

The thickness of each boundary crossing is estimated by the product of the VEX velocity (V_{VEX}) and the time spent crossing the boundary $\triangle T$, and multiplying by $\cos(\beta_{vex})$ where β_{vex} is the angle between the spacecraft velocity vector and the boundary normal

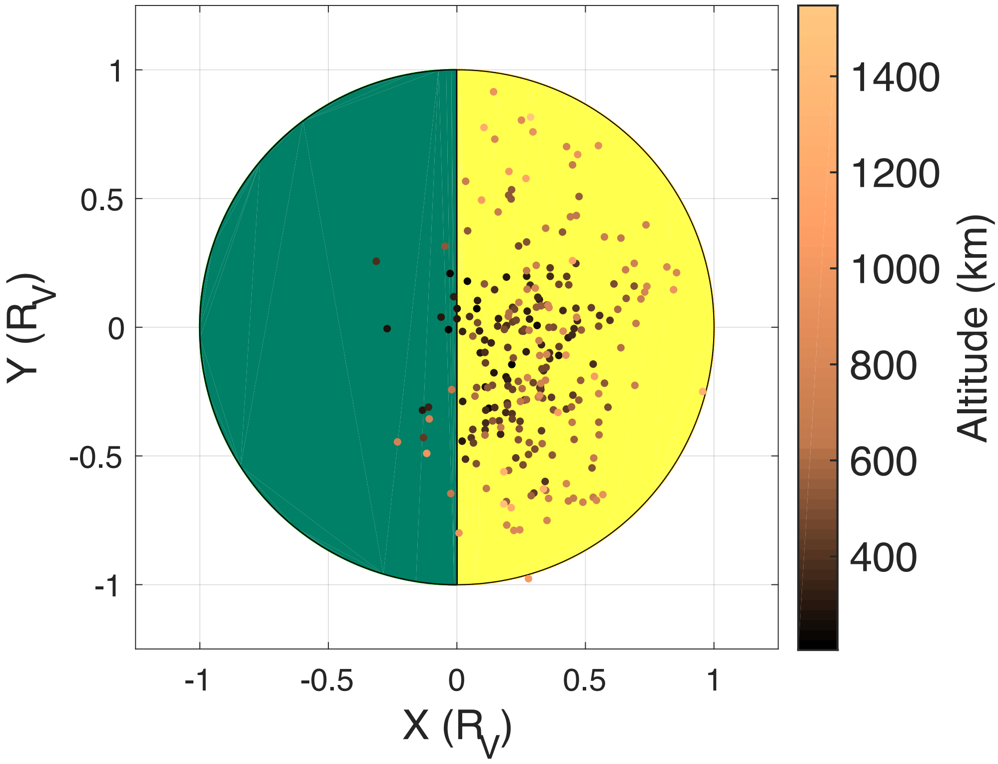

Figure 5.6: The locations of all the analysed 'smooth' boundary crossings are represented in coloured dots in the X-Y $_{VSO}$ plane. Units are in R_V. The altitudes of the boundary crossings are indicated by the colour scale on the right.

vector:

$$\text{Ionopause Thickness} = V_{VEX} \times \triangle T \times \cos(\beta_{vex}) \tag{5.1}$$

As only boundary crossings of VEX passes with no observation of photoelectron dropout are selected, this estimation of the thickness is based on the assumption that the ionopause is smooth and quasi-spherical in the dayside region of Venus. This has been shown to be the case in Section 5.3, i.e. Figure 5.3(c).

However, due to the nature of VEX's highly polar orbital plane with periapsis always in the northern region, the VEX trajectory tend to be $\sim 90°$ to the boundary normal directions. So the estimated thickness $\rightarrow 0$ as $\cos(\beta_{vex}) \rightarrow 0$. To eliminate the arbitrary values that might arise due to $\beta_{vex} \rightarrow 90°$, only VEX passes with $\beta_{vex} < 75°$ are considered. Note that the estimation with VEX passes of $\beta_{vex} > 75°$ are still technically correct but the whole distribution would be shifted towards zero with median value closer to zero.

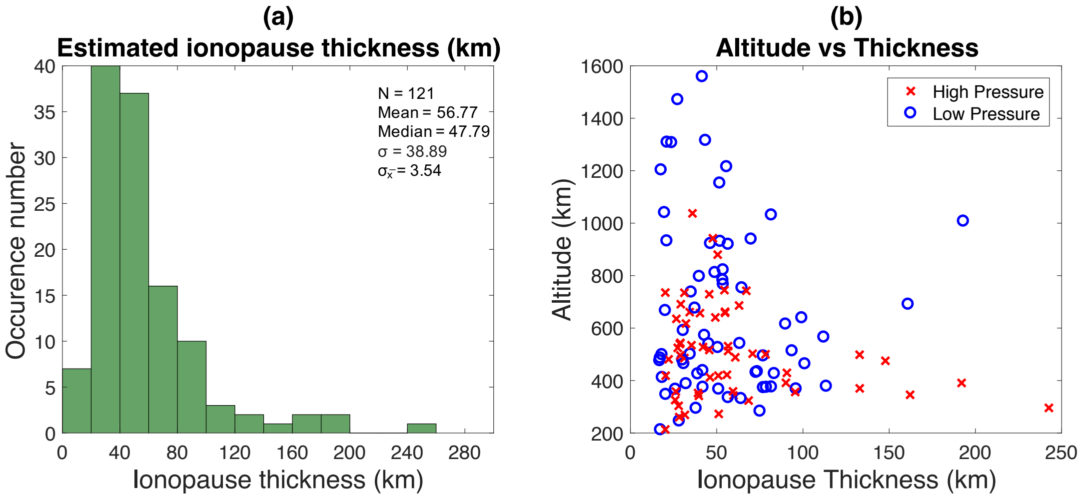

Figure 5.7: (a) A histogram of the estimated ionopause thickness from a total of 121 crossings. Bin size is 20 km. Range: from 17 km to 2423 km. (b) A scatter plot of the locations of the boundary crossings against the estimated ionopause thickness. Blue circles and red crosses denote values obtained from lower and higher range of magnetic pressure respectively.

A total of 121 boundary crossings are selected with this criteria as well as $\lambda_{int}/\lambda_{min}$ ≥ 3 and number of data points ≥ 6. Figure 5.7 shows (a) a histogram of the estimated ionopause thickness and (b) a scatter plot of the locations of the boundary crossings against the estimated ionopause thickness. Blue circles and red crosses in the scatter plot denote values obtained from lower and higher range of external pressure in the magnetic barrier respectively. The external pressure is estimated using the magnetic pressure in the magnetic barrier.

As discussed earlier in Chapter 2.3.1, the ionopause, forms at an altitude where the total pressure balance (i.e. the thermal (nk_BT), magnetic ($B^2/2\mu_0$) and dynamic (ρv^2) pressures) is in equilibrium between the ionosphere and magnetic barrier regions. In the magnetic barrier, the solar wind dynamic pressure term is converted to primarily magnetic pressure through depletion of solar wind plasma and the thermal pressure becomes insignificant [*Zwan and Wolf*, 1976; *Brace and Kliore*, 1991; *Brace et al.*, 1980]. Hence, the total external pressure exerted on the ionosphere is dominated and can be estimated by the magnetic pressure P_B. It is calculated as:

$$P_B = \frac{\mathbf{B}^2}{2\mu_0} \tag{5.2}$$

where $\mathbf{B}$ is the field magnitude and μ_0 is the permeability of free space. The median value of the pressure distribution of these 121 boundary crossings is 0.354 nPa. The mean average magnetic pressure is 0.399 ± 0.0170 nPa with a range from 1.929 pPa to 1.425 nPa. This average value is expressed in *mean ± standard error* values of the distributions and this expression is implemented for all succeeding calculations. In this section, pressure that is lower (higher) than 0.354 nPa is considered the lower (higher) pressure.

5.4.1 Ionopause thickness

The distribution of the average boundary thickness is a single peak positively skewed distribution with a median value of 48 km and a mode class of 20-40 km. Mode class is the most frequent range of values in a distribution. It ranges from 17 km to 243 km and has a mean average thickness of 57 ± 4 km. The lower 0.25 and higher 0.75 quantiles are 31 km and 70 km respectively. Figure 5.7(b) shows that there is a three-way relationship between the altitude where the boundary is crossed, the boundary thickness and the external pressure exerted on the ionopause. For instance, the boundary at higher altitude (>1000 km) is thinner (scale size of 10-60 km) for lower external pressure. On the other hand, the boundary is thicker (scale size of 130-250 km) at lower altitude (<600 km) for higher external pressure. It is also noteworthy to mention that lower (higher) external pressure usually results in ionopause forming at higher (lower) altitudes as discussed in Chapter 2.

The results are obtained based on the assumption that the boundary where VEX crossed is smooth locally. A slight change of the boundary shape locally will result in fluctuation in the boundary normal directions. This could then lead to variation in the estimated values of boundary thickness via the $\cos(\beta_{vex})$ term. Furthermore, the ionopause is also assumed to be stationary. This assumption should be correct most of the times considering the large inertia of the ionosphere. The fluctuations of the ionopause altitude will be discussed in detail in Chapter 6.3. These assumptions could add uncertainties to the results which may lead to some of the slightly scattered values.

5.4.2 Comparison to *Elphic et al.* [1981]

Using the magnetometer, plasma wave detector and Langmuir probe onboard of PVO, *Elphic et al.* [1981] presents a thorough analysis on the scale thickness of the Venusian ionopause during the solar maximum period. The current sheet in their work was identified based on the negative coincidence between the electron number density and the magnetic field gradient through the ionopause.

The three-way relationship between the boundary altitude, thickness and the external pressure shown in Figure 5.7(b) is also reflected in a similar fashion in *Elphic et al.* [1981]. The authors found that the current sheet is thinner (scale size of 10-50 km) for weaker solar wind magnetic field magnitude (thus lower external pressure) at altitude >300 km. On the other hand, the current sheet is thicker (scale size of 60-90 km) for stronger external field (thus higher external pressure) at altitude <300 km. The authors explain that the boundary thickness can be affected by the external pressure due to the different collisional properties at different altitude. For example, stronger pressure results in lower ionopause altitude and the effects of ionospheric plasma collisions with neutral particles become more significant. This can lead to diffusion and subsequently broadening of the boundary layer.

It is also noteworthy to mention that the estimated ionopause thickness in this work is roughly 1.5 times more than those estimated in *Elphic et al.* [1981]. Based on 62 number of events collected from PVO mission, *Elphic et al.* [1981] shows that the distribution of the ionopause boundary thickness is in a rather narrow range, from 20-40 km. Note that the values estimated in their study are measured based only on the time spent crossing the boundary. So the values are expected to be smaller (factor of 0.707 based on the assumption that spacecraft trajectory is $\sim 45^\circ$ to the boundary crossings). Similarly, based on a selection of 17 ionopause crossings, *Elphic et al.* [1980] reports an average current sheet thickness of 48 ± 24 km, similar to a few ionospheric ion gyroradii. Although the authors did attribute the thickness variability to the boundary motions.

This difference in the estimated boundary thickness is likely due to the different solar activity periods the data are collected during, as shown in Figure 3.3. The analysis in *Elphic et al.* [1981] was conducted during the first few years of PVO operation, when the external pressure is much stronger during the solar maximum period. The results presented here are obtained during one of the quietest solar minimum of the century, where the external pressure is much weaker. For the same reason discussed above, this weaker external pressure during solar minimum could lead to a relatively thicker ionospheric boundary layer for the results presented here (compared to those estimated using PVO data).

5.4.3 Summary

The results presented in this section is the first analysis on the ionospheric boundary thickness conducted for the entire VEX mission duration, which covers mainly the solar minimum period. The results are consistent and complement the study by *Elphic et al.* [1981] which covers the solar maximum period. In addition, the presence of ionospheric photoelectron population correspond directly to the higher limit of the ionopause boundary layer, i.e. the photoelectron populations are present within the ionospheric current sheet as well as in the ionosphere.

One should also note that, one of the criteria for the data selection for this smooth boundary case is to only consider a clear VEX pass from high field magnetic barrier to low field ionosphere without magnetic intermediary. This means that all the boundary crossings identified here are sampled only during an unmagnetised ionosphere. Magnetisation states of the ionosphere are often associated with the variation of the solar activity and external pressure. However, ionopause crossings cannot be correctly identified for a magnetised ionosphere. This is because the magnetic field change from the high field barrier region will be suppressed by the also high field ionosphere, making the field change unclear and MV analysis cannot be performed. Nevertheless, the data analysis presented in this section has included the role of the variation in the external magnetic pressure (thus the role of field magnitude). Hence, it is expected that the three-way relationship between the boundary altitude, thickness and the external pressure should also hold for magnetised ionosphere. It will be an interest for future work to assess the magnetised ionosphere cases in the dynamics of the boundary layer thickness. The estimated boundary thickness, which ranges from 30 km to 70 km (which correspond to the lower 0.25 and 0.75 quantiles) will be utilised in Chapter 6 to validate the estimated wavelength of previous simulation studies on Kelvin-Helmholtz waves.

5.5 'Rippled' ionospheric boundary

5.5.1 Locations

Due to the polar orbit of VEX, the ionosphere is only sampled at the northern polar region, hence the ionospheric boundary wave events are observed in a rather small range of locations around the northern polar region with elevation $> 39°$, (90% of the observations are made $> 61°$) as shown in Figure 5.8. The mean average altitude is 342 ± 3 km. It ranges from around 168 km to 1026 km, with 90% of the passes made below 475 km. These boundary wave events are observed everywhere in this small range of locations and do not show any particular preferred location.

5.5.2 Sizes - boundary wave width

With the assumption that the spacecraft crosses into a stationary boundary wave, the half-width of the boundary wave, $\lambda/2$ as illustrated in Figure 5.9(c) can be estimated by the product of the VEX velocity (VEX has velocity ~9.5 km s^{-1} around the periapsis) and the time spent between two consecutive boundary crossings. The estimation is made under two criteria: (1) Only two consecutive boundary crossings when α_{mv}, the angle between their respective boundary normal directions, is less than 30° or greater than 150°, are selected to eliminate the crossings of boundary waves that are still in the linear growth phase; i.e. only developed waves are selected, (2) only boundary crossings when β_{vex}, the angle between the spacecraft velocity vector and the boundary normal vector is less than 45° are selected to eliminate the boundary crossings of the 'near-tips' of the waves as illustrated in Figure 5.9(c) and to eliminate the boundary which

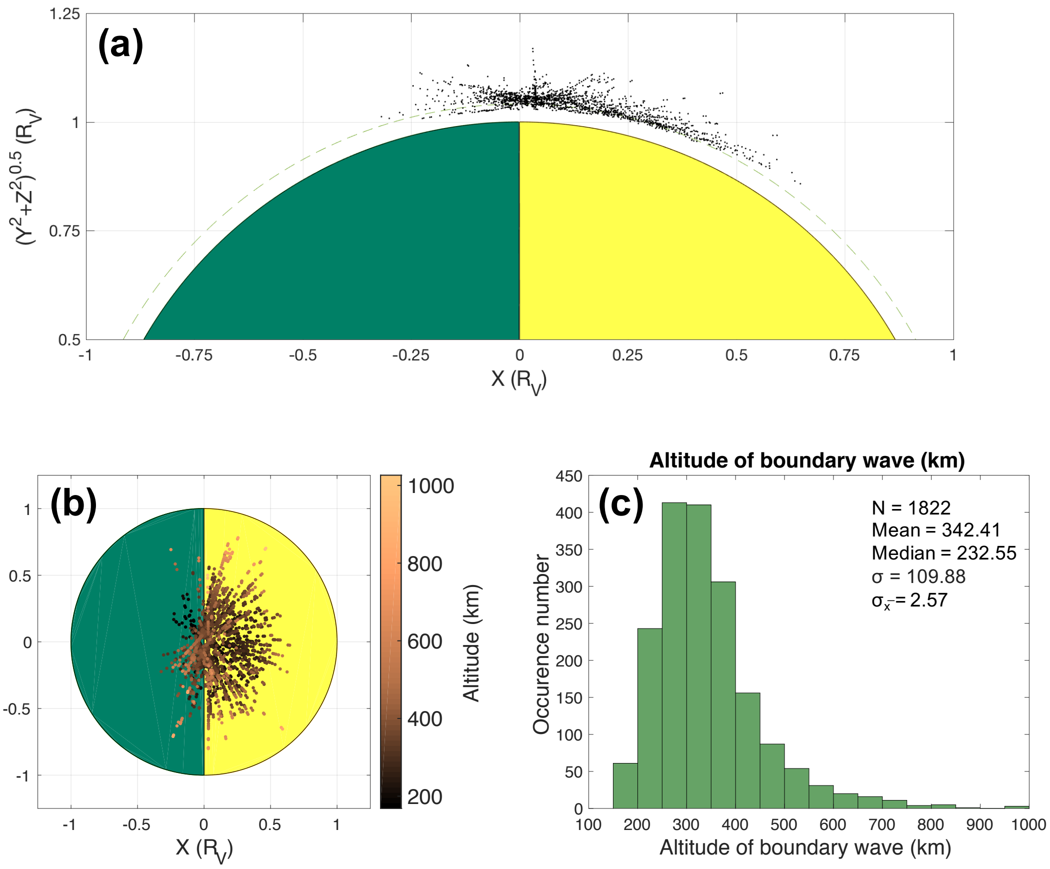

Figure 5.8: (a) The locations of the boundary wave are represented in black dots. They are plotted in a plane where the X-axis is along the X_{VSO} axis and the Y-axis is expressed in $\sqrt{Y^2+Z^2}$. The nominal altitude of ionopause is represented in green dashed line [*Zhang et al.*, 2008a]. (b) The locations of the boundary wave are represented in coloured dots in the X-Y $_{VSO}$ plane. Units are in R_V. The altitudes of the boundary crossings are indicated by the colour scale on the right. (c) A histogram of the altitude of the boundary wave crossings from a total of 1822 events. Bin size is 50 km. Range: from 168 km to 1026 km. The lower 0.25 and higher 0.75 quantiles are 269 km and 387 km respectively.

is crossed at a large angle by the VEX. These criteria yields a total of 89 boundary wave events. Note that the data of VEX, a single spacecraft mission, could only allow the estimations of the boundary normal directions but not the shape of the boundary wave. Hence the ionopause is expressed in a dashed line shaped question mark in the last schematic diagram in Figure 5.9(c) indicating an undefinable shape.

A histogram of the estimated widths of the boundary wave, λ of the 89 events with a bin size of 50 km is presented in Figure 5.9(a). The distribution of the boundary wave widths is a single peak positively skewed distribution with a median value of 173 km

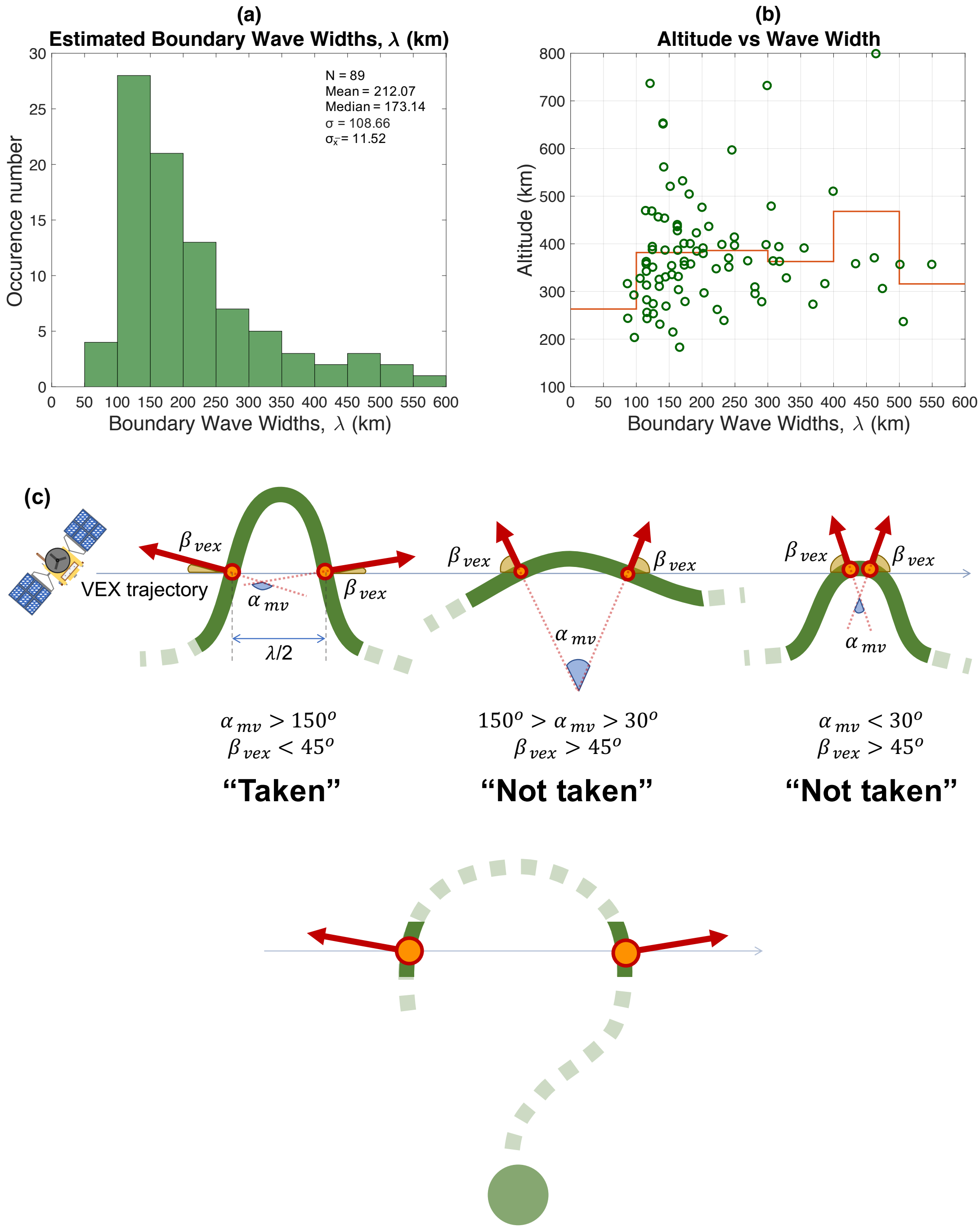

Figure 5.9: (a) A histogram of the estimated ionospheric boundary wave widths, λ from a total of 89 events from 2006 to 2014. Bin size is 50 km. Range: from 87 km to 550 km. (b) A scatter plot of the altitudes of the observed boundary wave against its estimated widths, λ. The red line is the mean average value of altitude for each 100 km λ bin. (c) Illustrative diagrams showing the criteria used in estimating the boundary wave widths. The criteria are $\alpha_{mv} < 30°$ or $> 150°$ and $\beta_{vex} < 45°$. The red arrows represent the normal directions of boundary crossings projected from its local locations which are denoted by the orange coloured dots. The ionospheric boundary is represented in green lines. β_{vex} is the angle between the spacecraft velocity vector and the boundary normal vector. α_{mv} is the angle between the boundary normal directions from two consecutive crossings.

and a mode class of 100-150 km. It ranges from 87 km to 550 km and has a mean average width, λ of 212 ± 12 km. The lower 0.25 and higher 0.75 quantiles are 135 km and 255 km respectively. A scatter plot of the altitudes where boundary wave events are observed against its estimated widths is presented in Figure 5.9(b). Red line is the mean average value of altitude for each 100 km λ bin. Results show that the mean average wave width is rather consistent at all altitudes and no dependence is reflected. Note that only a small number of data points for bigger boundary waves are considered here. Additional analysis conducted with criterion $\beta_{vex} < 30^\circ$ yields only 41 events but results in a similar mean average width, λ of 219 ± 17 km.

Note that if a boundary wave is configured similar to the three phases of the KHI evolution [*Amerstorfer et al.*, 2010], there are many possible ways that VEX can traverse through a boundary wave. Hence, with the limitations of the instruments on board of VEX, which is also a single spacecraft mission, estimations of the exact shape and thus the size of the observed boundary wave, are not possible.

5.6 Magnetic Flux ropes

As discussed earlier in Section 5.3, boundary crossings of both the magnetic flux ropes and the Venusian ionospheric boundary are similar, where both are tangential discontinuity boundaries [*Spreiter et al.*, 1970; *Wolff et al.*, 1979]. In this section, all flux ropes will be singled out from the boundary crossings for further analyses.

The crossings of flux ropes (Figure 2.5) can be identified by the unique changes of magnetic field signature as previously discussed in Chapter 4.4. Transformation to MV coordinates would allow the analysis of magnetic field magnitude changes in a plane perpendicular to the minimum variance direction. Therefore, for a spacecraft to cross the centre of an ideally circular flux rope as pictured in Figure 5.10(a), the resulted B_{min} would lie along the VEX trajectory, depicted as the green coloured arrow. Through the inbound crossing, the axial magnetic field magnitude (into/out of the page along B_{max}) increases and eventually peaks at the centre of the flux rope. At the same time, the azimuthal magnetic field magnitude (along B_{int}) reaches minimal at the centre before

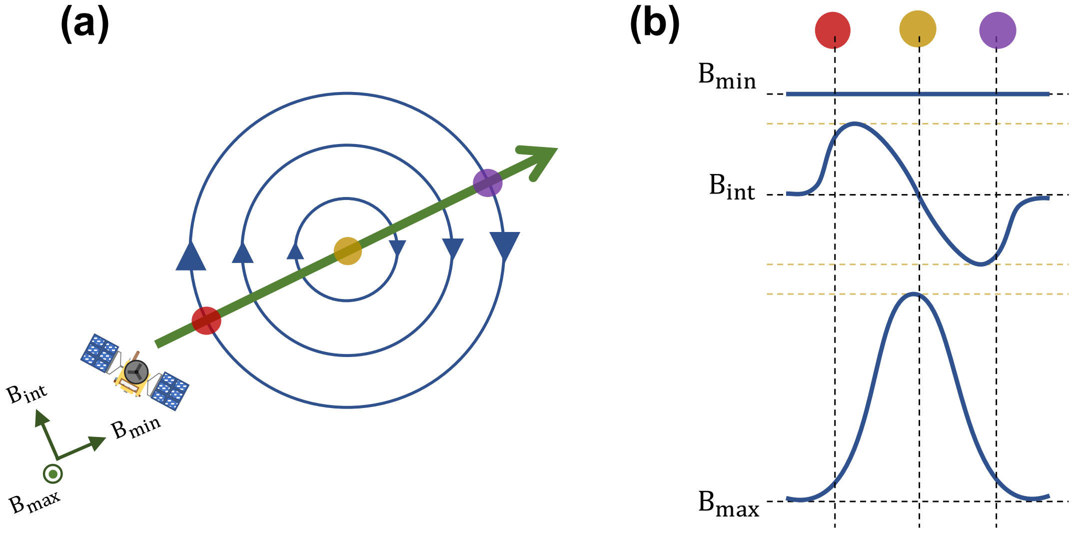

Through the centre of flux rope

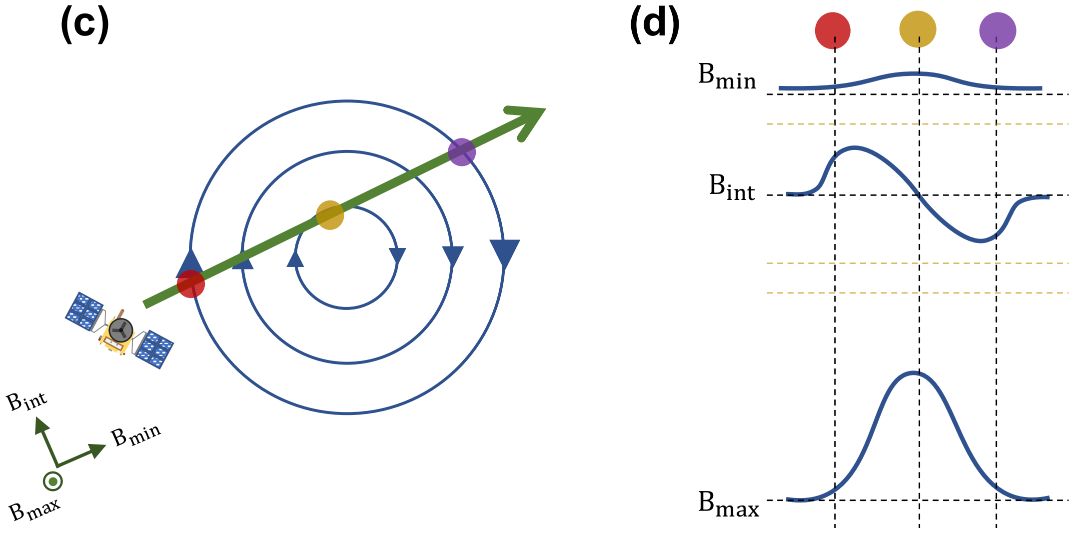

NOT through the centre of flux rope

Figure 5.10: Descriptions are similar to Figure 4.7. (a) and (c) show illustrations of VEX passing through the centre and off-centre of a flux rope. (b) and (d) show the expected changes of the magnetic field components in the minimum, intermediate and maximum variance coordinates for both cases. Green arrow represents the trajectory of VEX. The red, yellow and purple-coloured dots correspond to different spacecraft locations in a flux rope, i.e. Figure 2.5.

increasing again in the opposite direction towards the outbound boundary. Similar to the inbound mechanism but in a revered order, the axial field magnitude decreases and returns to minimal again at the outbound boundary. These changes in the respective individual components are clearly illustrated in Figure 5.10(b). Note that the directions of B_{int} and B_{max} are arbitrary. In this particular example provided, B_{max} and B_{int} represents the axial and the azimuthal field component of the flux rope respectively. This is true for an axially strong flux rope. Although infrequent, there are flux ropes where the axial field is not as strong as the case presented, for which the maximal change of field lies azimuthally. And in this case, the azimuthal and axial field components of the flux ropes are represented along B_{max} and B_{int} respectively.

Hodograms show the field change in the plane of B_{max}/B_{int} and B_{max}/B_{min}. If the field change in the individual variance directions through a flux rope is represented using hodograms, then the crossing of a flux rope will result in a "potato chip" shape hodogram. An example is shown in Figure 5.11(a). This unique "potato chip" shape hodogram is a key identifier of a crossing of a flux rope [*Russell*, 1990]. This particular hodogram presented in Figure 5.11(a) is actually obtained from a flux rope encountered in the case study on 02 Oct 2011. This flux rope corresponds to a dip-to-peak-to-dip field change from 05:48:41 UT to 05:48:55 UT. Note the consistent similarity between the flux rope encountered on 02 Oct 2011 as well as on 26 June 2006 (i.e. Figure 4.9). For comparison, the hodogram of an "ordinary" ionospheric boundary crossing obtained just before the flux rope on 02 Oct 2011 is presented in Figure 5.11(b). This boundary crossing is analysed from 05:47:56 UT to 05:48:09 UT. The starts of both hodograms are marked with blue circles. Unlike the crossing of a flux rope, the hodograms of this "ordinary" boundary crossing are rather linear. They do not indicate any three-dimensional field rotation and "potato chip" shape signature of a flux rope. Also note that as only the field change in the B_{max}/B_{int} plane is of interest, the change in direction between B_{max} and B_{int} will not affect this signature of a flux rope.

Also illustrated in Figure 5.10(c) is a case example of a flux rope crossing that is not through its exact centre. The changes in field magnitude along the variance directions for this case example are reflected in Figure 5.10(d). For the same flux rope, off centre

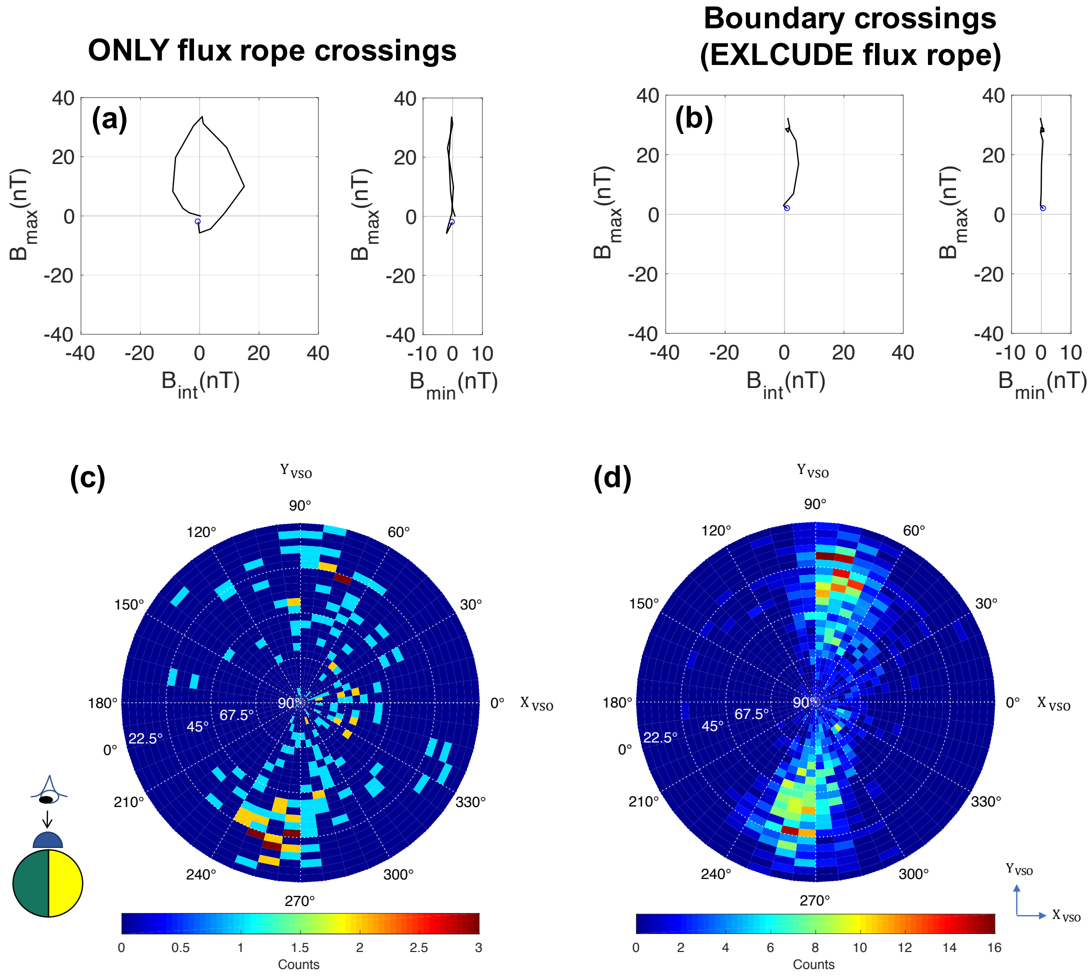

Figure 5.11: Hodogram of (a) a flux rope from 05:48:41 UT to 05:48:55 UT with $\lambda_{int}/\lambda_{min} \approx 55$ and (b) an ionospheric boundary crossing (analysed just before the encounter of flux rope) from 05:47:56 to 05:48:09 with $\lambda_{int}/\lambda_{min} \approx 9$ on 02 Oct 2011. All the normal directions of the boundary crossings are binned in a three dimensional polar histogram for ionospheric boundary crossings cases of (c) only flux ropes and (d) all photoelectron dropout intervals excluding flux ropes for comparison. (c) and (d) are computed from a total of 177 and 1269 events respectively. Both histograms are with an azimuthal ϕ bin size of 7.5° and elevation α bin size of 3.75°.

crossing results in non zero (but still small) field magnitude along B_{min}. The magnetic field magnitude along B_{max} and B_{int} will also be slightly lower if compared to the case in Figure 5.10(a). Nevertheless, hodograms for either case of flux rope crossing would still exhibit a "potato chip" shape. Note that VEX is assumed to cross very close to the centre of the flux rope in the illustration in Figure 5.10(c) and (d), where the B_{min} is depicted in the direction quasi-along the VEX trajectory.

Based on this unique "potato chip" shape hodogram as a key identifier, a total of 132 magnetic flux ropes resulting in 264 dip-to-peak and peak-to-dip field changes are identified in this statistical analysis.

This identification methodology of flux ropes based on their unique "potato chip" shape hodogram is not necessary definitive. It could lead to misclassification in some cases. Since only the hodograms which clearly show a field rotation are selected, the likely case would be that some of the less definitive flux ropes are not included in this section. The analysis results for the rest of the selected flux ropes should still hold.

5.6.1 Locations

Similar to the locations of the boundary wave events, the flux ropes are observed in a small range of locations around the northern polar region with elevation $> 48°$, (90% of the observations made $> 60°$) as shown in Figure 5.12. The mean average altitude is 313 ± 11 km. It ranges from around 167 km to 860 km, with 90% of the passes made below 520 km. These flux ropes are observed everywhere in this small range of locations and do not show any particular preferred location.

5.6.2 Shape

Previously it was illustrated in Figure 5.10 that, for a spacecraft to cross the exact centre of an ideally circular flux rope, the magnetic field magnitude along B_{min} should be zero. And for the case where the flux rope is not crossed through its centre, there should be a finite non zero magnetic field magnitude along B_{min}. To measure the

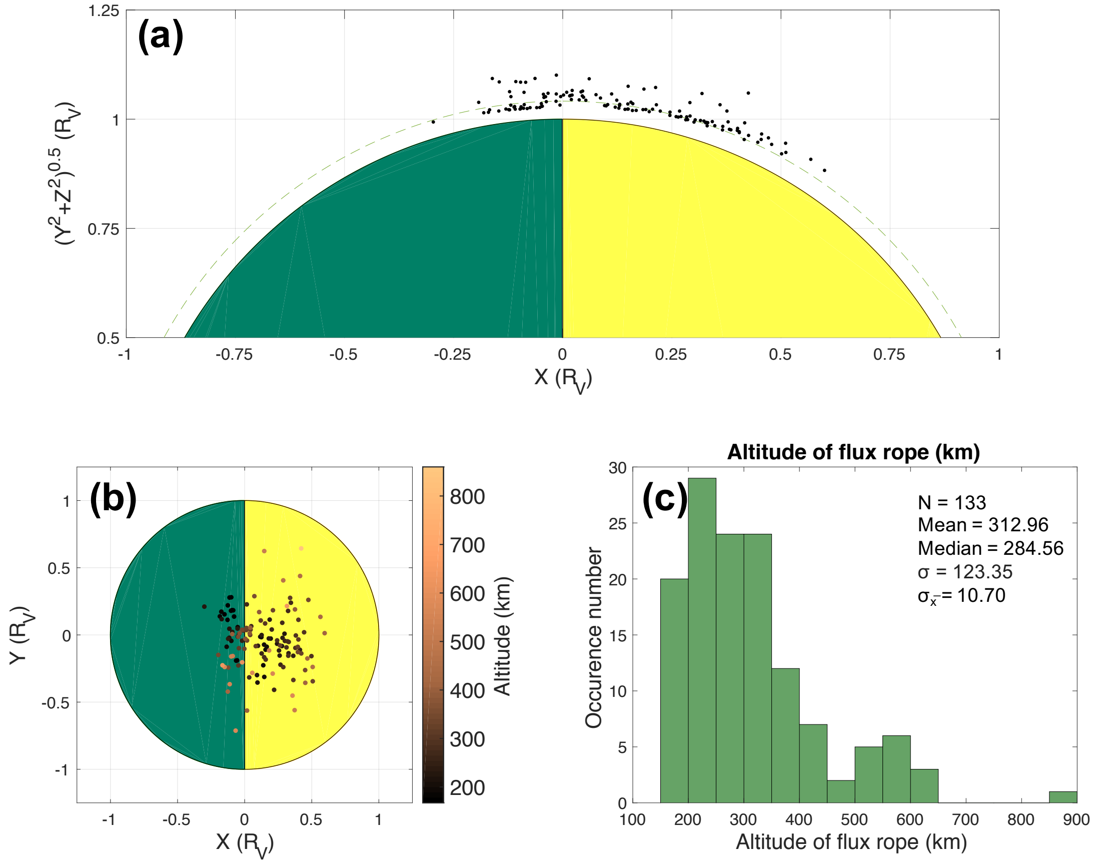

Figure 5.12: (a) The locations of the flux ropes are represented in black dots. They are plotted in a plane where the X-axis is along the X_{VSO} axis and the Y-axis is expressed in $\sqrt{Y^2 + Z^2}$. The nominal altitude of ionopause is represented in green dashed line [*Zhang et al.*, 2008a]. (b) The locations of the flux ropes are represented in coloured dots in the X-Y $_{VSO}$ plane. Units are in R_V. The altitudes of the flux ropes are indicated by the colour scale on the right. (c) A histogram of the altitude of the flux ropes crossings from a total of 133 events. Bin size is 50 km. Range: from 167 km to 860 km. The lower 0.25 and higher 0.75 quantiles are 225 km and 351 km respectively.

significance of the field magnitude along B_{min}, the $|B_{min}|/|B|$ value of all the flux ropes are calculated, where $|B|$ is the total magnetic field magnitude over the flux rope crossing. The mean average value of $|B_{min}|/|B|$ for all the 133 flux ropes is only 0.12 ± 0.01. This indicates that all of the flux ropes observed were crossed at or very close to its centre.

If the shapes of these flux ropes are ideally circular as depicted in Figure 5.10, for a spacecraft to cross its very centre, then the normal directions of the boundary crossings would be parallel/anti-parallel to the VEX trajectory. However, this is not reflected from the results. In fact, the mean average angle between the normal directions of the boundary crossings and the VEX trajectory is $47^\circ \pm 1^\circ$. This result indicates that the observed flux ropes in this study do not appear to be ideally circular as depicted. On the other hand, the finite values of the angle could also imply that the spacecraft crossed into the flux ropes with finite axial components, i.e. not perpendicularly. Similar to the boundary wave events, estimations of the exact shape are not possible based on the limitations of VEX.

5.6.3 Orientation

Similar to Figure 5.3(b), all the well defined minimum variance directions of only the flux rope crossings (a total of 177 that are well defined and have data points ≥ 6 and the photoelectron dropout events excluding flux ropes, are binned in a three dimensional polar histogram with an azimuthal ϕ bin size of 7.5° and elevation α bin size of 3.75° in Figure 5.11(c) and Figure 5.11(d) respectively. Compared to the non flux rope cases in Figure 5.11(d), the boundary normal directions of the flux ropes in Figure 5.11(c) are slightly more randomly orientated. However, the majority of them can still be observed to lie along the Y_{VSO} axis.

Next the flux ropes axial orientations (e.g. yellow coloured arrow B_{axis} in Figure 2.5) are assessed. Figure 5.10 illustrates how the radial, azimuthal and axial magnetic field components can be represented using B_{min}, B_{int} and B_{max} from MV analysis. And the B_{max} of a flux rope crossing can be used to approximate its axial orientation. Note that this approximation is only accurate if the spacecraft passes through/near the centre of the flux rope, which has been shown to be the case based on the low $|B_{min}|/|B|$ for all the flux rope crossings. To assess the flux ropes axial orientations correctly, only the B_{max} when the value of $|B_{min}|/|B| < 0.1$ are selected. This criterion yields a total of 74 B_{max} of the flux ropes (referred to as the “axial vector” from here on) for further analysis. In addition, individual magnetic field components along the X_{VSO}, Y_{VSO} and Z_{VSO} axes are also collected when the overall field magnitude of a flux rope crossing reaches its maxima (indicating reaching the centre of a flux rope). These individual magnetic field components are found to be consistent with the B_{max} direction which

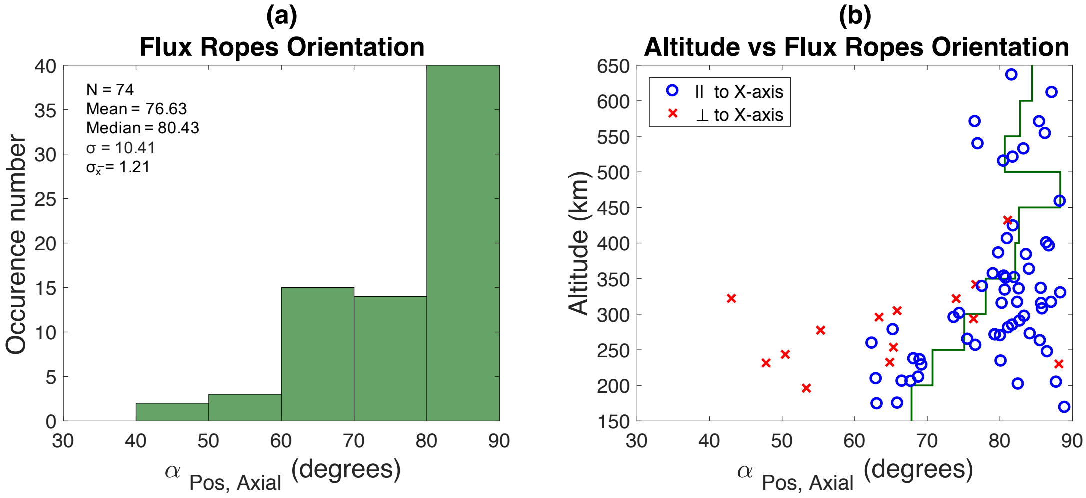

Figure 5.13: (a) A histogram of the $\alpha_{\ Pos,\ Axial}$ from a total of 74 flux ropes. Bin size is 10°. Range: from 43° to 89°. $\alpha_{\ Pos,\ Axial}$ is defined as the angle between the flux rope axial vector and the radial vector of the centre of Venus. (b) A scatter plot of the altitudes of the flux ropes against the $\alpha_{\ Pos,\ Axial}$. The green line is the mean average value of $\alpha_{\ Pos,\ Axial}$ for each 50 km bin. Blue circles and red crosses denote quasi-parallel and quasi-perpendicular orientations between the flux rope axial vector and the X_{VSO} axis.

further implies that the estimated axial vectors are well defined and accurate.

To examine if these axial vectors are quasi-horizontal or quasi-vertical with respect to the Venusian surface, all the $\alpha_{\ Pos,\ Axial}$, angle between the axial vectors and their respective radial vectors from the centre of Venus are calculated. A histogram of the $\alpha_{\ Pos,\ Axial}$ is presented in Figure 5.13(a). The mean average value of $\alpha_{\ Pos,\ Axial}$ is $77 \pm 1°$, which suggest that the majority of the flux rope axial orientations are highly quasi-horizontal to the Venusian surface. In fact, only 1 out of 74 flux ropes has $\alpha_{\ Pos,\ Axial} < 45°$ at 43° and 90% of the $\alpha_{\ Pos,\ Axial} > 63°$. A scatter plot of the altitudes of the flux ropes against the $\alpha_{\ Pos,\ Axial}$ is presented in Figure 5.13(b). It can be observed that the flux rope axial vectors are ‘highly’ quasi-horizontal to the Venusian surface for altitude >350 km. On the other hand, the flux rope axial vectors for altitude <350 km are slightly randomly oriented but still within the quasi-horizontal orientation regime.

These results reflect a similar trend to those reported in *Chen et al.* [2017] and *Elphic and Russell* [1983]. Note that the flux ropes in both work are analysed using VEX and PVO data respectively but are selected only based on the bipolar magnetic field signature (e.g. "potato chip" shape hodogram), while the flux ropes in this work are selected based on both the photoelectron dropout and the bipolar magnetic field signature events. Analysis in both studies show that the majority of the flux ropes around the terminator region have quasi-horizontal axial orientation at higher altitudes and randomly oriented at lower altitudes. However, one should note that in both studies, flux ropes with quasi-vertical orientation ($\alpha_{\ Pos,\ Axial} \approx 0°$) were also present at higher altitudes, while ∼99% (73 out of 74) of the identified flux ropes in this study have quasi-horizontal orientations $\alpha_{\ Pos,\ Axial} > 45°$. Only one flux rope has $\alpha_{\ Pos,\ Axial} < 45°$ at 43°.

Furthermore, all the $\alpha_{\ Xaxis,\ Axial}$, angle between the axial vectors and the X_{VSO} axis are calculated. The axial vectors are considered to be quasi-parallel to the X_{VSO} axis if $\alpha_{\ Xaxis,\ Axial} < 45°$ and to be quasi-perpendicular to the X_{VSO} axis if $\alpha_{\ Xaxis,\ Axial} > 45°$. These two classifications are further characterised in the scatter plot in Figure 5.13(b): the blue circles and red crosses denote quasi-parallel and quasi-perpendicular orientations between the flux rope axial vector and the X_{VSO} axis. Results show that the mean average value of $\alpha_{\ Xaxis,\ Axial}$ is $31 \pm 2°$ indicating the majority of the flux rope axial vectors are quasi-parallel to the X_{VSO} axis. In fact, around 81% of the axial vectors (60 out of 74) have $\alpha_{\ Xaxis,\ Axial} < 45°$.

5.6.4 Size - Diameter

The diameter of a flux rope is estimated by the product of the VEX velocity and the time spent between the inbound and outbound flux rope crossings. This is similar to the estimation of boundary wave widths in previous Section 5.5 but without the consideration of the two criteria: $\alpha_{mv} < 30°$ or $> 150°$ and $\beta_{vex} < 45°$. This is because, as elaborated earlier, these criteria are only used to eliminate the crossings of boundary waves that are still in linear growth phase and the boundary crossings of the 'near-tips' of the waves. However, for a flux rope crossing, both of these scenario are already shown to have been met: selection of flux ropes are based on (1) the three dimensional "potato chip" shape hodogram and (2) low mean average value of

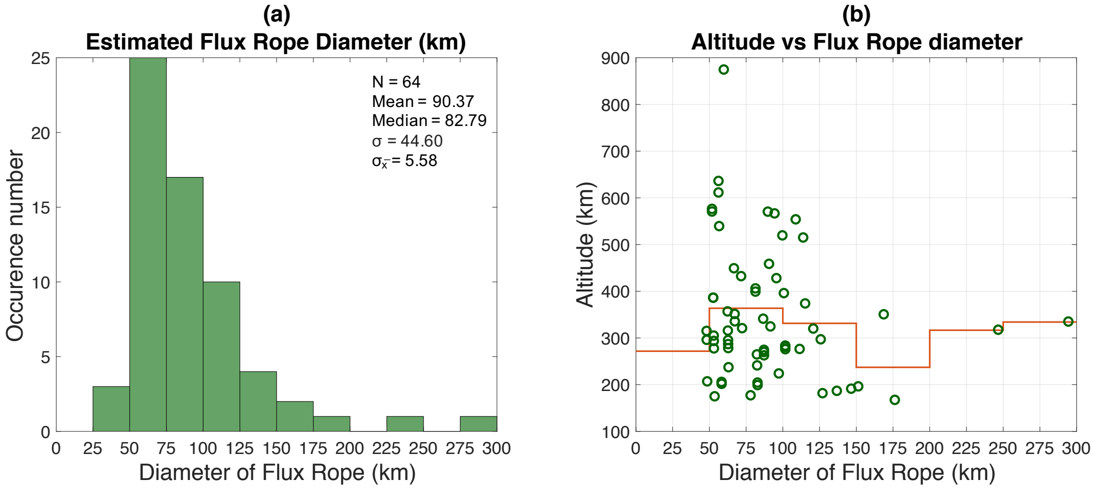

Figure 5.14: (a) A histogram of the estimated flux rope diameters from a total of 64 events from 2006 to 2014. Bin size is 25 km. Range: from 48.4 km to 294.7 km. (b) A scatter plot of the altitudes of the observed flux ropes against its estimated diameters, λ. Red line is the mean average value of altitude for each 25 km λ bin.

$|B_{min}|/|B| \approx 0.12 \pm 0.01$. Hence the criteria based on the α_{mv} and β_{vex} components are not implemented here.

The estimated diameters of a total of 64 (out of 133) flux ropes which have $\lambda_{int}/\lambda_{min} \geq 3$ and number of data points ≥ 6 are presented in a histogram in Figure 5.14(a) with a bin size of 25 km. The distribution of the flux rope diameters is also a single peak positively skewed distribution with a median value of 83 km and a mode class of 50-75 km. It ranges from 48 km to 295 km and has a mean average diameter of 90 ± 6 km. The lower 0.25 and higher 0.75 quantiles are 59 km and 102 km respectively. Additional analysis conducted with criterion $\beta_{vex} < 45°$ yields a total of 25 flux ropes and a mean average diameter of of 79 ± 6 km. The low value of $|B_{min}|/|B|$ and the consistency shown in the estimated diameters regardless if the criterion on β_{vex} is applied, implies that the majority of the flux ropes are crossed close to the centre and they do not appear to be ideally circular as depicted in Figure 5.5, consistent with the results in Section 5.6.2.

A scatter plot of the altitudes where the flux ropes are encountered, against their estimated diameters is presented in Figure 5.14(b). The red line is the mean average value of altitude for each 50 km λ bin. Similar to the cases of boundary waves. The results show that the mean average flux rope diameter is rather consistent at all altitudes and no dependence is reflected.

Note that the flux rope diameters are estimated on the assumption that the spacecraft (VEX has velocity ~9.5 km s^{-1} around the periapsis) crosses into stationary flux ropes. This assumption could add uncertainties to the results which may lead to some of the slightly scattered values of larger flux rope diameters (e.g. $>$ 200 km).

5.6.5 Production of flux ropes

The consistency shown between the results in Section 5.5 and this section suggests that these surveyed flux ropes are likely created as a result of turbulent boundary wave. An illustration adapted from *Wolff et al.* [1980] is depicted in Figure 5.15. The ionopause is a current sheet layer separating the ionospheric and shocked solar wind plasma. As shown in Section 5.5, the ionospheric boundary can at times exist in a wavelike appearance. As the boundary wave grows, the stability of the ionopause is continuously being distorted. When it reaches the turbulent state, boundary wave can break off and detach from the main wave. These broken wave, which are the compressed shocked solar wind magnetic field lines now bounded by the ionospheric current sheet in the ionosphere, are the flux ropes.

This mechanism is reflected by a number of results presented in this section. First of all, the flux ropes and boundary wave events are observed in a similar range of locations. The lower 0.25 and higher 0.75 quantiles for both flux ropes and boundary wave events are ~250 km and ~350 km respectively. Secondly, the estimated flux rope diameters (lower 0.25 and higher 0.75 quantiles of 59 km and 102 km) are roughly $\lambda/2$, half of the estimated boundary wave widths (lower 0.25 and higher 0.75 quantiles of 135 km and 255 km). In addition, the normal directions of the boundary crossings for both flux ropes and boundary waves are similar; i.e. the majority of them lie along the Y-Z $_{VSO}$ plane and predominantly along the Y_{VSO} axis. These consistencies shown between the flux ropes and boundary wave events indicates that the observed flux ropes are ‘newly’ created at the ionopause before sinking deeper into the ionosphere.

However, note that the flux rope diameters and the boundary wave widths are estimated

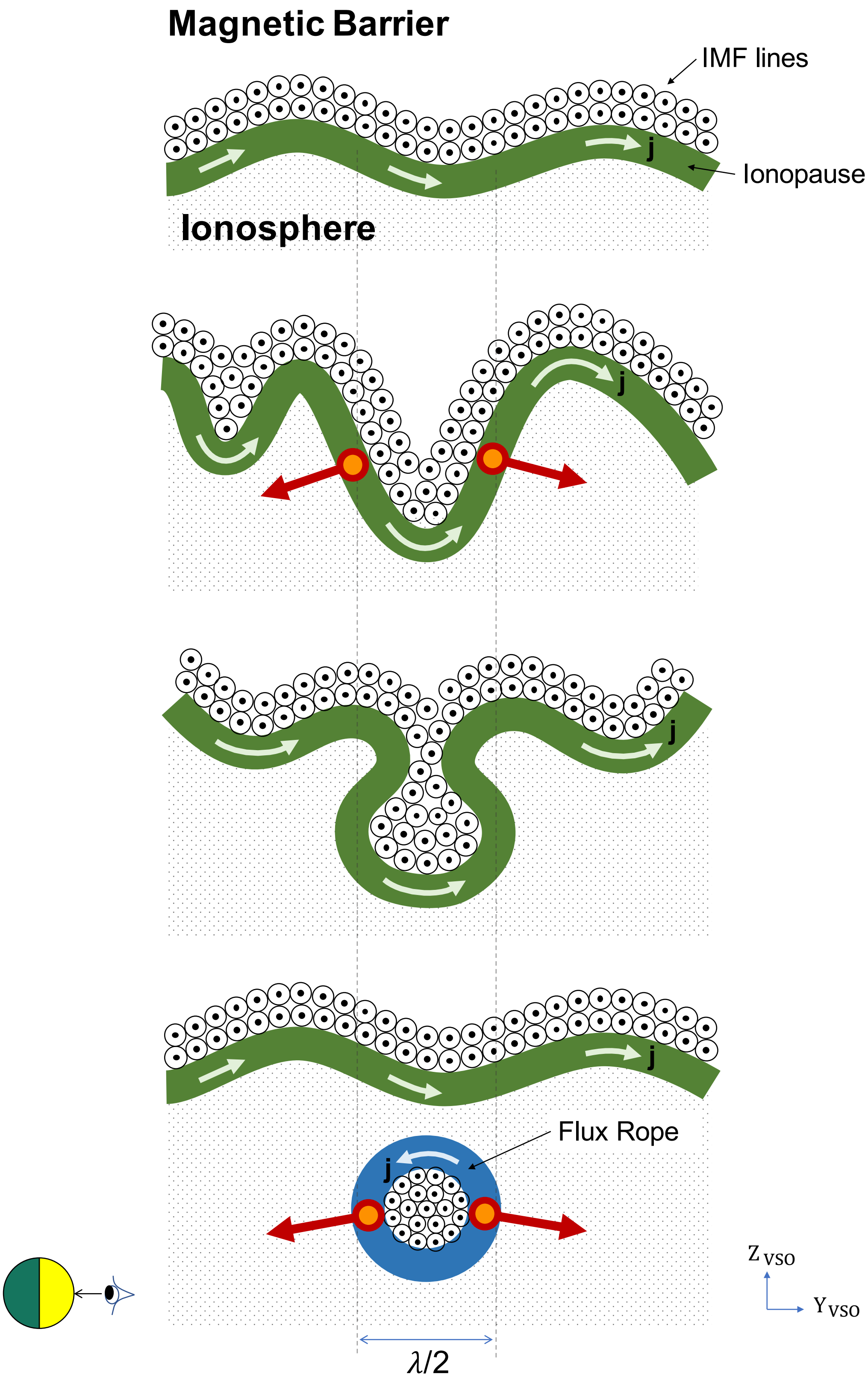

Figure 5.15: Illustration of how flux rope could be created as a result of turbulent boundary wave. The red arrows represent normal directions of boundary crossings projected from its local locations which are denoted by the orange coloured dots. λ denotes the boundary wave width. IMF lines are pointing out of the paper in this illustration. Adapted from *Wolff et al.* [1980]. **j** denotes the ionospheric current.

regardless of the impact angles (angle between the flux rope/boundary wave axis and the spacecraft trajectory). Therefore, to account for the additional distance the spacecraft travelled due to these impact angles, the estimated diameter and width presented here are expected to be smaller in the same magnitude. In other words, the estimated flux rope diameters will still be roughly half-wavelength of the boundary wave width and the theory illustrated in Figure 5.15 will still hold.

On the other hand, all the flux ropes are observed on the basis of the absence of photoelectron populations. This rules out the possible flux rope generation mechanism by mass loading. As summarised in Chapter 2, the mechanism presented in [*Russell*, 1990; *Wei et al.*, 2010] remarks the sinking of flux tubes into the ionosphere is based on the balance between the downward curvature force and upward buoyancy force (due to the different densities between the flux tubes and the ionosphere). When the buoyancy force is stronger than the curvature force, the flux tubes will float on the ionospheric current sheet. These flux tube can become heavier as a result of photoionisation process with the neutrals, eventually overcoming the buoyancy force and subsequently sink into the ionosphere. Hence, the flux ropes created from this case scenario will have bundles of flux tubes with electron populations similar to those of photoelectron. However, this is not the case reflected here, as photoelectron populations are absent in all the flux ropes analysed in this work.

It is also noteworthy to mention that the flux ropes created by the turbulent boundary wave are also subjected to photoionisation process as they sink into the ionosphere. This implies that, regardless of the production mechanism by either turbulent boundary wave or mass loading, the flux ropes observed in lower altitudes will have the signatures of photoelectron populations. Hence the absence of photoelectron population further suggests that all the flux ropes studied here are newly created by the turbulent boundary wave. The downward force of these newly created flux ropes can be smaller than the buoyancy force when they are first created by the turbulent boundary. So before these flux ropes can overcome the buoyancy force via photoionisation process, the possibility of flux ropes floating toward and reconnecting with the ionospheric boundary should not be ruled out. In addition, the mass loading mechanism is more favourable at the subsolar region where the velocity shear is the lowest, compared to the terminator region where the flux tubes will have been carried downstream by the incoming solar wind before they can get photoionised and sink into the ionosphere. On a similar note, this strong tangential shear flow in the terminator region may give rise to KHI which can lead to the formation of boundary wave. The generation mechanisms of boundary wave (thus flux ropes) will be discussed further in details in the Chapter 6.

The results in Section 5.6.3 found that the majority of the flux ropes are quasi-horizontal to the Venusian surface; highly horizontal for altitude >350 km and slightly randomly oriented for altitude <350 km but still within the quasi-horizontal orientation regime. A trend that is consistent to *Elphic and Russell* [1983] and *Chen et al.* [2017]. *Chen et al.* [2017] addresses that such orientation preference may indicate different flux rope formation mechanisms, but neither discussed their possible origins. If these flux ropes are created as a result of turbulent boundary wave as suggested in Figure 5.15, then for a boundary wave to ripple along the Y_{VSO} axis, the resulting flux ropes would have axial vectors quasi-parallel to the X_{VSO} axis, a scenario which is reflected from the results of $\alpha_{\ Xaxis,\ Axial} < 45°$. Due to the high latitude polar orbital nature of VEX, the flux ropes are only sampled in the northern polar region, hence it is not possible to compare to those in the subsolar region which are more frequently observed over the PVO mission. It is however, noteworthy to remark that *Elphic and Russell* [1983], which reports the flux rope in the terminator region are almost exclusively horizontal compared to those observed in the subsolar region which are randomly orientated. Hence, these observed flux ropes which are quasi-horizontal to the Venusian surface especially in the terminator region, are likely the newly created flux ropes originated from the turbulent boundary wave in the terminator region, rather than the subsolar region which the velocity shear would be low. They subsequently sink, twist and lose their horizontal axial vectors as they travel towards the atmosphere.

As the flux ropes sink deeper into the ionosphere, the velocity shear provided by both the turbulent boundary wave and the ionospheric plasma could provide the flux ropes its helical structure [*Russell and Elphic*, 1979]. These flux ropes will twist and compress as they travel deeper into the ionosphere, resulting in a decrease in their diameters, which can be attributed to the Helical Kink Instability [*Russell*, 1990]. The presence of velocity shear can also explain the rather irregular flux rope shapes (contrary to an ideal circular shape) observed in this work. Regardless of their overall irregular shapes, the flux rope helical structures and strong axial field are identifiable from their bipolar field magnitude signature. Note that the estimated flux rope diameters (mean average diameter of 90 ± 6 km) are significantly higher than the upper boundary of those reported in *Elphic and Russell* [1983] using PVO data (15-16 km in the terminator region) and *Chen et al.* [2017] using VEX data ($\sim$ 25 km in the terminator region). One explanation for this is that the flux ropes selected in this study are ‘newly’ created, implying bigger diameters compared to those which have travelled deeper into the ionosphere and become more twisted.

5.6.6 Implications

Based on the higher number of flux ropes found at lower altitudes, *Russell and Elphic* [1979] suggests that these flux ropes may enter into, slow down and ‘pile up’ in the denser ionosphere. The authors also propose a magnetic diffusion process on the time scale of many hours, which will allow them to be transported from the dayside to nightside and from high altitude to low altitude. As they twist and develop into three dimensional structures, they can interact with other flux ropes which have also become kink unstable to form more complex structures [*Russell*, 1990]. This can explain the rather randomly orientated flux ropes at lower altitude reported in *Elphic and Russell* [1983]. These flux ropes may dissipate their respective magnetic flux through charge exchange and recombination with the surrounding ionosphere, which is becoming more resistive as the altitude decreases [*Russell*, 1990]. Furthermore, *Russell and Elphic* [1979] has also proposed a possible source of flux ropes to originate from the lower ionosphere and subsequently float upwards to the ionopause due to the dominating buoyancy. Though this mechanism might be more dominant at Mars where the flux ropes could be formed via the interaction with its remnant magnetic field [*Acuna et al.*, 1998].

Creation of flux ropes described by this suggested mechanism of turbulent boundary wave, particularly with an axial vector along the X_{VSO}, axis imply that the two ends of the flux ropes will be anchored just outside the ionopause, with one end in the dayside and one end in the night side. This model could provide an alternative explanation to the frequent observations of ionospheric holes, a common nightside feature at Venus [*Brace et al.*, 1982; *Marubashi et al.*, 1985]. Their characteristics include the depletion of plasma temperature, density and a strong axial magnetic field magnitude. These characteristics are also consistent to the interior structure of a newly created flux rope. One problem with this proposed mechanism is that the helical structure has not been reported and the radial dimensions of the ionospheric holes could extend to a few hundred kilometres.

The characteristics of all the studied flux ropes, which are selected based on the absence of photoelectron population and their bipolar magnetic field signature, suggest that they are created as a result of ionospheric boundary waves reaching their turbulent state. Atmospheric bubbles, on the other hand, are also expected to form in a similar fashion. Continuous scattering and the subsequent convection of atmospheric bubbles downstream and away from Venus over a prolonged period of time plays an important role in atmospheric loss from Venus. However, the convection of the atmospheric plasma out of the ionosphere and subsequently downstream with the main solar wind bulk flow can change their magnetisation state as well as their characteristic plasma energy signature. In addition, the magnetic barrier region, where atmospheric bubbles populate before they are convected downstream, is highly dynamic. These complications may result in the atmospheric bubbles not being accurately identified in this work.

5.7 Summary

Data from the IMA, ELS and MAG onboard the Venus Express spacecraft are utilised to conduct a statistical survey of the ionospheric boundary wave events from 2006 to 2014. Results reveal that the ionopause of Venus does not always appear to be smooth, but often exhibits a wavelike appearance. In addition to this, results from the minimum variance analysis of all the photoelectron dropout events further reveal that, in the northern polar region of Venus, the ionospheric boundary wave is propagating along the dawn-dusk (Y_{VSO}) direction with its amplitude growing along the Z_{VSO} direction. Comparisons between the rippled and smooth boundary wave events allow detailed analysis of the ionopause dynamics during solar minimum. The results show that the ionopause thickness has a clear dependence on altitude and external pressure. These are consistent with and complement the works by *Elphic et al.* [1981] which utilised PVO data that operated during solar maximum period.

Similar to the boundary wave events, magnetic flux ropes are also identified based on the absence of photoelectron populations in addition to their signature “potato chip” shape hodogram. A statistical analysis on these magnetic flux ropes reveals a close similarity in the sizes, observed locations and normal directions of boundary crossings to those of boundary waves. This suggests that the flux ropes are ‘newly’ created as a result of turbulent boundary waves before sinking deeper into the ionosphere. This then rules out the production mechanism by the mass loading process in the subsolar region and subsequent transportation to the nightside. This is then followed by a discussion on the role of boundary wave in the Venusian atmospheric removal process with the formations of the flux ropes as well as the atmospheric bubbles.

The ionopause in the terminator region, where all these boundary wave events are observed, is unstable to KHI as a result of the expected strong tangential solar wind flow over the ionopause [*Wolff et al.*, 1980; *Terada et al.*, 2002]. This shear flow is expected to lie along the X_{VSO} direction, i.e. the solar wind bulk flow direction. However, results in this chapter show that in the northern polar region of Venus, the boundary waves propagate mainly along the Y_{VSO} direction which is inconsistent to the expected shear flow direction. The next chapter will assess the different boundary wave generation mechanisms, in particular their propagation directions.

5.8 Contribution

This chapter has three principal novel contributions.

Firstly, using the entire VEX mission duration which mainly covers the solar minimum period, this chapter presents the first observational statistical analysis of the ionospheric boundary wave phenomena at Venus, and measures their global distributions and characteristics. The results have been accepted for publication in Journal of Geophysical Research: Space Physics:

Chong, G. S., S. A. Pope, S. N. Walker, R. A. Frahm, T. L, Zhang, and Y. Futaana (2018), A statistical study of ionospheric boundary wave formation at Venus. *Journal of Geophysical Research - Space Physics.* doi:10.1029/2018JA025644.

Secondly, this chapter also present the first statistical study of the ionopause dynamics over the solar minimum period using VEX data. The results complement the works by *Elphic et al.* [1981].

Finally, there have been a handful of studies on the ionospheric flux ropes at Venus. These studies mainly identified the flux ropes based on their unique bipolar magnetic field signatures as well as their "potato chip" shape hodograms, regardless of their origins; whether they are formed by mass loading [*Russell et al.*, 1982] or turbulent ionospheric boundary waves [*Wolff et al.*, 1980]. This chapter presents for the first time, a statistical study on the magnetic flux ropes which are created as a result of only boundary wave events. This study provides an explanation of a strong preference in the magnetic flux rope orientations with respect to their observed altitudes, which have been reported by a number of previous works [*Chen et al.*, 2017; *Russell*, 1990; *Elphic and Russell*, 1983]. These results will be drafted and will be submitted to the Journal of Geophysical Research: Space Physics.

Chapter 6

Boundary wave generation mechanisms

6.1 Introduction

In Chapter 5, a statistical survey of the ionopause reveals that the ionospheric boundary is often observed to exhibit a wavelike appearance. In particular, it is observed in around 23% of all the available VEX orbits. However, this statistic is expected to be higher as the the observation of a boundary wave event can be rather subjective, in the sense that it cannot be demonstrated for certain whether the ionopause always exhibits a wavelike appearance, and if the observation is dependent exclusively on the chances of spacecraft crossing them. It has also been discussed how a boundary wave can lead to the formation of magnetic flux ropes and atmospheric bubbles which may play a vital role in the atmospheric evolution at Venus. In the case that the ionopause is always in a waveform, then its role in the atmospheric evolution at Venus will become more significant and should not be overlooked. So it is an objective in this chapter to address the potential ionospheric boundary wave generation mechanisms, that in particular lead to a boundary wave to propagate mainly along the Y-Z $_{VSO}$ plane and predominantly in a direction along the Y_{VSO} axis.

The three main generation mechanisms that will be analysed in this chapter are the

(1) KHI, (2) fluctuations of ionopause altitude as well as (3) reverse in magnetic field orientations.

6.2 Kelvin-Helmholtz Instability

A number of simulation studies (e.g. *Terada et al.* [2002]; *Biernat et al.* [2007]) have shown that the ionopause is unstable to KHI, a macroinstability that is principally generated by the strong shear flow [*Chandrasekhar*, 1961]. So it is an aim to investigate the role of KHI further in this section.

6.2.1 Velocity shear profile

The velocity shear flow across the ionopause when boundary waves are observed, $|U_{iono} - U_{Mb}|$ is estimated in this section. U_{iono} and U_{Mb} are the average proton velocity in the ionosphere and magnetic barrier regions respectively. Due to the long IMA sampling time of 192s, to ensure there are at least two data points, only U_{iono} from orbits that VEX spent longer than 192s (and at least 2 data points) in the ionosphere are considered and U_{Mb} is estimated by taking an average proton velocity 5 minutes (and at least 2 data points) before crossing the dayside ionopause. VEX normally spent around 1 to 5 minutes in the dayside magnetic barrier which varies with trajectories of the spacecraft.

A histogram of the measured velocity shear of 158 events with a bin size of 25 km s^{-1} is presented in Figure 6.1(a). The distribution of the estimated velocity shear is a single peak positively skewed distribution with a median value of 87 km s^{-1} and a mode class of 25-75 km. The $|U_{iono} - U_{Mb}|$ ranges from 5 km s^{-1} to 341 km s^{-1} and has a mean average velocity of 104 ± 6 km s^{-1}.

Since the time spent by VEX in the magnetic barrier region is often short, much less than the long 192s sampling time of the IMA, the estimation of U_{Mb} by averaging the proton velocity 5 minutes before crossing the inbound ionopause, will often include the plasma populations in the sheath region. These have a much larger magnitude along

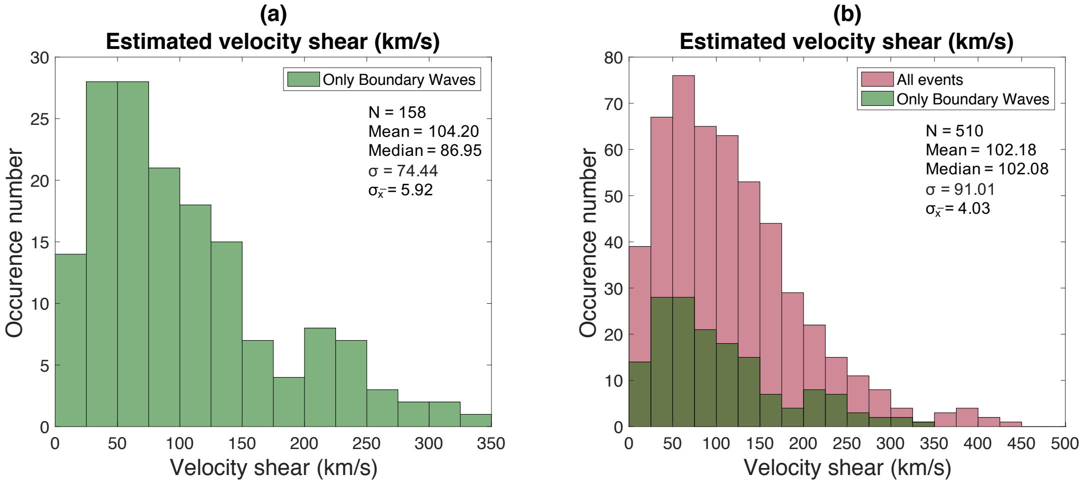

Figure 6.1: Histograms of the estimated velocity shear across the ionospheric boundary for (a) orbits when boundary waves are observed and (b) all orbits regardless if boundary wave is observed. Note that the velocity shear in (a) is overplotted in (b). (a) and (b) are computed from a total of 158 and 510 events respectively. Bin size is 25 km s^{-1}. Range for (a): from 5 km s^{-1} to 341 km s^{-1}. Range for (b): from 5 km s^{-1} to 444 km s^{-1}.

the X_{VSO} axis due to the main solar wind bulk flow. Therefore, the U_{Mb} presented here is an overestimate and shows bias along the X_{VSO} axis. The magnitude of the 'actual' U_{Mb} is expected to be lower. In addition, the estimation U_{iono} would also include the plasma velocity in the magnetic barrier region as a result of the boundary wave events. Hence, the velocity shear profile presented here should be examined with caution.

Further analysis has been conducted to estimate the velocity shear of all orbits regardless of whether boundary waves are observed. Figure 6.1(b) shows the histogram of the measured velocity shear of 510 events with a bin size of 25 km s^{-1}. The distribution of the estimated velocity shear is also a single peak positively skewed distribution with a median value of 102 km s^{-1} and a mode class of 50-75 km. The $|U_{iono} - U_{Mb}|$ ranges from 5 km s^{-1} to 444 km s^{-1} and has a mean average velocity of 102 ± 4 km s^{-1}. The histogram in Figure 6.1(a) is overplotted in Figure 6.1(b) for comparison. The results show that the ionospheric boundary does not always exhibit a wavelike appearance when the velocity shear is large (i.e. $|U_{iono} - U_{Mb}| > 150$ km s^{-1}). This can be due to: (1) stabilising terms (e.g. gravity [*Elphic and Ershkovich*, 1984]) which are more significant and dominate; (2) resolution of VEX data is too low to observe the short boundary wavelength resulting from the large velocity shear; and (3) the ionospheric

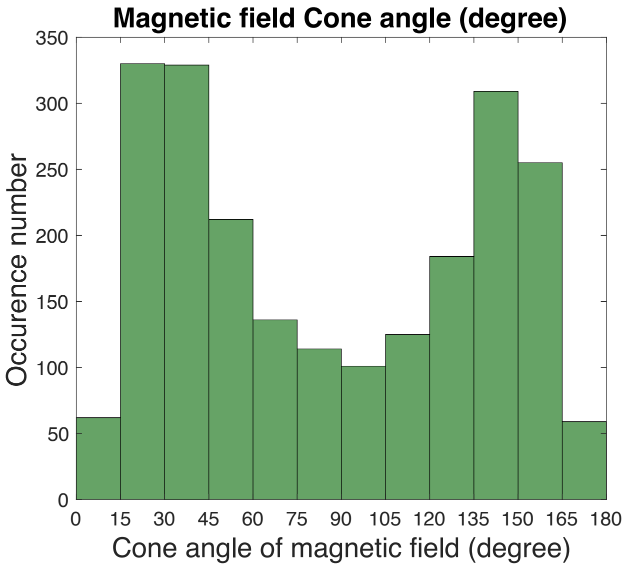

Figure 6.2: (d) A histogram of the magnetic field cone angle in the magnetic barrier region from a total of 2216 events. Bin size is 15°. Cone angle is defined as $\cos^{-1}(B_x/B)$.

boundary may exist in a wave but it is not traversed by VEX.

6.2.2 Orientation of magnetic field

Analysis reveals that the magnetic field orientation in the magnetic barrier region is quasi-perpendicular to the Y-Z $_{VSO}$ plane, which is a favourable condition for the excitation of KHI along the Y_{VSO} direction. This orientation is evidenced from the bimodal shaped distribution of the magnetic field cone angles in the magnetic barrier region presented in Figure 6.2, where the majority of the cone angles are $< 45°$ and $> 135°$, i.e. quasi-parallel to the X_{VSO} axis. Note that cone angle is defined as $\cos^{-1}(B_x/B)$. The distributions of the histogram are very consistent for all VEX passes regardless of whether boundary wave events are observed. This consistent quasi-parallel orientation of magnetic field lines to the X_{VSO} axis is due to the draping pattern of the magnetic field lines in the northern polar region of Venus. This is discussed further in the following sections.

6.2.3 Comparison to previous studies

The results of the estimated ionospheric boundary wave widths and the velocity shear flow across the ionospheric boundary are consistent with the study of KHI wave on Venus. For instance, *Wolff et al.* [1980] shows that with a 'gyroviscosity' coefficient, v_L of 250 km^2 s^{-1}, a velocity shear of 100 km s^{-1} results in a wavelength of $\sim$ 31 km while velocity shear of 10 km s^{-1} results in a wavelength of $\sim$ 305 km. For a typical 30 km thin ionopause, *Elphic and Ershkovich* [1984] shows that velocity shear of 100 km s^{-1} and 200 km s^{-1} results in wave growth times of 81s and 32s respectively. Considering a density jump (ionosphere to the sheath region) with a ratio of 10, the local MHD simulation by *Amerstorfer et al.* [2010] with the lower (30 km) and upper (70 km) limits of ionopause boundary thickness, gives a dominant KHI wavelength with a lower range limit of ~181 km and a higher range limit of ~423 km. Note that the density ratio between the ionosphere and the magnetic barrier cannot be accurately estimated from the VEX data as the spacecraft resolution is insufficient for such estimation. Similarly in *Ong and Roderick* [1972], for the most dominant mode of KHI, 30 km and 70 km of ionopause boundary thickness gives a dominant KHI wavelength of ~224 km and ~524 km respectively. The consistency shown between the estimated values in this statistical analysis and the simulation results, suggests that KHI may act as an excitation seed in inducing the ionospheric boundary wave that is observed in the northern polar region of Venus.

Note that the lower (30 km) and upper (70 km) limits of ionopause boundary thickness used here are obtained from the lower 0.25 and higher 0.75 quantiles of the estimated boundary thickness in Section 5.4.

6.2.4 Wave propagation along Y_{VSO}: Draping pattern of magnetic field

To assess if there is a preference in plasma velocity direction, the contribution of the mean average plasma velocity components along the X_{VSO}, Y_{VSO} and Z_{VSO} axes of the inbound solar wind (U_{sw}), magnetic barrier (U_{Mb}) and ionosphere (U_{iono}) are calculated and tabulated in Table 6.1. The contributions of plasma velocity components along

Table 6.1: A summary of the contributions of plasma velocity components along the X_{VSO}, Y_{VSO} and Z_{VSO} axes which are expressed in a percentage ratio of the individual components (medians of their individual distributions) with respect to the overall magnitudes of the inbound solar wind (U_{sw}), magnetic barrier (U_{Mb}) and ionosphere (U_{iono}). The U_{sw}, U_{Mb} and U_{iono} are averaged from a total of 658, 341 and 465 plasma velocity vectors respectively.

	Median (km s^{-1})			Contributions (%)		
Regions	X_{VSO}	Y_{VSO}	Z_{VSO}	X_{VSO}	Y_{VSO}	Z_{VSO}
Solar Wind	313.93	84.85	47.38	91.26	6.67	2.08
Magnetic Barrier	72.51	28.59	30.35	75.15	11.69	13.16
Ionosphere	15.44	26.88	24.88	15.10	45.73	39.17

the X_{VSO}, Y_{VSO} and Z_{VSO} axes are measured by taking the ratio of the individual components with respect to their overall magnitudes. The contributions are expressed in percentage and the median values of their respective distributions are utilised for this calculations.

Similar to the section above, only U_{iono} from orbits for which VEX spent longer than 192s in the ionosphere are considered, while U_{sw} and U_{Mb} are estimated by taking an average of proton velocity 30 minutes before crossing the inbound bow shock and 5 minutes before crossing the inbound ionopause respectively. To eliminate the possible orbital dependence of plasma velocity, only quasi-terminator VEX trajectories are considered, i.e. when the orbital plane is $< 30°$ to the terminator plane. It is also noteworthy to mention that the results (shown below) are consistent regardless of whether U_{sw} and U_{Mb} are estimated from only quasi-terminator or all VEX trajectories.

As shown in Table 6.1, the average solar wind plasma velocity outside of the bow shock is dominantly along the X_{VSO} axis, while the components along the Y_{VSO} and Z_{VSO} axes are minimal, as expected from the main solar wind bulk flow. However, through the bow shock and into the ionosphere, the contributions of the velocity component along the X_{VSO} axis can be observed to decrease drastically, while the contributions of the velocity components along the Y_{VSO} and Z_{VSO} axes become more significant. In the ionosphere, the plasma velocity is actually dominated by the components along the Y_{VSO} axis (with a contribution of $\approx 46\%$) followed by Z_{VSO} ($\approx 39\%$) and X_{VSO}

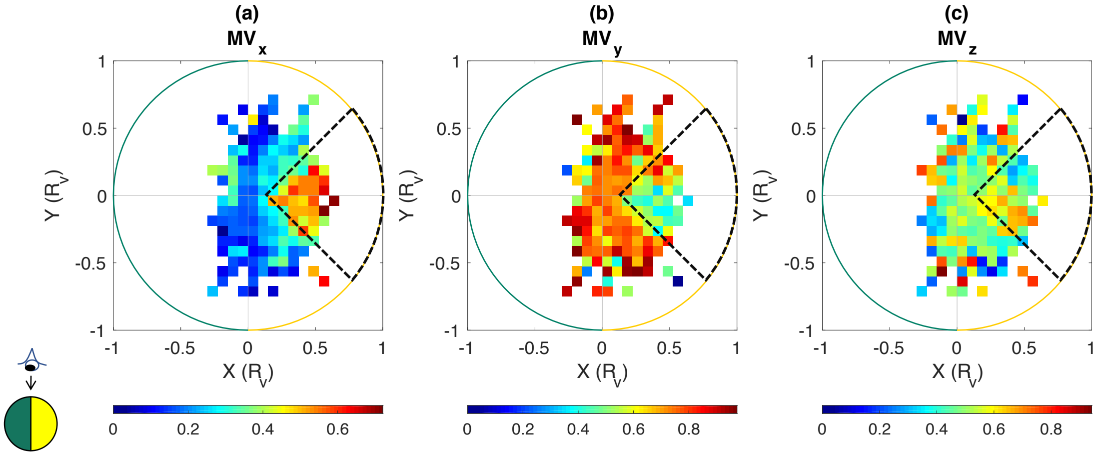

Figure 6.3: The distribution of MV_x, MV_y, and MV_z, which are the components of the normalized boundary normal directions along the X_{VSO}, Y_{VSO} and Z_{VSO} projected from their locations in the X-Y $_{VSO}$ plane. Each bin size is 0.075 R_v and they range from -1 R_v to 1 R_v. Regions outlined with the black-coloured dashed line are the regions where the azimuthal angle of the locations, $\phi_{Location} < |45°|$ which is just in front of X = 0.

($\approx$ 15%) axes.

The domination of the plasma velocity along the Y_{VSO} axis in the ionosphere region further suggests that a velocity shear profile across the ionospheric boundary could be set up and consequently exciting the boundary wave by KHI. However, the follow up question is: what is the possible driving mechanism of the plasma along the Y_{VSO} axis?

Dependence of the boundary normals with respect to their locations

Next the dependence of the normal directions of the boundary crossings with respect to their locations is studied. The MV_x, MV_y, and MV_z, which are the components of the normalised boundary normal directions along the X_{VSO}, Y_{VSO} and Z_{VSO} axes relative to the observation location of their associated boundary crossings in the X-Y$_{VSO}$ plane are shown in Figure 6.3. The measurement for each normal direction is binned in 0.075 × 0.075 R_v bins ranging from -1 R_v to 1 R_v. Only bins with two or more measurements are shown.

The results presented in Figure 6.3 shows a clear dependence of the boundary normal directions on their respective locations, especially when the azimuthal angle of the locations, $\phi_{Location} < |45°|$. These regions are outlined with the black-coloured dashed line which is just in front of X = 0. For instance, observable from Figure 6.3(a), the MV_x components in the region $\phi_{Location} < |45°|$ are much larger compared to the region $\phi_{Location} > |45°|$. This is visible by the stronger red-coloured patches in the region outlined with the black-coloured dashed line. In contrast, from Figure 6.3(b), the MV_y components in the same region are much smaller, visible from the weaker blue-coloured patches. While MV_z components are rather randomly distributed. Even though the majority of the boundary normal directions are dominantly along the Y_{VSO} axis, the above results suggest that, at the location $\phi_{Location} < |45°|$, the boundary normal directions have slightly larger components along the X_{VSO} axis.

6.2.5 Draping of magnetic field lines

In Figure 6.4(a), taking the normal directions of the boundary crossings (represented as purple arrows) across an altitude range from 360 km to 370 km as an example, the boundaries (represented as red-dotted lines which are perpendicular to the normal directions) show an alignment that is comparable to a typical pattern of draped magnetic field lines (represented as blue lines) around Venus. These curved patterns are also valid at other altitude ranges (illustrations not shown here). The results from Figure 6.4(a) are consistent to Figure 6.3. The expected overall draping configuration of magnetic field lines across the cross section of altitude is illustrated in Figure 6.4(b)-(c).

Upstream of the bow shock, the IMF may appear in a range of orientations. The IMF moves towards Venus in the direction of the main solar wind bulk flow ($-X_{VSO}$). As the magnetic field lines drape around Venus, their orientations can be visualised to change from quasi-straight lines (upstream of bow shock) to highly curved lines (outside of the ionopause in the polar regions of Venus) as illustrated in Figure 6.4(b) and (c). Typically, upstream of the bow shock, the solar wind has a higher plasma β (defined as the ratio of thermal to magnetic pressure). In this case, the thermal pressure dominates and the magnetic field lines are carried by the plasma flow. The plasma still gyrates around the field lines but has an overall velocity component mainly in the direction of

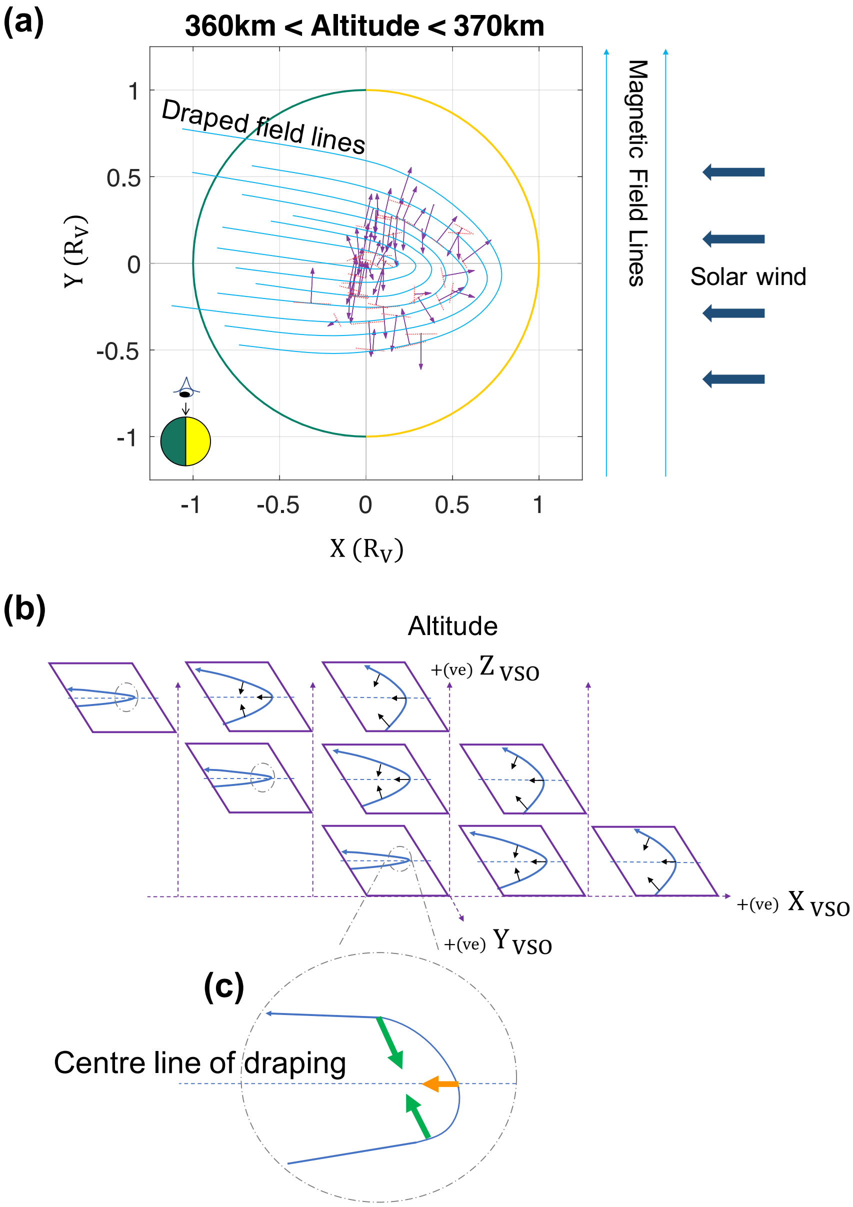

Figure 6.4: (a) An illustration of how all the perpendicular directions of boundary normal directions (from the altitude band 360 km < altitude < 370 km) could be related to field draping. The red dotted lines are the perpendicular directions to the boundary normal directions, the blue lines represent the expected draping pattern and the purple arrows are the minimum variance directions. Note the intended slight solar wind aberration due to the orbital motion of Venus. (b)-(c) Illustrates how the draping patterns of magnetic field lines may change as a function of altitude and along X_{VSO} direction (adapted from [*Chong et al.*, 2017]) The black arrows represent the normals to the field line directions as they drape around the planet. The orange arrow shows the downstream convection direction of draped field lines. Green arrows represent how the magnetic field lines might be tightly draped towards the centre line of draping (which is along the Y_{VSO} axis).

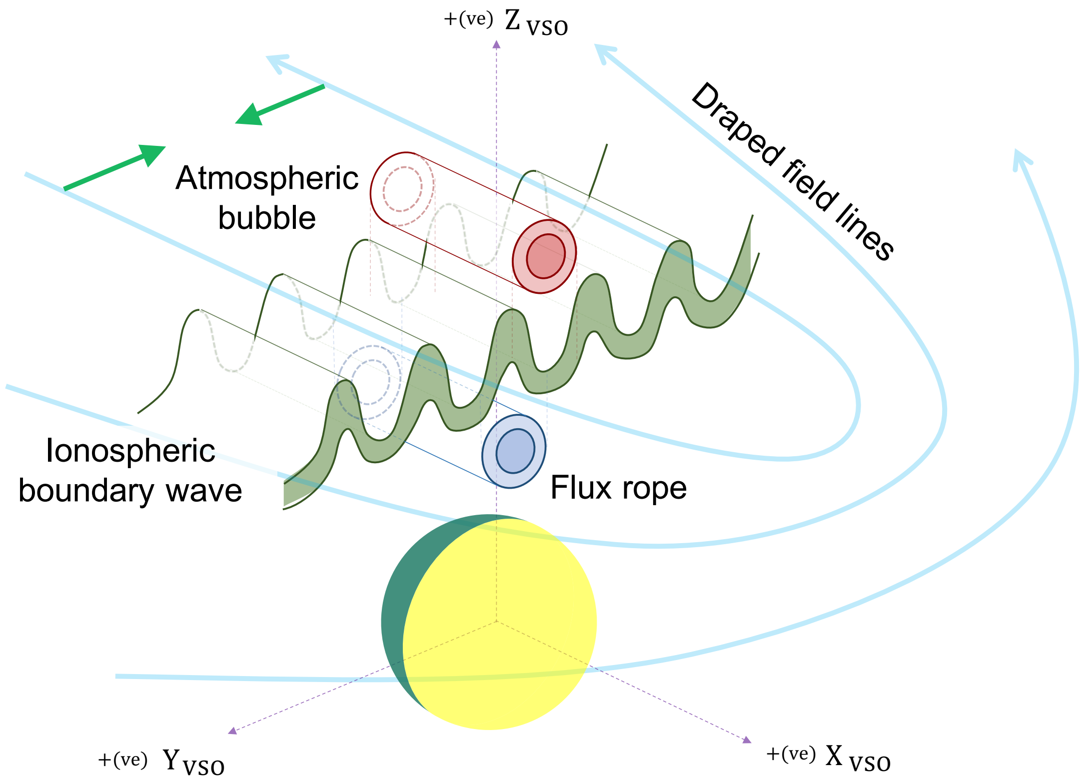

Figure 6.5: Illustration of how field draping might lead to ionospheric boundary wave and the production of flux rope and atmospheric bubble. Illustration is not drawn to scale.

solar wind bulk velocity in the $-X_{VSO}$ direction (represented by the orange arrow in Figure 6.4(c)). In contrast, through the magnetosheath the IMF lines start to pile up and drape around Venus more 'orderly and regularly', with the field lines eventually extending mainly in the direction of the solar wind bulk flow regardless of the IMF orientation [*McComas et al.*, 1986; *Masunaga et al.*, 2011; *Tanaka*, 1993]). At the same time, the plasma is slowly heated and slows towards the ionopause, where the thermal pressure is gradually converted into magnetic pressure. This consequently results in a lower β where the magnetic pressure dominates and the plasma is now "frozen into" the magnetic field lines. As a result, just outside of the Venusian ionopause around the polar regions, as illustrated by the green arrows in Figure 6.4(c), the now much lower β plasma is 'forced' to move towards the centre line of draping (which is along the Y_{VSO} axis) due to the movement of magnetic field lines (which is along the Y_{VSO} axis). This could subsequently set up a velocity shear along the Y_{VSO} axis. In addition, as the density jump is along the Z_{VSO} axis in the northern polar region, the combination together with the velocity shear along the Y_{VSO} axis and the quasi-parallel orientation of magnetic field lines to the X_{VSO} axis, should favour the growth of KHI induced ionospheric boundary waves along the Y-Z $_{VSO}$ plane and with a propagation direction along the Y_{VSO} axis.

This proposed mechanism is consistent with the results presented in this work and is illustrated in Figure 6.5. Note that the flux rope and the atmospheric bubble are only depicted simply to illustrate their possible presence. Their actual shapes are not known and the depicted circular shapes are for illustration purposes only.

Independence on the IMF orientation

For completeness, the dependence of the boundary wave events on the orientations of the IMF has also been assessed. To eliminate the effects when the IMF might have changed between the inbound and outbound bow shock, IMF data is only considered when the angle between the inbound and outbound IMF orientations are $< 15°$. The IMF clock[1] and cone[2] angles for all the VEX orbits, as well as the orbits when boundary wave events are observed are shown in polar histograms in Figure 6.6(a)-(d). Binsize is 30°.

The majority of the incoming IMF can be observed to have orientations mainly quasi-along the Y_{VSO} axis and quasi-perpendicular to the X_{VSO} axis. On the other hand, the IMF clock angles when boundary waves are observed (i.e. Figure 6.6(c)) are not as orderly orientated but are considerably similar to Figure 6.6(a). The distribution of IMF cone angles in Figure 6.6(d) is very similar to Figure 6.6(b). These results indicate that the occurrence of a boundary wave does not show any dependence on the IMF orientation. This lack of dependence on the IMF orientation is consistent to the suggested mechanism where, regardless of the IMF orientation, the magnetic field lines pile up more orderly and regularly in the magnetic barrier.

---

[1] Clock angle is defined as $\tan^{-1}(B_y/B_z)$.

[2] Cone angle is defined as $\cos^{-1}(B_x/B)$

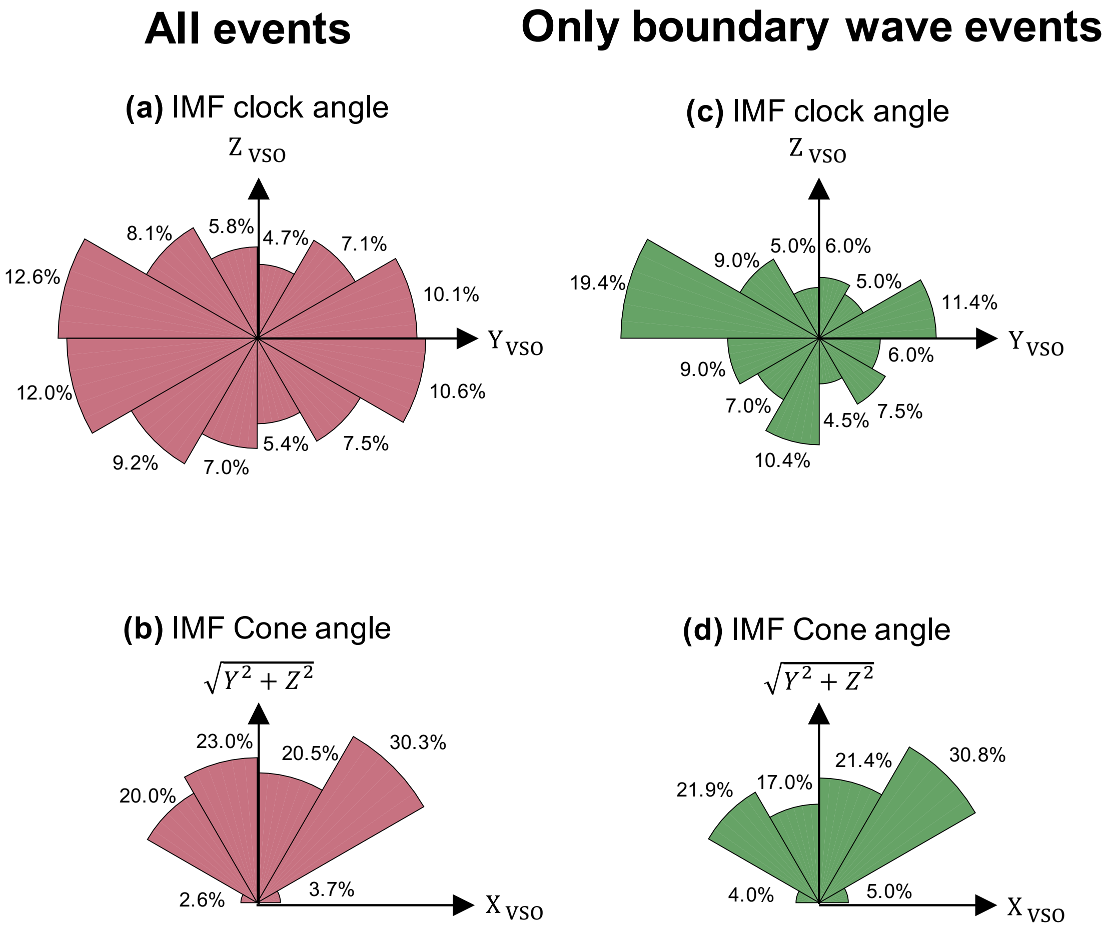

Figure 6.6: IMF (a) clock angle and (b) cone angle based on a total of 1091 orbits. IMF (c) clock angle and (d) cone angle based on a total of 201 orbits when boundary wave events are observed. Cone angle is defined as $\cos^{-1}(B_x/B)$. Clock angle is defined as $\tan^{-1}(B_y/B_z)$.

6.3 Fluctuations of ionopause altitude

By using PVO data, *Brace et al.* [1980] noticed that the observations of ionospheric boundary wave are always accompanied by fluctuations of ionopause altitude. Hence the occurrence of a boundary wave could be due to the variability in ionopause altitude and could subsequently lead to the detachments of atmospheric bubbles. So it is an interest in this section to investigate this scenario further.

The survey of VEX data from 2006 to 2014 has identified a total 2162 ionosphere perturbations based on the observations of the ionospheric photoelectron population. Each of these 2162 perturbations corresponds to an inbound and an outbound ionopause

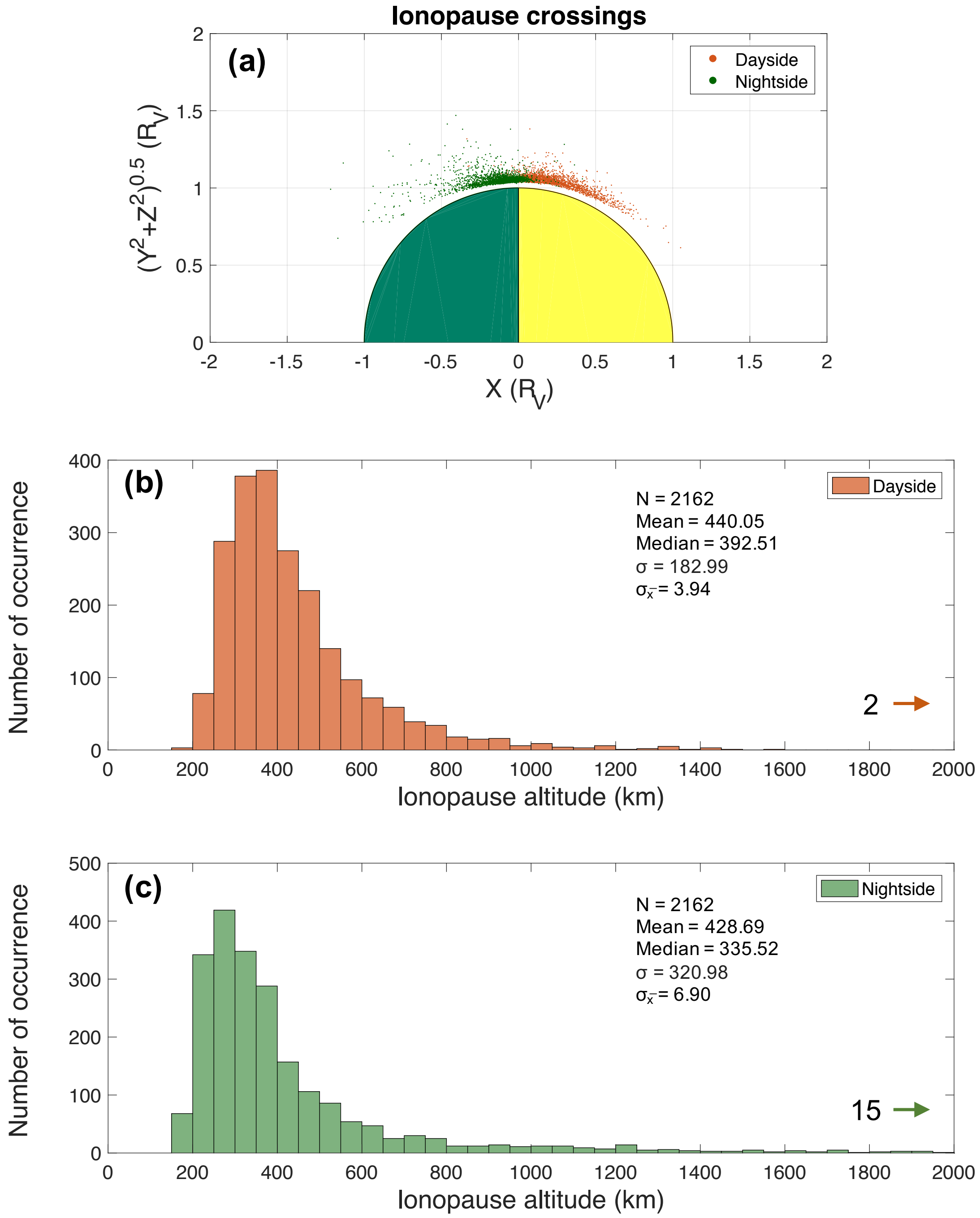

Figure 6.7: (a) Positions of the ionopause from 2006-2014. Red and green coloured dots represent dayside and nightside crossings respectively. They are plotted in a plane where the X-axis is along the X_{VSO} axis and the Y-axis is expressed in $\sqrt{Y^2 + Z^2}$. Histogram of the altitude of the (b) dayside and (c) nightside ionopause crossings. Range for (b): from 180.1 km to 2302.2 km. Range for (c): from 154.4 km to 3748.4 km. Both have bin size of 50 km. 2 dayside and 15 nightside ionopause crossings altitude greater than 2000 km not included on the histogram.

crossing. Here, the two ionopause crossings resulting from each of these VEX passes are further classified into dayside and nightside crossings, based on the regions where they are observed. For VEX passes which have orbital planes quasi-parallel to the terminator plane, the dayside (nightside) ionopause crossing is regarded as the crossing where its magnetic field magnitude in the magnetic barrier is higher (lower). The locations of these ionopause crossings are plotted in Figure 6.7(a), where the red and green coloured dots represent dayside and nightside crossings respectively. Histograms of the dayside and nightside ionopause crossings are presented in Figure 6.7(b) and (c) respectively.

These results complement the work by *Angsmann et al.* [2011] which covers the analysis of VEX data from 2006 to 2010 but their work did not consider the classifications of dayside and nightside crossings. The results presented in Figure 6.7 show that the ionopause altitude fluctuates considerably over the course of the VEX mission. The lowest and highest altitude of the combined dayside and nightside ionopause crossings are 154 km and 3748 km respectively. The dayside altitudes can also be observed to be more confined compared to the nightside where the altitudes are more spread out. This can also be reflected by the lower variance of 183 km and higher variance of 321 km for the respective dayside and nightside cases. This difference in the variance values can be attributed to the more complex pressure balance in the nightside where the manifestation of solar wind pressure to magnetic pressure is less straightforward compared to the dayside.

The fluctuations of ionopause altitude are measured by the difference between the altitudes of two consecutive orbits, i.e. subtraction of the altitude by the value of the orbit before. For example, positive (negative) values imply higher (lower) altitude in the previous orbit. As there are orbits where the ionosphere is not perturbed or the ELS data is unavailable, only 1929 VEX passes with consecutive ionosphere perturbations are selected for further analysis. The changes of inbound and outbound ionopause altitudes for cases when boundary wave events are not observed and are observed, are presented in histograms in Figure 6.8(a)-(d). The red and yellow lines represent the lower 0.25 and higher 0.75 quantiles respectively.

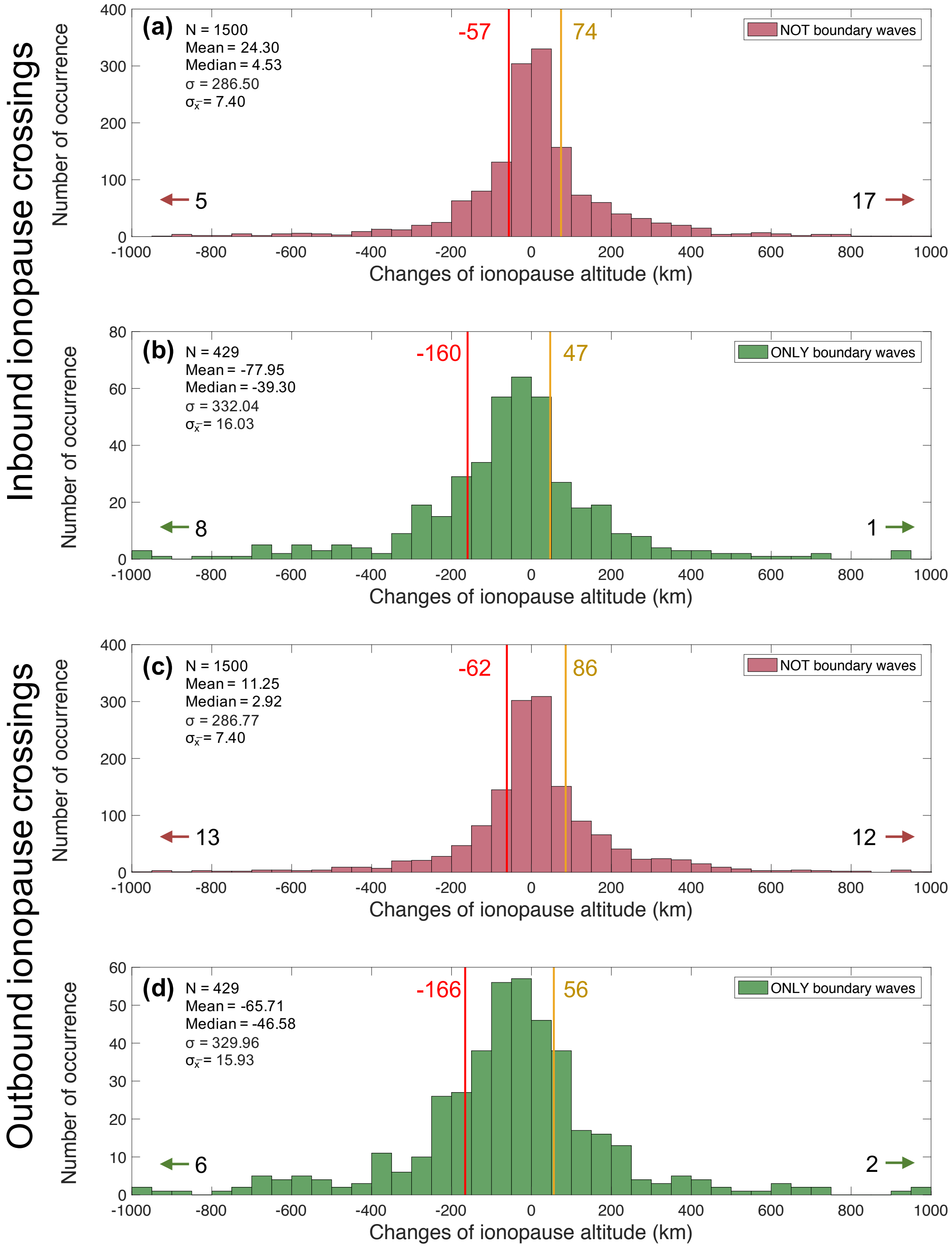

Figure 6.8: Histograms of the inbound ionopause altitude changes when boundary wave events (a) are not observed and (b) are observed. (c)-(d) are same as (a)-(b) but for outbound ionopause crossings. Bin size is 50 km for all histograms. Altitude changes are measured by the difference between the altitudes of two consecutive orbits. The red and yellow lines represent the lower 0.25 and higher 0.75 quantiles respectively. The number of altitude changes which are not included in these histograms are noted on the lower left and right corners of respective histograms.

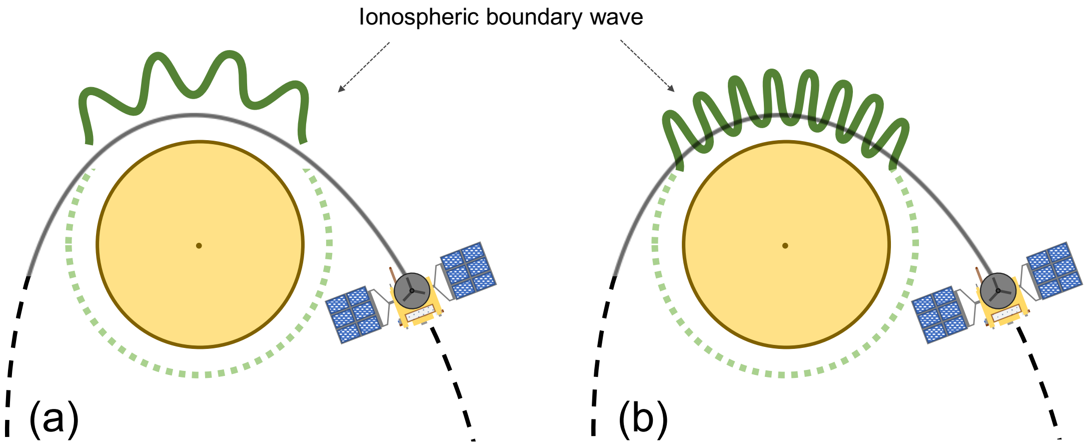

Figure 6.9: Possible scenarios where the ionospheric boundary waves cannot be observed by the spacecraft. (a) Boundary wave may exist in a wave but it is not traversed by VEX. (b) Boundary wave with short wavelength (in comparison to the resolution of VEX).

Both the lower 0.25 and higher 0.75 quantiles of the altitude changes for the cases when boundary wave events are observed (Figure 6.8(b) and (d)), are significantly lower than the cases when boundary wave events are not observed (Figure 6.8(a) and (c)). In fact, the median values of the altitude changes for both inbound and outbound crossings cases when boundary wave is not observed are ≈ 0 km. On the other hand, the median values are -39 km and -47 km for the cases when boundary wave events are observed. Although it should not be taken as a strong indication, the distinct difference in the lower 0.25 quantiles for cases whether boundary waves are observed, suggests that the fluctuation of ionopause altitude may be a factor for the occurrence of boundary wave. Furthermore, the results also indicate that the occurrence of boundary wave is more (less) likely when the ionopause altitude is higher (lower) compared to the altitude of orbits from previous days.

It is noteworthy to mention that boundary wave events are also observed for small altitude changes, i.e. $< |50 \text{ km}|$. Inversely, boundary wave events are not always observed for large altitude changes, i.e. $> |150 \text{ km}|$. However, similar to Section 6.2.1, the observation of the ionospheric boundary exhibiting a wavelike appearance can be subjective, in the sense that the ionospheric boundary may exist in a wave but it is not traversed by VEX, and the resolution of VEX data may be too low to observe a

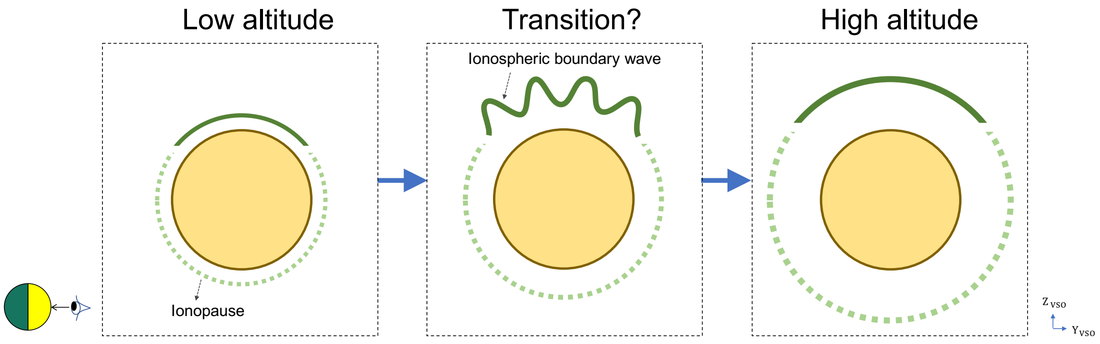

Figure 6.10: An illustration of how boundary wave could be formed as a result of fluctuations in ionopause altitude. Due to the highly elliptical polar orbit of VEX, only the ionopause in the northern polar region of Venus is perturbed by the spacecraft. Hence the ionopause not sampled by the VEX is illustrated with dotted line. Illustration is not drawn to scale.

boundary wave with short wavelength, as illustrated in Figure 6.9. On the other hand, significant disturbance of the ionopause boundary due to the waves may also result in crossings being observed at higher than expected altitudes. This scenario can also serve as an explanation to the slight bias shown from the occurrence of the boundary wave on the altitude fluctuations. Hence, the results presented above should be compared with cautions.

A possible scenario of boundary wave formation based on these results is illustrated in Figure 6.10. As previously discussed, the variability in solar wind pressure could lead to changes in ionopause altitude. If the solar wind is assumed to impact on Venus in the -X_{VSO} direction regardless of the solar wind aberration (due to the orbital motion of Venus), then a decrease in solar wind pressure will lead to an increase of ionopause altitude temporally. This temporal change of ionopause altitude may lead to the distortion of the ionopause and subsequently the formation of boundary wave in a similar fashion as depicted in Figure 6.10. This proposed model that considers the ionopause altitude fluctuation factor is highly speculative but does fit, quite effectively with the results presented in this section. However, it is unclear why the occurrence of the boundary wave is less likely when the ionopause altitude is lower than the altitude on the previous day.

As far as it could provide an interesting explanation that the altitude fluctuation may act as an initial seed excitation for the formation of boundary wave, this model can not address its particular propagation direction, which is mainly along the Y_{VSO} axis (as presented in Chapter 5.5). So Figure 6.10 should only serve as an illustration.

6.4 Reverse in magnetic field orientation

Based on the significant field behaviour change of the observed flux ropes within 15° of the terminator, using PVO data, the work of *Luhmann* [1990] suggested a series of "terminator waves" that has an east-to-west field oscillation along the terminator. The author suggested that the observations of the dayside ionospheric flux ropes can be resulted from these terminator waves. A schematic illustration of this terminator wave which is represented as a wavy ionospheric current sheet, is presented in Figure 6.11 (adapted from *Luhmann* [1990]). A reverse in the orientation of the penetrated magnetic field can result in layers of various magnetic field orientation. Any disturbances to the current sheet can subsequently lead to a wavelike appearance. The author then suggested that the field lines merging could result in the detachment and the dissipation of ionospheric flux tubes, as well as the production of ionospheric flux ropes.

It is an interest in the section to investigate if a reverse in magnetic field orientation might play a role in the occurrence of boundary waves. To do this, all the average magnetic field magnitude in both the inbound and outbound magnetic barrier are analysed. Unlike the nightside ionopause crossings which can be identified by the last

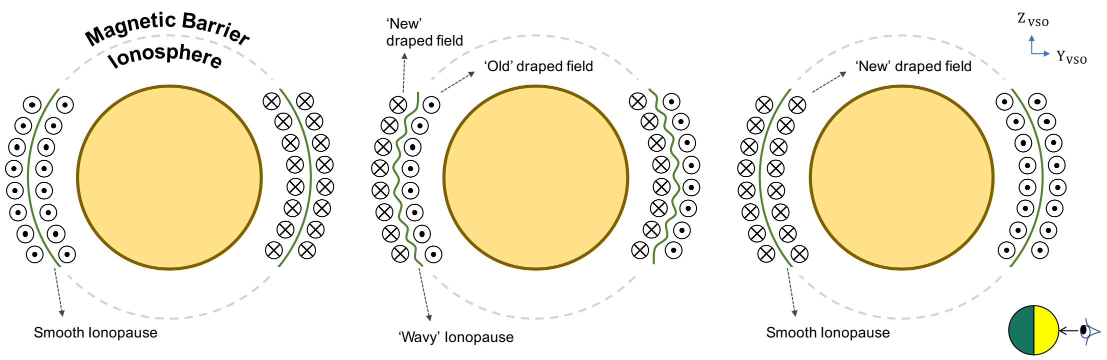

Figure 6.11: Schematic illustration how "wavy" ionopause could be formed as a result of reverse magnetic field orientation. Note that illustration not drawn to scale.

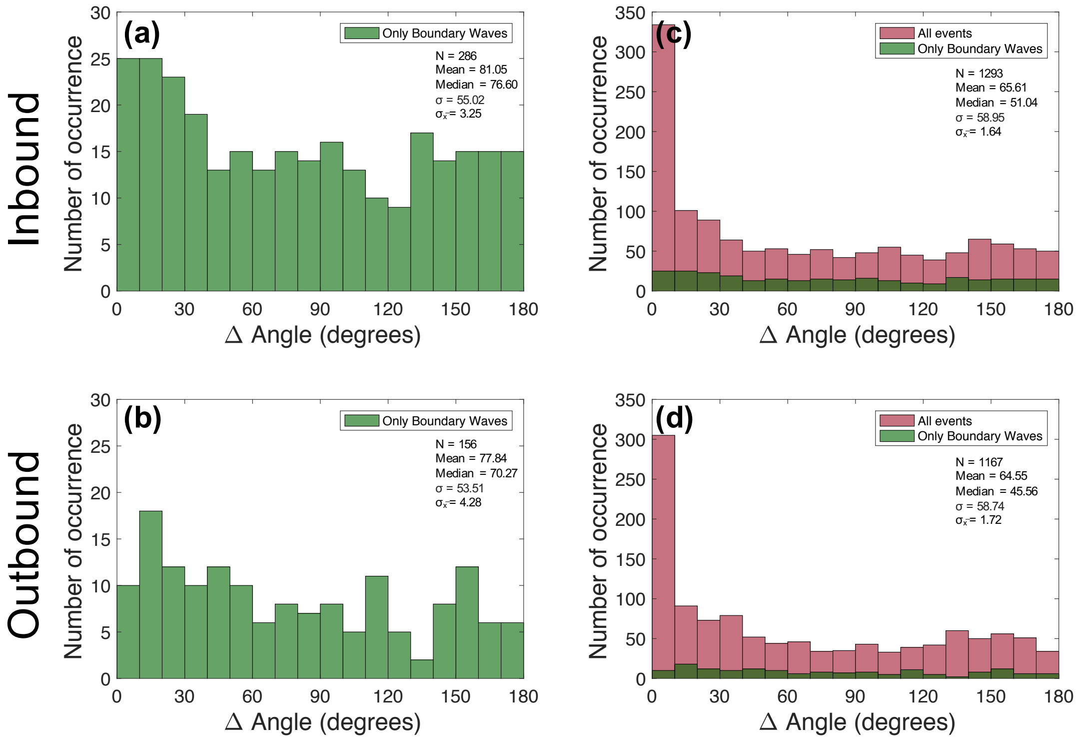

Figure 6.12: (a)-(d) Histograms of △Angle with bin size of 10°. (a)-(b) Histograms (green) of △Angle of both the inbound and outbound magnetic barrier for the cases when boundary waves are observed. (a)-(b) are overplotted in (c)-(d). (c)-(d) Histograms (green) of △Angle of both the inbound and outbound magnetic barrier regardless if boundary waves are observed.

observation of photoelectron population, the magnetic field in the magnetic barrier in the nightside region is often less well defined, so it will not be considered for the analysis in this section.

The 'reverse' of the magnetic field orientation is measured by the angle between the magnetic field magnitudes in the magnetic barrier of consecutive orbits (referred to as '△Angle' from here on). △Angle ranges from 0° to 180°, where 0°, 90° and 180° imply parallel, perpendicular and anti-parallel orientations between the consecutive magnetic field magnitudes respectively. Histograms of △Angle with bin size of 10° are presented in Figure 6.12(a)-(d). The green coloured histograms in Figure 6.12(a)-(b) represent the distributions of △Angle for the cases when boundary waves are observed. They are overplotted in Figure 6.12(c)-(d) where the red coloured histograms represent the △Angle distribution for all orbits regardless if boundary waves are observed.

The results show that the △Angle distribution in Figure 6.12(a)-(b) are somewhat evenly distributed across all angles with a slightly higher distribution in △Angle $< 60°$. In other words, boundary waves can be observed in all range of △Angle and show no obvious dependence on any particular △Angle. In addition, the comparison of the overplotted distributions in Figure 6.12(c)-(d) further reveals that the △Angle distributions regardless of whether boundary waves are observed, are fairly consistent. However, it is noteworthy to point out that the obvious peaks of $< 10°$ in Figure 6.12(c)-(d) indicate that the magnetic field orientations in the magnetic barrier of consecutive orbits in general do not vary frequently. Considering how infrequent the changes of magnetic field orientations in all orbits, the absence of such an obvious peak at $< 10°$ of the △Angle distribution in Figure 6.12(a)-(b) imply that the boundary waves are less frequently observed for a smaller value of △Angle. The results indicate that reversed magnetic field orientations may play a potential, but non-fundamental role in exciting a boundary wave.

On a side note, the infrequent changes of magnetic field orientations also suggests an 'orderly and regularly' piling up of magnetic field lines in the magnetic barrier region, which further agrees with the draping pattern of the magnetic field lines discussed in Section 6.2.5. VEX had a long orbital period of 24 hours which makes it challenging to assess this suggested model by *Luhmann* [1990]. The authors also acknowledged that this model is highly speculative.

6.5 Summary

This chapter has discussed three potential boundary wave generation mechanisms. They are the KHI, ionopause altitude fluctuation and reversed magnetic field orientations. Analyses of all three mechanisms suggest that they may play roles in boundary wave excitation but the indication strengths of respective mechanisms vary. It is not possible to compare their importances qualitatively as the role of each of these three proposed mechanisms is analysed with different approaches. However, it is noteworthy to mention that the fluctuations of ionopause altitude itself cannot explain why the majority of the normal directions of the boundary wave crossings have components mainly along the Y_{VSO} axis. Furthermore, neither the fluctuations of ionopause altitude nor the reverse in magnetic field orientation as boundary wave generation mechanisms could provide a tangible explanation on the growth of the boundary wave amplitude mainly along the Z_{VSO} directions, to an extent of reaching turbulent state and breaking off from the main wave.

On the other hand, the consistency shown between the results and those from simulation studies on KHI indicate that the ionospheric boundary waves develop due to the KHI. In addition to this, the strong dependence of the boundary normals with respect to their observed locations suggests that the draping pattern of magnetic field lines play a principal role in enhancing the plasma flow along the Y_{VSO} axis and subsequently sets up a velocity shear that favours the excitation and the growth of ionospheric boundary waves. Moreover, the flute instability may also arise as a parasitic mode to the growth of KHI wave where the curvature of the rippled ionopause concave toward the ionosphere [*Elphic and Ershkovich*, 1984]. Therefore, its role in the growth of the boundary wave should not be ruled out completely. However, it is also noteworthy to mention that the work in *Elphic and Ershkovich* [1984] concluded that the flute mode does not grow as rapidly compared to KHI and KHI remains the dominant instability on the ionopause.

6.6 Contribution

The discussions with regard to the role of magnetic field draping pattern in exciting and generating the ionospheric boundary wave to propagate mainly along the Y_{VSO} axis have been accepted for publication in Journal of Geophysical Research: Space Physics:

Chong, G. S., S. A. Pope, S. N. Walker, R. A. Frahm, T. L, Zhang, and Y. Futaana (2018), A statistical study of ionospheric boundary wave formation at Venus. *Journal of Geophysical Research - Space Physics.* doi:10.1029/2018JA025644.

Chapter 7

Conclusions

7.1 Summary

The objective of this thesis was to investigate the dynamics of the Venusian planetary space environment in relation to the incoming solar wind. The investigation centred on the stability of the ionopause and its role in the atmospheric evolution of Venus. In Chapter 2, a review of the solar wind interaction with magnetised (e.g. Earth) and unmagnetised (e.g. Venus) planets was presented. Following this, the dynamic response of the Venusian ionopause was highlighted and the role of the ionospheric boundary wave in the atmospheric plasma removal mechanism was discussed. In Chapter 3, the instrumentations onboard of VEX utilised in this thesis were introduced in detail and its suitability in investigating the boundary wave events was also elaborated. The MV analysis technique which was implemented to assess the discontinuity conditions and the normal directions of boundary crossings was described.

In Chapter 4, a detailed analysis of ionospheric boundary wave perturbation on 26 June 2006 was presented. An approach was implemented to identify these boundary wave crossings. The approach was based on the observations of photoelectron dropout events while VEX was in the ionosphere, of which the corresponding magnetic field magnitudes were similar to those in the magnetic barrier. MV analysis revealed that these intervals were ionopause crossings. Further analysis on these boundary crossings shows that the ionopause on this date was not smooth, but exhibited a wavelike appearance which VEX traversed across. A flux rope was also identified in the vicinity of the boundary wave. The consistency shown from their sizes and observed locations suggested that this flux rope was created as a result of the boundary wave reaching the turbulent stage. Results also indicated that this boundary wave was generated by KHI as it was observed in the terminator region where the tangential shear flow is strong.

Chapter 5 presented a statistical analysis of all the identified boundary wave events based on a similar approach in Chapter 4 to measure their overall distributions. Results showed that this wavelike appearance of the ionopause is not rare but can be observed in around 23% of all the available VEX orbits across the whole mission. Similar to the event presented in Chapter 4, results showed that the majority of the identified boundary waves are consistently observed to be a propagating along the dawn-dusk (Y_{VSO}) direction with amplitude growing along the Z_{VSO} direction.

In addition, ‘smooth’ ionospheric boundary cases were also identified. Their respective boundary normal directions at the locations of the crossings were shown to lie radially outward from the centre of Venus, indicating a smooth quasi-spherical boundary. Analysis on these crossings allowed the dynamics of the ionospheric current sheet to be investigated. Results showed that the ionopause has an average boundary thickness of 57 ± 4 km, a value which is higher than those estimated in *Elphic et al.* [1981] and *Elphic et al.* [1980]. Further analysis also showed that the boundary is thicker for weaker pressure and at higher altitudes. On the other hand, the boundary is thinner for stronger pressure at lower altitudes.

In addition to its signature “potato chip” shape hodogram, flux ropes were also identified based on the absence of a photoelectron population. These flux ropes were observed to be quasi-horizontal (to the surface of Venus) and have axial orientations which lie along the X_{VSO} direction. Their shapes also appeared to be irregular. The consistency in the sizes, locations and orientations shown between the identified flux ropes and boundary wave events suggest that these flux ropes are created as a result of the boundary wave reaching the turbulent stage.

In Chapter 6, three potential boundary wave generation mechanisms were discussed, i.e. the KHI, ionopause altitude fluctuation [*Brace et al.*, 1980] and reversed magnetic field orientations [*Luhmann*, 1990]. Analyses suggest all three mechanisms may play roles in boundary wave excitation, but only KHI could explain the excitation of a boundary wave that can subsequently propagate mainly along the dawn-dusk (Y_{VSO}) direction with amplitude growing along the Z_{VSO} direction. The estimated velocity shear across the ionopause and the boundary wavelength are similar to those from simulation studies on KHI, a result which indicated that the development of ionospheric boundary waves was due to the KHI. Furthermore, the strong dependence shown from the boundary normals on their respective observed locations suggests that the draping pattern of magnetic field lines play a principal role in enhancing the plasma flow along the Y_{VSO} axis. This could subsequently set up a velocity shear that may favour the excitation of ionospheric boundary waves.

7.2 Key findings and limitations

Chapter 4 presented a detailed analysis of evidence of ionospheric boundary waves at Venus by utilising data from VEX. An approach was implemented to identify potential boundary crossings resulting from ionospheric boundary waves. Coupled with MV analysis, this approach was able to demonstrate whether or not the boundary crossings are 'smooth'. By implementing this approach over the entire duration of VEX mission, Chapter 5 presented the first statistical evidence of the observational existence of the ionospheric boundary wave phenomena at Venus. The results indicated that this wavelike appearance of the boundary is a common characteristic of the ionopause. It can be observed everywhere in the rather constrained northern polar region of Venus where the ionosphere was mostly sampled due to the VEX high latitude polar orbit. For the same reason, it is unclear whether or not the ionopause in other regions (e.g. subsolar, equatorial, southern polar and nightside regions) could exhibit a wavelike appearance. However, it is noteworthy to mention that the observations of a boundary wave event can be rather subjective, in the sense that it cannot be demonstrated for certain whether the ionopause always exhibits a wavelike appearance, and if the observation is dependent exclusively on the chances of spacecraft crossing them.

The results in Chapter 5 reveal that the boundary wave characteristics are very similar to those reported in Chapter 4: an ionospheric boundary wave that propagates mainly along the Y_{VSO} direction with its amplitude growing along the Z_{VSO} direction in the northern polar region of Venus. Further analysis indicated that the boundary wave was likely to be excited by KHI. These are the first statistical results that report such unexpected behaviour of the KHI-induced boundary wave, and are inconsistent to the conventional understanding. For instance, the velocity shear profile that could give rise to KHI in the terminator region has always been expected to be attributed to the strong tangential solar wind bulk flow along the X_{VSO} direction, and not along the Y_{VSO} direction as revealed by the statistical analysis. Further analysis conducted in Chapter 6 indicated that the draping pattern of magnetic field lines could play a principal role in enhancing the plasma flow along the Y_{VSO} direction and subsequently sets up a velocity shear that favours the excitation of ionospheric boundary waves along this direction.

Chapter 6 also revealed that proposed boundary wave generation mechanisms, such as the ionopause altitude fluctuation [*Brace et al.*, 1980] and reversed magnetic field orientations [*Luhmann*, 1990] may play a potential, but non-fundamental role of in the occurrence of boundary wave events. However, the results do not rule out the possibility of the potential coupling between the role of field draping and the involvements of all three proposed mechanisms in inducing the boundary wave to propagate along the Y_{VSO} axis.

Chapter 5 also presented the first statistical observational study on the ionopause dynamics based on VEX data during the solar minimum period. This complements the investigation conducted by *Elphic et al.* [1981] in which data from the PVO mission over the solar maximum period was utilised. Results showed that the boundary thickness varies with the external pressure: the plasma collisional properties that cause the broadening/narrowing of a boundary is a function of the ionopause altitude dictated mainly by the external pressure. This characteristic dynamic is consistent to that described in *Elphic et al.* [1981]. However, the results showed that the estimated ionopause thickness in this work is roughly 1.5 times more than that estimated in *Elphic et al.* [1981]. This is because the analysis in both works were conducted over two different solar activities, i.e. quieter solar activity leads to weaker thermal pressure that results in lower ionopause altitude where plasma becomes more collisional. The ionopause thickness is an important quantitative value as the estimation of the wavelength of the KHI induced boundary wave depends inversely on the ionopause thickness (hence the solar activity). On a side note, one of the criteria for the selection of boundary crossings in this study is based on clear magnetic transformation from the magnetic barrier into an unmagnetised ionosphere. Hence, the results presented here might show bias towards the ionospheric conditions that are similar to solar maximum, where the ionosphere is often unmagnetised.

The second half of Chapter 5 presented the first study on the ionospheric flux ropes that were identified based on their origins, i.e. as a result of turbulent boundary wave. The outcomes of this statistical study were twofold. Firstly, a number of studies (e.g. *Wolff et al.* [1980], *Thomas and Winske* [1991], and *Lu et al.* [2015] etc.) have demonstrated that magnetic irregularities such as the atmospheric bubbles and flux ropes can be created as a result of turbulent boundary waves. Unlike past studies that focused on the production of such structures on an individual basis, the results presented in Chapter 5 provides observational evidence that the production of flux ropes can be linked directly to the turbulent boundary wave.

Secondly, past studies [*Elphic and Russell*, 1983; *Russell*, 1990; *Chen et al.*, 2017] on the Venusian ionospheric flux ropes revealed that their orientations are quasi-horizontal (to the Venus surface) at higher altitudes, a puzzling characteristic that has not been well investigated. This is addressed by this thesis. For instance, on the basis that they resulted from a turbulent boundary wave, analysis of these identified flux ropes in this thesis showed that they have orientations that are not only quasi-horizontal to the Venus surface, but are also quasi-parallel to the X_{VSO} direction. These preferable orientations of flux ropes are consistent to the past studies and this can be well explained by their production mechanism: a turbulent boundary wave that propagates mainly along the dawn-dusk (Y_{VSO}) direction would result in the production of flux ropes with orientations quasi-parallel to the X_{VSO} direction.

Atmospheric bubbles are also expected to form in a similar fashion to the production of flux ropes. However, the convection of the atmospheric plasma out of the ionosphere and subsequently downstream with the main solar wind bulk flow, can change its magnetisation state as well as its characteristic energy signature. In addition, the magnetic barrier region, where atmospheric bubbles populate before they are convected downstream, is highly dynamic. These complications may result in the atmospheric bubbles not being accurately identified in this thesis. On a different note though, on the assumption that their sizes are comparable to those of flux ropes ($\approx$90 km), a prolonged period of continuous plasma loss into space as a result of detached atmospheric bubbles, would have had a significant impact on the atmospheric evolution on Venus.

7.3 Future Work

Due to the high latitude polar orbital period of VEX, only the ionosphere in the northern polar region of Venus was sampled. Hence, future work should consider revisiting and reassessing the data from PVO which often sampled the ionosphere around the subsolar region. Coupled with possible future missions that may sample the equatorial and nightside ionosphere regions, a global distribution of the the boundary wave phenomena can be measured to better understand the dynamics of the ionopause. On the other hand, boundary waves events have always been expected to exist only around the terminator region where the shear flow is the strongest. But if they can also be generated in regions that are unlikely to be unstable to wave excitation (e.g. regions of smaller SZA), then the role they play in removing the atmospheric contents from Venus would have been very significant and should not be overlooked.

The observational study conducted in this thesis shows that the draping pattern of magnetic field lines may play a role in setting up a velocity shear that favours the excitation of ionospheric boundary waves by KHI. Future model simulations of the

KHI at the Venus ionopause should consider whether or not the the involvement of field draping can lead to this unexpected behaviour of boundary waves. Future global simulation works should consider the boundary wave propagation direction, that is along the Y_{VSO} axis, to reveal the potential shapes of the possible magnetic irregularities (such as the atmospheric bubbles and the flux ropes) as a result of its evolution into the turbulent state.

In this thesis, only flux ropes which are created as a result of turbulent boundary wave events are selected for investigation. It would be of interest to identify the flux ropes that are created only via the mass loading mechanism, so that a direct comparison between these two mechanisms can be conducted, to assess their significance on an individual mechanism basis.

In addition, due to their complex plasma and magnetic characteristics resulting from being convected downstream with the solar wind bulk flow, atmospheric bubbles were not identified in this work. Hence, it would be an interest for future work to develop a qualitative approach to identify these atmospheric bubbles, perhaps by utilising the different instruments onboard of VEX. Therefore, their contributions to the Venusian atmospheric evolution can be measured more systematically and the numerical values of the plasma loss due to detached atmospheric bubbles can be more accurately quantified.

Mars, the only other unmagnetised terrestrial planet, is also subjected to plasma loss as a result of detached atmospheric bubbles. However, due to its smaller mass, the thermal escape mechanism plays a more crucial role [*Lammer et al.*, 2006] as the escape velocity is much lower at Mars, i.e. only ≈ 5 km s^{-1} (refer to Chapter 2.4.3). However, it will be an interest for future study to investigate whether or not the characteristics of the Martian ionospheric boundary wave are also comparable to those observed on Venus, and subsequently reassess their significance. The high resolution data from Mars Atmosphere and Volatile Evolution Mission (MAVEN), one of the current Mars orbiters, would provide an ideal opportunity to conduct the boundary wave events on Mars.

References

Acuna, M. H., J. E. P. Connerney, P. Wasilewski, R. P. Lin, K. A. Anderson, C. W. Carlson, J. McFadden, D. W. Curtis, D. Mitchell, H. Reme, C. Mazelle, J. A. Sauvaud, C. D'Uston, A. Cros, J. L. Medale, S. J. Bauer, P. Cloutier, M. Mayhew, D. Winterhalter, and N. F. Ness (1998), Magnetic Field and Plasma Observations at Mars: Initial Results of, *Science*, *279*, 1676, doi:10.1126/science.279.5357.1676.

Amerstorfer, U. V., N. V. Erkaev, D. Langmayr, and H. K. Biernat (2007), On Kelvin-Helmholtz instability due to the solar wind interaction with unmagnetized planets, *Planetary and Space Science*, *55*(12), 1811–1816, doi:10.1016/j.pss.2007.01.015.

Amerstorfer, U. V., N. V. Erkaev, U. Taubenschuss, and H. K. Biernat (2010), Influence of a density increase on the evolution of the Kelvin-Helmholtz instability and vortices, *Physics of Plasmas*, *17*(7), 072901, doi:10.1063/1.3453705.

Angsmann, A., M. Fränz, E. Dubinin, J. Woch, S. Barabash, T. L. Zhang, and U. Motschmann (2011), Magnetic states of the ionosphere of Venus observed by Venus Express, *Planetary and Space Science*, *59*, 327–337, doi:10.1016/j.pss.2010.12.004.

Arshukova, I., N. Erkaev, H. Biernat, and D. Vogl (2004), Interchange instability of the venusian ionopause, *Advances in Space Research*, *33*(2), 182–186, doi:10.1016/j.asr.2003.04.015.

Barabash, S., J.-A. Sauvaud, H. Gunell, H. Andersson, A. Grigoriev, K. Brinkfeldt, M. Holmström, R. Lundin, M. Yamauchi, K. Asamura, et al. (2007), The analyser of space plasmas and energetic atoms (ASPERA-4) for the Venus Express mission, *Planetary and Space Science*, *55*(12), 1772–1792, doi:10.1016/j.pss.2007.01.014.

Barabash, S., A. Fedorov, J. J. Sauvaud, R. Lundin, C. T. Russell, Y. Futaana, T. L. Zhang, H. Andersson, K. Brinkfeldt, A. Grigoriev, M. Holmström, M. Yamauchi, K. Asamura, W. Baumjohann, H. Lammer, A. J. Coates, D. O. Kataria, D. R. Linder, C. C. Curtis, K. C. Hsieh, B. R. Sandel, M. Grande, H. Gunell, H. E. J. Koskinen, E. Kallio, P. Riihelä, T. Säles, W. Schmidt, J. Kozyra, N. Krupp, M. Fränz, J. Woch, J. Luhmann, S. McKenna-Lawlor, C. Mazelle, J.-J. Thocaven, S. Orsini, R. Cerulli-Irelli, M. Mura, M. Milillo, M. Maggi, E. Roelof, P. Brandt, K. Szego, J. D. Winningham, R. A. Frahm, J. Scherrer, J. R. Sharber, P. Wurz, and P. Bochsler (2007), The loss of ions from Venus through the plasma wake, *Nature*, *450*, 650–653, doi:10.1038/nature06434.

Baumjohann, W., R. A. Treumann, and R. A. Treumann (1996), *Basic Space Plasma Physics*, vol. 57, World Scientific.

Behannon, K. W., F. M. Neubauer, and H. Barnstorf (1981), Fine-scale characteristics of interplanetary sector boundaries, *Journal of Geophysical Research*, *86*, 3273–3287, doi:10.1029/JA086iA05p03273.

Biernat, H. K., N. V. Erkaev, U. V. Amerstorfer, T. Penz, and H. I. M. Lichtenegger (2007), Solar wind flow past Venus and its implications for the occurrence of the Kelvin-Helmholtz instability, *Planetary and Space Science*, *55*(12), 1793–1803, doi:10.1016/j.pss.2007.01.006.

Brace, L. H., and A. J. Kliore (1991), The structure of the Venus ionosphere, *Space Science Reviews*, *55*, 81–163, doi:10.1007/BF00177136.

Brace, L. H., R. F. Theis, W. R. Hoegy, J. H. Wolfe, J. D. Mihalov, C. T. Russell, R. C. Elphic, and A. F. Nagy (1980), The dynamic behavior of the Venus ionosphere in response to solar wind interactions, *J. Geophys. Res.*, *85*(A13), 7663–7678, doi:10.1029/JA085iA13p07663.

Brace, L. H., R. F. Theis, and W. R. Hoegy (1982), Plasma clouds above the ionopause of Venus and their implications, *Planetary and Space Science*, *30*(1), 29–37, doi:10.1016/0032-0633(82)90069-1.

Brace, L. H., R. F. Theis, H. G. Mayr, S. A. Curtis, and J. G. Luhmann (1982), Holes in the nightside ionosphere of Venus, *Journal of Geophysical Research: Space Physics*, *87*, 199–211, doi:10.1029/JA087iA01p00199.

Brace, L. H., R. C. Elphic, S. A. Curtis, and C. T. Russell (1983), Wave structure in the Venus ionosphere downstream of the terminator, *Geophysical Research Letters*, *10*, 1116–1119, doi:10.1029/GL010i011p01116.

Brace, L. H., W. T. Kasprzak, H. A. Taylor, R. F. Theis, C. T. Russell, A. Barnes, J. D. Mihalov, and D. M. Hunten (1987), The ionotail of Venus - Its configuration and evidence for ion escape, *Journal of Geophysical Research: Space Physics*, *92*, 15–26, doi:10.1029/JA092iA01p00015.

Brain, D. A., F. Bagenal, Y.-J. Ma, H. Nilsson, and G. Stenberg Wieser (2016), Atmospheric escape from unmagnetized bodies, *Journal of Geophysical Research (Planets)*, *121*, 2364–2385, doi:10.1002/2016JE005162.

Chaisson, E., and S. McMillan (1995), *Astronomy : a beginner's guide to the universe*.

Chamberlain, J. W. (1961), Interplanetary Gas. III. a Hydrodynamic Model of the Corona., *The Astrophysical Journal*, *133*, 675, doi:10.1086/147070.

Chandrasekhar, S. (1961), *Hydrodynamic and hydrodynamic stability*, Oxford University Press, Oxford.

Chen, Y. Q., T. L. Zhang, S. D. Xiao, and G. Q. Wang (2017), Characteristics of ionospheric flux rope at the terminator observed by Venus Express, *Journal of Geophysical Research (Space Physics)*, *122*, 8858–8867, doi:10.1002/2017JA023999.

Chong, G. S., S. A. Pope, T. L. Zhang, G. A. Collinson, S. N. Walker, and M. A. Balikhin (2017), A study of ionopause perturbation and associated boundary wave formation at Venus, *Journal of Geophysical Research (Space Physics)*, *122*, 4284–4298, doi:10.1002/2016JA023769.

Chong, G. S., S. A. Pope, S. N. Walker, R. A. Frahm, T. Zhang, and Y. Futaana (2018), A statistical study of ionospheric boundary wave formation at venus, *Journal of Geophysical Research: Space Physics*, doi:10.1029/2018JA025644.

Coates, A. J., R. A. Frahm, D. R. Linder, D. O. Kataria, Y. Soobiah, G. Collinson, J. R. Sharber, J. D. Winningham, S. J. Jeffers, S. Barabash, J.-A. Sauvaud, R. Lundin, M. Holmström, Y. Futaana, M. Yamauchi, A. Grigoriev, H. Andersson, H. Gunell, A. Fedorov, J.-J. Thocaven, T. L. Zhang, W. Baumjohann, E. Kallio, H. Koskinen, J. U. Kozyra, M. W. Liemohn, Y. Ma, A. Galli, P. Wurz, P. Bochsler, D. Brain, E. C. Roelof, P. Brandt, N. Krupp, J. Woch, M. Fraenz, E. Dubinin, S. McKenna-Lawlor, S. Orsini, R. Cerulli-Irelli, A. Mura, A. Milillo, M. Maggi, C. C. Curtis, B. R. Sandel, K. C. Hsieh, K. Szego, A. Asamura, and M. Grande (2008), Ionospheric photoelectrons at Venus: Initial observations by ASPERA-4 ELS, *Planetary and Space Science*, *56*, 802–806, doi:10.1016/j.pss.2007.12.008.

Collinson, G., L. Wilson, D. Sibeck, N. Shane, T. Zhang, T. Moore, A. J. Coates, and S. Barabash (2012), Short large-amplitude magnetic structures (SLAMS) at Venus, *Journal of Geophysical Research: Space Physics (1978–2012)*, *117*(A10), doi: 0.1029/2012JA017838.

Collinson, G. A., R. A. Frahm, A. Glocer, A. J. Coates, J. M. Grebowsky, S. Barabash, S. D. Domagal-Goldman, A. Fedorov, Y. Futaana, L. K. Gilbert, G. Khazanov, T. A. Nordheim, D. Mitchell, T. E. Moore, W. K. Peterson, J. D. Winningham, and T. L. Zhang (2016), The electric wind of Venus: A global and persistent "polar wind"-like ambipolar electric field sufficient for the direct escape of heavy ionospheric ions, *Geophysical Research Letters*, *43*, 5926–5934, doi:10.1002/2016GL068327.

Correia, A. C. M., and J. Laskar (2010), *Tidal Evolution of Exoplanets*, pp. 239–266.

Cui, J., M. Galand, A. J. Coates, T. L. Zhang, and I. C. F. Müller-Wodarg (2011), Suprathermal electron spectra in the Venus ionosphere, *Journal of Geophysical Research (Space Physics)*, *116*, A04321, doi:10.1029/2010JA016153.

de Pater, I., and J. J. Lissauer (2001), *Planetary Sciences*, Cambridge University Press.

Donahue, T. M., and R. E. Hartle (1992), Solar cycle variations in H(+) and D(+) densities in the Venus ionosphere - Implications for escape, *Geophysical research letters*, *19*, 2449–2452, doi:10.1029/92GL02927.

Dubinin, E., M. Fraenz, A. Fedorov, R. Lundin, N. Edberg, F. Duru, and O. Vaisberg (2012), *Ion Energization and Escape on Mars and Venus*, p. 173, Springer, doi: 10.1007/978-1-4614-3290-6_6.

Dubinin, E., M. Fraenz, T. L. Zhang, J. Woch, Y. Wei, A. Fedorov, S. Barabash, and R. Lundin (2013), Plasma in the near Venus tail: Venus Express observations, *Journal of Geophysical Research (Space Physics)*, *118*, 7624–7634, doi: 10.1002/2013JA019164.

Elphic, R. C., and A. I. Ershkovich (1984), On the stability of the ionopause of Venus, *J. Geophys. Res.*, *89*(A2), 997–1002, doi:10.1029/JA089iA02p00997.

Elphic, R. C., and C. T. Russell (1983), Global characteristics of magnetic flux ropes in the Venus ionosphere, *J. Geophys. Res.*, *88*(A4), 2993–3003, doi: 10.1029/JA088iA04p02993.

Elphic, R. C., and C. T. Russell (1983), Magnetic flux ropes in the Venus ionosphere - Observations and models, *Journal of Geophysical Research: Space Physics*, *88*, 58–72, doi:10.1029/JA088iA01p00058.

Elphic, R. C., C. T. Russell, J. A. Slavin, and L. H. Brace (1980), Observations of the dayside ionopause and ionosphere of Venus, *J. Geophys. Res.*, *85*(A13), 7679–7696, doi:10.1029/JA085iA13p07679.

Elphic, R. C., C. T. Russell, J. G. Luhmann, F. L. Scarf, and L. H. Brace (1981), The Venus ionopause current sheet — Thickness length scale and controlling factors, *Journal of Geophysical Research: Space Physics*, *86*, 11,430–11,438, doi: 10.1029/JA086iA13p11430.

Evans, J. D. (1996), *Straightforward statistics for the behavioral sciences*, Brooks/Cole.

Fränz, M., E. Dubinin, E. Roussos, J. Woch, J. D. Winningham, R. Frahm, A. J. Coates, A. Fedorov, S. Barabash, and R. Lundin (2007), *Plasma Moments in the Environment of Mars*, p. 165, doi:10.1007/978-0-387-70943-7_7.

Futaana, Y., S. Barabash, M. Yamauchi, S. McKenna-Lawlor, R. Lundin, J. G. Luhmann, D. Brain, E. Carlsson, J.-A. Sauvaud, J. D. Winningham, R. A. Frahm,

P. Wurz, M. Holmström, H. Gunell, E. Kallio, W. Baumjohann, H. Lammer, J. R. Sharber, K. C. Hsieh, H. Andersson, A. Grigoriev, K. Brinkfeldt, H. Nilsson, K. Asamura, T. L. Zhang, A. J. Coates, D. R. Linder, D. O. Kataria, C. C. Curtis, B. R. Sandel, A. Fedorov, C. Mazelle, J.-J. Thocaven, M. Grande, H. E. J. Koskinen, T. Sales, W. Schmidt, P. Riihela, J. Kozyra, N. Krupp, J. Woch, M. Fränz, E. Dubinin, S. Orsini, R. Cerulli-Irelli, A. Mura, A. Milillo, M. Maggi, E. Roelof, P. Brandt, K. Szego, J. Scherrer, and P. Bochsler (2008), Mars Express and Venus Express multi-point observations of geoeffective solar flare events in December 2006, *Planetary and Space Science*, *56*, 873–880, doi:10.1016/j.pss.2007.10.014.

Futaana, Y., G. Stenberg Wieser, S. Barabash, and J. G. Luhmann (2017), Solar wind interaction and impact on the Venus atmosphere, *Space Science Reviews*, *212*, 1453–1509, doi:10.1007/s11214-017-0362-8.

Goetz, C., C. Koenders, I. Richter, K. Altwegg, J. Burch, C. Carr, E. Cupido, A. Eriksson, C. Güttler, P. Henri, P. Mokashi, Z. Nemeth, H. Nilsson, M. Rubin, H. Sierks, B. Tsurutani, C. Vallat, M. Volwerk, and K.-H. Glassmeier (2016), First detection of a diamagnetic cavity at comet 67P/Churyumov-Gerasimenko, *Astronomy & Astrophysics*, *588*, A24, doi:10.1051/0004-6361/201527728.

Hamano, K., Y. Abe, and H. Genda (2013), Emergence of two types of terrestrial planet on solidification of magma ocean, *Nature*, *497*, 607–610, doi:10.1038/nature12163.

Hones, E. W., Jr. (1984), Magnetic reconnection in space and laboratory plasmas, *EOS Transactions*, *65*, 340–341, doi:10.1029/EO065i018p00340.

Horbury, T. S., D. Burgess, M. Fränz, and C. J. Owen (2001), Three spacecraft observations of solar wind discontinuities, *Geophysical research letters*, *28*, 677–680, doi:10.1029/2000GL000121.

Huba, J. D. (1981), The Kelvin-Helmholtz instability in inhomogeneous plasmas, *J. Geophys. Res.*, *86*(A5), 3653–3656, doi:10.1029/JA086iA05p03653.

Ingersoll, A. P. (1969), The Runaway Greenhouse: A History of Water on

Venus., *Journal of Atmospheric Sciences*, *26*, 1191–1198, doi:10.1175/1520-0469(1969)026¡1191:TRGAHO¿2.0.CO;2.

Johnson, N. L. (1979), Handbook of Soviet lunar and planetary exploration, *NASA STI/Recon Technical Report A*, *80.*

Kasting, J. F. (1988), Runaway and moist greenhouse atmospheres and the evolution of earth and Venus, *Icarus*, *74*, 472–494, doi:10.1016/0019-1035(88)90116-9.

Kasting, J. F., and J. B. Pollack (1983), Loss of water from Venus. I - Hydrodynamic escape of hydrogen, *Icarus*, *53*, 479–508, doi:10.1016/0019-1035(83)90212-9.

Kella, D., L. Vejby-Christensen, P. Johnson, H. B. Pedersen, and L. H. Andersen (1997), The source of green light emission determined from a heavy-ion storage ring experiment, *Science*, *276*(5318), 1530–1533.

Kennel, C., J. Edmiston, and T. Hada (1984), *A quarter century of collisionless shock research*, Wiley Online Library.

Khrabrov, A. V., and B. U. Ö. Sonnerup (1998), Error estimates for minimum variance analysis, *Journal of Geophysical Research: Space Physics*, *103*, 6641–6652, doi:10.1029/97JA03731.

Kivelson, M. G., and C. T. Russell (1995), *Introduction to Space Physics*, 586 pp.

Knetter, T., F. M. Neubauer, T. Horbury, and A. Balogh (2004), Four-point discontinuity observations using Cluster magnetic field data: A statistical survey, *Journal of Geophysical Research (Space Physics)*, *109*, A06102, doi:10.1029/2003JA010099.

Knudsen, W. C., K. Spenner, K. L. Miller, and V. Novak (1980), Transport of ionospheric O/+/ ions across the Venus terminator and implications, *Journal of Geophysical Research: Space Physics*, *85*, 7803–7810, doi:10.1029/JA085iA13p07803.

Knudsen, W. C., K. L. Miller, and K. Spenner (1982), Improved Venus ionopause altitude calculation and comparison with measurement, *Journal of Geophysical Research: Space Physics*, *87*, 2246–2254, doi:10.1029/JA087iA04p02246.

Lammer, H., H. I. M. Lichtenegger, H. K. Biernat, N. V. Erkaev, I. L. Arshukova, C. Kolb, H. Gunell, A. Lukyanov, M. Holmstrom, S. Barabash, T. L. Zhang, and W. Baumjohann (2006), Loss of hydrogen and oxygen from the upper atmosphere of Venus, *Planetary and Space Science*, *54*(13-14), 1445–1456, doi: 10.1016/j.pss.2006.04.022.

Lammer, H., J. F. Kasting, E. Chassefière, R. E. Johnson, Y. N. Kulikov, and F. Tian (2008), Atmospheric Escape and Evolution of Terrestrial Planets and Satellites, *Space Science Reviews*, *139*, 399–436, doi:10.1007/s11214-008-9413-5.

Leinweber, H. K., C. T. Russell, K. Torkar, T. L. Zhang, and V. Angelopoulos (2008), An advanced approach to finding magnetometer zero levels in the interplanetary magnetic field, *Measurement Science and Technology*, *19*(5), 055104, doi:10.1088/0957-0233/19/5/055104.

Lepping, R., and K. Behannon (1980), Magnetic field directional discontinuities: 1. minimum variance errors, *Journal of Geophysical Research: Space Physics*, *85*(A9), 4695–4703, doi:10.1029/JA085iA09p04695.

Lu, H. Y., J. B. Cao, T. L. Zhang, H. S. Fu, and Y. S. Ge (2015), Evolution of Kelvin-Helmholtz instability at Venus in the presence of the parallel magnetic field, *Physics of Plasmas*, *22*(6), 062902, doi:10.1063/1.4922753.

Luger, R., and R. Barnes (2015), Extreme Water Loss and Abiotic O2Buildup on Planets Throughout the Habitable Zones of M Dwarfs, *Astrobiology*, *15*, 119–143, doi:10.1089/ast.2014.1231.

Luhmann, J. G. (1986), The solar wind interaction with Venus, *Space Science Reviews*, *44*, 241–306, doi:10.1007/BF00200818.

Luhmann, J. G. (1990), 'Wave' analysis of Venus ionospheric flux ropes, *Washington DC American Geophysical Union Geophysical Monograph Series*, *58*, 425–432, doi: 10.1029/GM058p0425.

Luhmann, J. G., and T. E. Cravens (1991), Magnetic fields in the ionosphere of Venus, *Space Science Reviews*, *55*, 201–274, doi:10.1007/BF00177138.

Luhmann, J. G., and J. U. Kozyra (1991), Dayside pickup oxygen ion precipitation at Venus and Mars — Spatial distributions, energy deposition and consequences, *Journal of Geophysical Research: Space Physics*, *96*, 5457–5467, doi:10.1029/90JA01753.

Luhmann, J. G., and C. T. Russell (1997), Venus: Magnetic field and magnetosphere, in *Encyclopedia of planetary science*, Encyclopedia of Earth Science, pp. 905–907, Springer Netherlands.

Luhmann, J. G., R. C. Elphic, C. T. Russell, J. D. Mihalov, and J. H. Wolfe (1980), Observations of large scale steady magnetic fields in the dayside Venus ionosphere, *Geophysical Research Letters*, *7*, 917–920, doi:10.1029/GL007i011p00917.

Luhmann, J. G., C. T. Russell, and R. C. Elphic (1984), Time scales for the decay of induced large-scale magnetic fields in the Venus ionosphere, *Journal of Geophysical Research: Space Physics*, *89*, 362–368, doi:10.1029/JA089iA01p00362.

Marshall, M. (2009), Timeline: The evolution of life.

Marubashi, K., J. M. Grebowsky, H. A. Taylor, J. G. Luhmann, C. T. Russell, and A. Barnes (1985), Magnetic field in the wake of Venus and the formation of ionospheric holes, *Journal of Geophysical Research: Space Physics*, *90*, 1385–1398, doi: 10.1029/JA090iA02p01385.

Masters, A., N. Achilleos, C. Bertucci, M. K. Dougherty, S. J. Kanani, C. S. Arridge, H. J. McAndrews, and A. J. Coates (2009), Surface waves on Saturn's dawn flank magnetopause driven by the Kelvin-Helmholtz instability, *Planetary and Space Science*, *57*, 1769–1778, doi:10.1016/j.pss.2009.02.010.

Masunaga, K., Y. Futaana, M. Yamauchi, S. Barabash, T. L. Zhang, A. O. Fedorov, N. Terada, and S. Okano (2011), O^+ outflow channels around Venus controlled by directions of the interplanetary magnetic field: Observations of high energy O^+ ions around the terminator, *Journal of Geophysical Research (Space Physics)*, *116*, A09326, doi:10.1029/2011JA016705.

McComas, D. J., H. E. Spence, C. T. Russell, and M. A. Saunders (1986), The average magnetic field draping and consistent plasma properties of the Venus magnetotail, *Journal of Geophysical Research: Space Physics*, *91*, 7939–7953, doi: 10.1029/JA091iA07p07939.

McElroy, M. B., M. J. Prather, and J. M. Rodriguez (1982), Escape of hydrogen from Venus, *Science*, *215*, 1614, doi:10.1126/science.215.4540.1614.

Morrison, D., and T. Owen (1996), *The planetary system.*, Addison-Wesley Publishing.

Möstl, U. V., N. V. Erkaev, M. Zellinger, H. Lammer, H. Gröller, H. K. Biernat, and D. Korovinskiy (2011), The Kelvin-Helmholtz instability at Venus: What is the unstable boundary?, *Icarus*, *216*, 476–484, doi:10.1016/j.icarus.2011.09.012.

Nagano, H. (1978), Effect of finite ion Larmor radius on the Kelvin-Helmholtz instability, *Journal of Plasma Physics*, *20*, 149–160, doi:10.1017/S0022377800021450.

Nagano, H. (1979), Effect of finite ion Larmor radius on the Kelvin-Helmholtz instability of the magnetopause, *Planetary and Space Science*, *27*, 881–884, doi: 10.1016/0032-0633(79)90013-8.

Neugebauer, M., D. Clay, B. Goldstein, B. Tsurutani, and R. Zwickl (1984), A reexamination of rotational and tangential discontinuities in the solar wind, *Journal of Geophysical Research: Space Physics*, *89*(A7), 5395–5408.

Nykyri, K., and A. Otto (2001), Plasma transport at the magnetospheric boundary due to reconnection in Kelvin-Helmholtz vortices, *Geophysical research letters*, *28*, 3565–3568, doi:10.1029/2001GL013239.

Ong, R. S. B., and N. Roderick (1972), On the kelvin-Helmholtz instability of the Earth's magnetopause, *Planetary and Space Science*, *20*(1), 1–10, doi:10.1016/0032-0633(72)90135-3.

Öpik, E. J., and S. F. Singer (1961), Distribution of Density in a Planetary Exosphere. II, *Physics of Fluids*, *4*, 221–233, doi:10.1063/1.1724432.

Owens, M. J., and R. J. Forsyth (2013), The Heliospheric Magnetic Field, *Living Reviews in Solar Physics*, *10*, 5, doi:10.12942/lrsp-2013-5.

Penz, T., N. Erkaev, H. Biernat, H. Lammer, U. Amerstorfer, H. Gunell, E. Kallio, S. Barabash, S. Orsini, A. Milillo, et al. (2004), Ion loss on mars caused by the Kelvin-Helmholtz instability, *Planetary and Space Science*, *52*(13), 1157–1167, doi: 10.1016/j.pss.2004.06.001.

Pérez-de Tejada, H., M. Dryer, and O. L. Vaisberg (1977), Viscous flow in the near-Venusian plasma wake, *J. Geophys. Res.*, *82*(19), 2837–2841, doi: 10.1029/JA082i019p02837.

Phillips, J. L., J. G. Luhmann, and C. T. Russell (1986), Magnetic configuration of the Venus magnetosheath, *Journal of Geophysical Research: Space Physics*, *91*, 7931–7938, doi:10.1029/JA091iA07p07931.

Pollack, J. B., J. F. Kasting, S. M. Richardson, and K. Poliakoff (1987), The case for a wet, warm climate on early Mars, *Icarus*, *71*, 203–224, doi:10.1016/0019-1035(87)90147-3.

Pope, S. A., M. A. Balikhin, T. L. Zhang, A. O. Fedorov, M. Gedalin, and S. Barabash (2009), Giant vortices lead to ion escape from Venus and re-distribution of plasma in the ionosphere, *Geophys. Res. Lett.*, *36*(7), L07,202, doi:10.1029/2008GL036977.

Pope, S. A., T. L. Zhang, M. A. Balikhin, M. Delva, L. Hvizdos, K. Kudela, and A. P. Dimmock (2011), Exploring planetary magnetic environments using magnetically unclean spacecraft: A systems approach to VEX MAG data analysis, *Ann. Geophys.*, *29*(4), 639–647, doi:10.5194/angeo-29-639-2011.

Raymond, S. N., T. Quinn, and J. I. Lunine (2006), High-resolution simulations of the final assembly of Earth-like planets I. Terrestrial accretion and dynamics, *Icarus*, *183*, 265–282, doi:10.1016/j.icarus.2006.03.011.

Russell, C. T. (1990), Magnetic flux ropes in the ionosphere of Venus, *Washington DC American Geophysical Union Geophysical Monograph Series*, *58*, 413–423, doi: 10.1029/GM058p0413.

Russell, C. T., and R. C. Elphic (1979), Observation of magnetic flux ropes in the Venus ionosphere, *Nature*, *279*(5714), 616–618, doi:10.1038/279616a0.

Russell, C. T., R. C. Elphic, and J. A. Slavin (1979), Initial Pioneer Venus magnetic field results - Dayside observations, *Science*, *203*, 745–748, doi: 10.1126/science.203.4382.745.

Russell, C. T., R. C. Elphic, and J. A. Slavin (1980), Limits on the possible intrinsic magnetic field of Venus, *J. Geophys. Res.*, *85*(A13), 8319–8332, doi: 10.1029/JA085iA13p08319.

Russell, C. T., J. G. Luhmann, R. C. Elphic, F. L. Scarf, and L. H. Brace (1982), Magnetic field and plasma wave observations in a plasma cloud at Venus, *Geophys. Res. Lett.*, *9*(1), 45–48, doi:10.1029/GL009i001p00045.

Schwartz, S. J. (1998), Shock and discontinuity normals, mach numbers, and related parameters, *ISSI scientific reports series*, *1*, 249–270.

Sibeck, D. G., R. E. Lopez, and E. C. Roelof (1991), Solar wind control of the magnetopause shape, location, and motion, *Journal of Geophysical Research: Space Physics*, *96*, 5489–5495, doi:10.1029/90JA02464.

Siscoe, G. L. (1983), Solar system magnetohydrodynamics, in *Solar-terrestrial physics*, pp. 11–100, Springer.

Smith, E. J. (1973), Identification of interplanetary tangential and rotational discontinuities, *Journal of Geophysical Research*, *78*, 2054, doi:10.1029/JA078i013p02054.

Söding, A., F. M. Neubauer, B. T. Tsurutani, N. F. Ness, and R. P. Lepping (2001), Radial and latitudinal dependencies of discontinuities in the solar wind between 0.3 and 19 AU and -80° and +10°, *Annales Geophysicae*, *19*, 681–686.

Sonett, C. P. (1963), A Summary Review of the Scientific Findings of the Mariner Venus Mission, *Space Science Reviews*, *2*, 751–777, doi:10.1007/BF00208814.

Sonnerup, B. U. Ö., and L. J. Cahill (1967), Magnetopause structure and attitude from Explorer 12 observations, *J. Geophys. Res.*, *72*(1), 171–183, doi: 10.1029/JZ072i001p00171.

Sonnerup, B. U. O., and L. J. Cahill, Jr. (1967), Magnetopause Structure and Attitude from Explorer 12 Observations, *Journal of Geophysical Research*, *72*, 171, doi:10.1029/JZ072i001p00171.

Sonnerup, B. U. Ö., and L. J. Cahill, Jr. (1968), Explorer 12 observations of the magnetopause current layer, *Journal of Geophysical Research*, *73*, 1757, doi:10.1029/JA073i005p01757.

Sonnerup, B. U. Ö., and M. Scheible (1998), Minimum and maximum variance analysis, *ISSI Scientific Reports Series*, *1*, 185–220.

Spreiter, J. R., A. L. Summers, and A. W. Rizzi (1970), Solar wind flow past nonmagnetic planets—Venus and Mars, *Planetary and Space Science*, *18*(9), 1281–1299, doi:10.1016/0032-0633(70)90139-X.

Stevenson, D. J. (2003), Planetary magnetic fields, *Earth and Planetary Science Letters*, *208*(1-2), 1–11, doi:10.1016/S0012-821X(02)01126-3.

Stevenson, D. J., T. Spohn, and G. Schubert (1983), Magnetism and thermal evolution of the terrestrial planets, *Icarus*, *54*(3), 466–489, doi:10.1016/0019-1035(83)90241-5.

Sundberg, T., S. A. Boardsen, J. A. Slavin, L. G. Blomberg, and H. Korth (2010), The Kelvin-Helmholtz instability at Mercury: An assessment, *Planetary and Space Science*, *58*, 1434–1441, doi:10.1016/j.pss.2010.06.008.

Svedhem, H., D. V. Titov, D. McCoy, J. P. Lebreton, S. Barabash, J. L. Bertaux, P. Drossart, V. Formisano, B. Häusler, O. Korablev, W. J. Markiewicz, D. Nevejans, M. Pätzold, G. Piccioni, T. L. Zhang, F. W. Taylor, E. Lellouch, D. Koschny, O. Witasse, H. Eggel, M. Warhaut, A. Accomazzo, J. Rodriguez-Canabal, J. Fabrega, T. Schirmann, A. Clochet, and M. Coradini (2007), Venus Express—The first European mission to Venus, *Planetary and Space Science*, *55*(12), 1636–1652, doi:10.1016/j.pss.2007.01.013.

Svedhem, H., D. Titov, F. Taylor, and O. Witasse (2009), Venus Express mission, *J. Geophys. Res.*, *114*(E5), E00B33, doi:10.1029/2008JE003290.

Tanaka, T. (1993), Configurations of the solar wind flow and magnetic field around the planets with no magnetic field: Calculation by a new MHD simulation scheme, *Journal of Geophysical Research: Space Physics*, *98*, 17,251–17,262, doi: 10.1029/93JA01516.

Taylor, F. W. (2006), Venus before Venus Express, *Planetary and Space Science*, *54*, 1249–1262, doi:10.1016/j.pss.2006.04.031.

Terada, N., S. Machida, and H. Shinagawa (2002), Global hybrid simulation of the Kelvin-Helmholtz instability at the Venus ionopause, *J. Geophys. Res.*, *107*(A12), 1471, doi:10.1029/2001JA009224.

Thomas, V. A., and D. Winske (1991), Kinetic simulation of the Kelvin-Helmholtz instability at the Venus ionopause, *Geophysical research letters*, *18*, 1943–1946, doi: 10.1029/91GL02552.

Titov, D. V., H. Svedhem, D. Koschny, R. Hoofs, S. Barabash, J. L. Bertaux, P. Drossart, V. Formisano, B. Häusler, O. Korablev, W. J. Markiewicz, D. Nevejans, M. Pätzold, G. Piccioni, T. L. Zhang, D. Merritt, O. Witasse, J. Zender, A. Accomazzo, M. Sweeney, D. Trillard, M. Janvier, and A. Clochet (2006), Venus Express science planning, *Planetary and Space Science*, *54*(13-14), 1279–1297, doi: 10.1016/j.pss.2006.04.017.

Vogt, M. F., P. Withers, P. R. Mahaffy, M. Benna, M. K. Elrod, J. S. Halekas, J. E. P. Connerney, J. R. Espley, D. L. Mitchell, C. Mazelle, and B. M. Jakosky (2015), Ionopause-like density gradients in the Martian ionosphere: A first look with MAVEN, *Geophysical Research Letters*, *42*, 8885–8893, doi:10.1002/2015GL065269.

Walker, S. N., M. A. Balikhin, T. L. Zhang, M. E. Gedalin, S. A. Pope, A. P. Dimmock, and A. O. Fedorov (2011), Unusual nonlinear waves in the Venusian magnetosheath, *J. Geophys. Res.*, *116*(A1), A01,215, doi:10.1029/2010JA015916.

Way, M. J., A. D. Del Genio, N. Y. Kiang, L. E. Sohl, D. H. Grinspoon, I. Aleinov, M. Kelley, and T. Clune (2016), Was Venus the First Habitable World of our Solar System?, *Geophysical Research Letters*, doi:10.1002/2016GL069790.

Wei, H., C. Russell, T. Zhang, and M. Dougherty (2010), Comparison study of magnetic flux ropes in the ionospheres of Venus, Mars and Titan, *Icarus*, *206*(1), 174–181, doi: 10.1016/j.icarus.2009.03.014.

Williams, D. R. (2005), Venus fact sheet, *Tech. rep.*, Tech. rep., NASA, 2005. http://nssdc.gsfc.nasa.gov/planetary/factsheet/index.html.

Wolff, R., B. Goldstein, and S. Kumar (1979), A model of the variability of the Venus ionopause altitude, *Geophysical Research Letters*, *6*(5), 353–356, doi: 10.1029/GL006i005p00353.

Wolff, R. S., B. E. Goldstein, and C. M. Yeates (1980), The onset and development of Kelvin-Helmholtz instability at the Venus ionopause, *J. Geophys. Res.*, *85*(A13), 7697–7707, doi:10.1029/JA085iA13p07697.

Zellinger, M., U. V. Möstl, N. V. Erkaev, and H. K. Biernat (2012), 2.5D magnetohydrodynamic simulation of the Kelvin-Helmholtz instability around Venus–Comparison of the influence of gravity and density increase, *Physics of Plasmas*, *19*(2), 022,104–022,104, doi:10.1063/1.3682039.

Zhang, T. L., W. Baumjohann, M. Delva, H.-U. Auster, A. Balogh, C. T. Russell, S. Barabash, M. Balikhin, G. Berghofer, H. K. Biernat, H. Lammer, H. Lichtenegger, W. Magnes, R. Nakamura, T. Penz, K. Schwingenschuh, Z. Vörös, W. Zambelli, K.-H. Fornacon, K.-H. Glassmeier, I. Richter, C. Carr, K. Kudela, J. K. Shi, H. Zhao, U. Motschmann, and J.-P. Lebreton (2006), Magnetic field investigation of the Venus plasma environment: Expected new results from Venus Express, *Planetary and Space Science*, *54*, 1336–1343, doi:10.1016/j.pss.2006.04.018.

Zhang, T. L., M. Delva, W. Baumjohann, H.-U. Auster, C. Carr, C. T. Russell, S. Barabash, M. Balikhin, K. Kudela, G. Berghofer, H. K. Biernat, H. Lammer, H. Lichtenegger, W. Magnes, R. Nakamura, K. Schwingenschuh, M. Volwerk, Z. Vörös, W. Zambelli, K.-H. Fornacon, K.-H. Glassmeier, I. Richter, A. Balogh, H. Schwarzl, S. A. Pope, J. K. Shi, C. Wang, U. Motschmann, and J.-P. Lebreton (2007), Little or no solar wind enters Venus' atmosphere at solar minimum, *Nature*, *450*(7170), 654–656, doi:10.1038/nature06026.

Zhang, T. L., M. Delva, W. Baumjohann, M. Volwerk, C. T. Russell, S. Barabash, M. Balikhin, S. Pope, K. H. Glassmeier, C. Wang, and K. Kudela (2008a), Initial Venus Express magnetic field observations of the magnetic barrier at solar minimum, *Planetary and Space Science*, *56*(6), 790–795, doi:10.1016/j.pss.2007.10.013.

Zhang, T. L., M. Delva, W. Baumjohann, M. Volwerk, C. T. Russell, S. Barabash, M. Balikhin, S. Pope, K. H. Glassmeier, K. Kudela, C. Wang, Z. Vörös, and W. Zambelli (2008b), Initial Venus Express magnetic field observations of the Venus bow shock location at solar minimum, *Planetary and Space Science*, *56*(6), 785–789, doi: 10.1016/j.pss.2007.09.012.

Zhang, T. L., J. Du, Y. J. Ma, H. Lammer, W. Baumjohann, C. Wang, and C. T. Russell (2009), Disappearing induced magnetosphere at Venus: Implications for close-in exoplanets, *Geophysical Research Letters*, *36*, L20203, doi:10.1029/2009GL040515.

Zwan, B. J., and R. A. Wolf (1976), Depletion of solar wind plasma near a planetary boundary, *Journal of Geophysical Research*, *81*, 1636–1648, doi: 10.1029/JA081i010p01636.

Appendix A

Hodograms of the magnetic field fluctuations on 26 June 2006

The results in this appendix complement the results in Chapter 4.

Figure A.1, A.2, A.3, A.4 and A.5 show the hodograms of the field variation in (a) B_{max} to B_{int} and (b) B_{max} to B_{min} plane over the duration stated in the figure captions respectively.

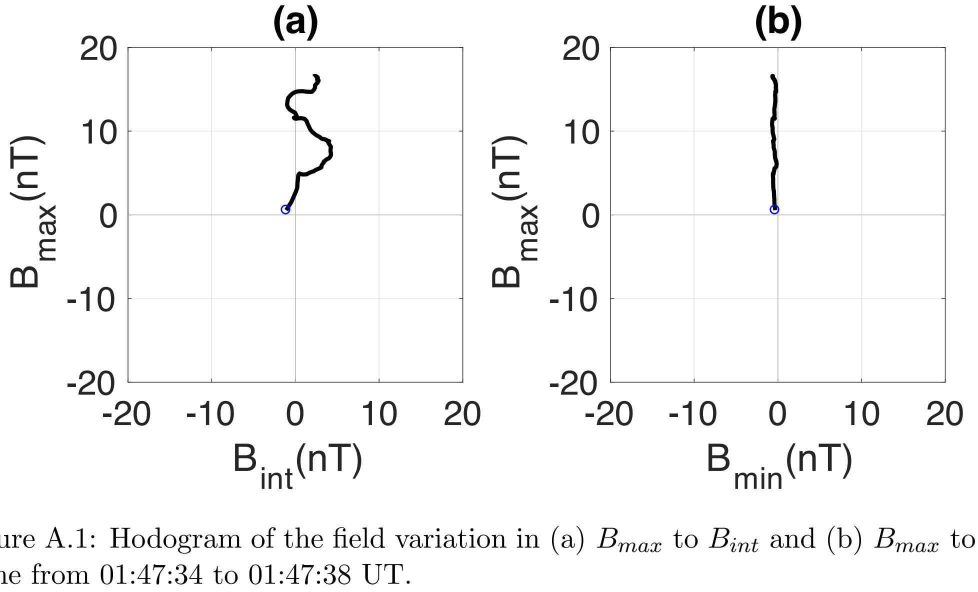

Figure A.1: Hodogram of the field variation in (a) B_{max} to B_{int} and (b) B_{max} to B_{min} plane from 01:47:34 to 01:47:38 UT.

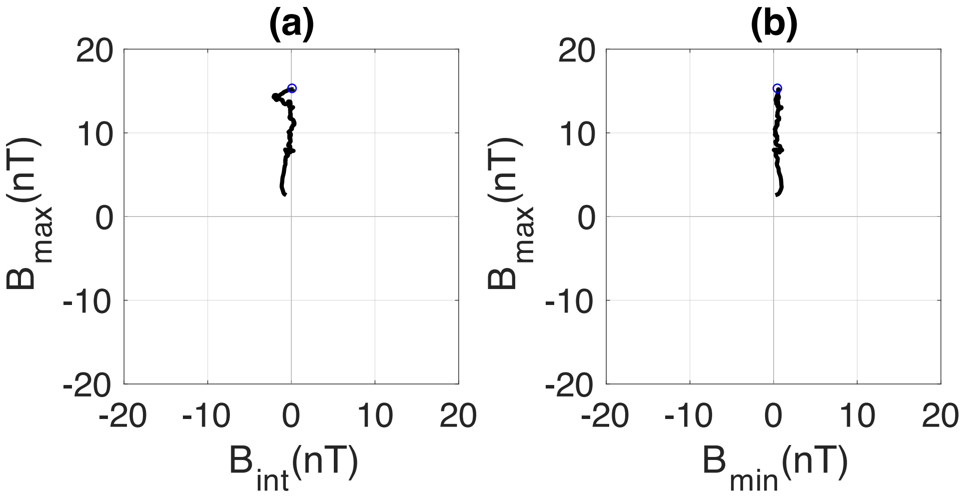

Figure A.2: Caption is same as Figure A.1 but from 01:47:40 to 01:47:48 UT.

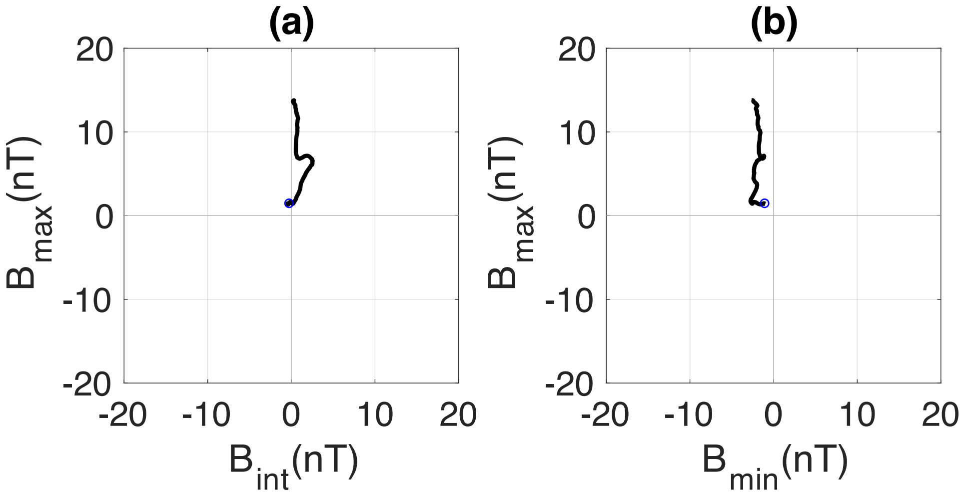

Figure A.3: Caption is same as Figure A.1 but from 01:47:51 to 01:47:55 UT.

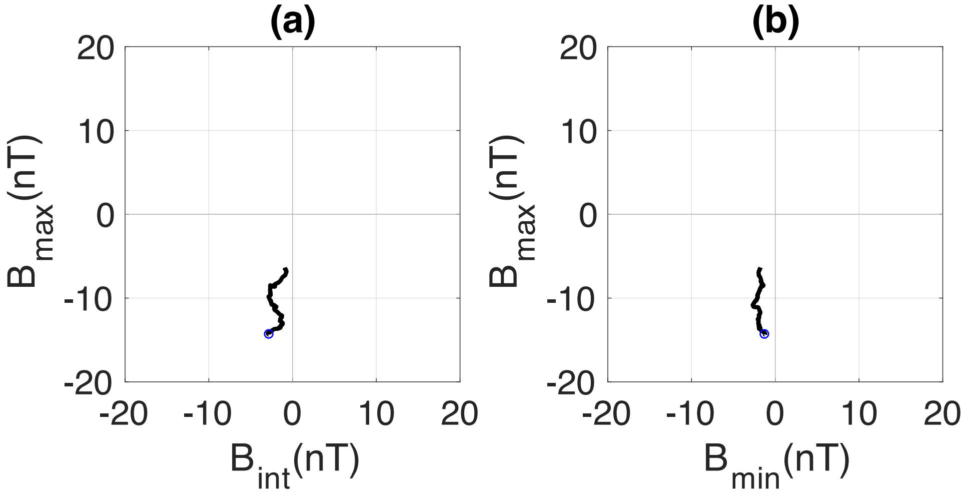

Figure A.4: Caption is same as Figure A.1 but from 01:47:59 to 01:48:06 UT.

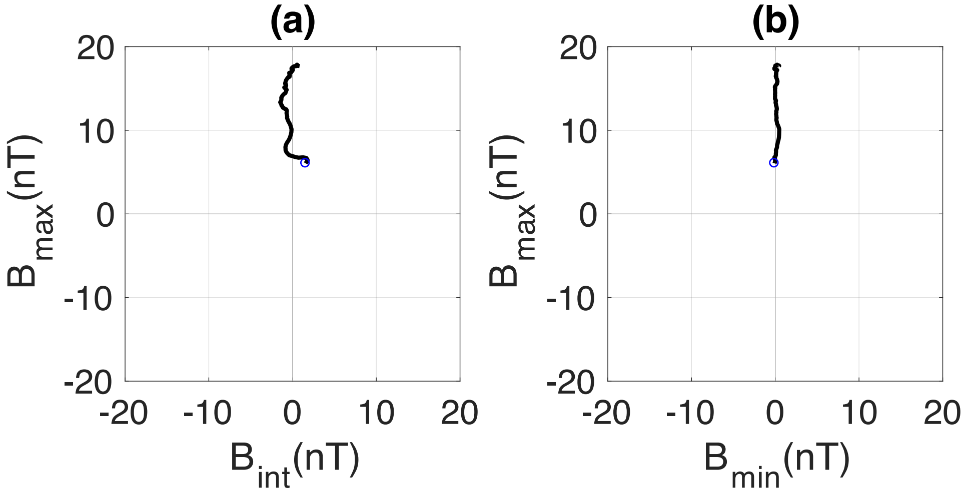

Figure A.5: Caption is same as Figure A.1 but from 01:48:08 to 01:48:11 UT.